Non-invasive functional gene delivery to the central and peripheral nervous system across species

Thesis by

Xinhong Chen

In Partial Fulfillment of the Requirements for
the Degree of
Doctor of Philosophy

CALIFORNIA INSTITUTE OF TECHNOLOGY
Pasadena, California

2023
(Defended March 7, 2023)

Xinhong Chen
ORCID: 0000-0003-0408-0813

TO

My dear Family and Friends

ACKNOWLEDGEMENTS

Pursuing a PhD has been a challenging journey. I could not have done this without the support of many mentors, colleagues, friends, and family. I would like to especially express my gratitude to these individuals.

I would like to start by thanking my advisor, Viviana Gradinaru. She provided us an incredible amount of intellectual freedom to explore all the possibilities in science with generous resources. Her inspiring scientific vision and ideas always guided me to think outside the box. Her philosophy of collaborative scientific environment enabled me to collaborate broadly with amazing scientists both in and outside of the lab. I feel extremely fortunate to work with her, not only because of the exciting science, but also because of her attitude towards career and life. She not only cares about the science we are doing, but even more cares about us as individual. She cheers on the ups in our lives while providing support when the downs are coming. I cannot think of a better mentor for both science and life.

I also got to learn from amazing mentors in the Gradinaru Lab. I would like to first thank Sripriya Ravindra Kumar. Priya, literally being my mentor since the first day I stepped in a Caltech lab, has taught me most of the things I know about AAV engineering. Her patience and cheerful nature have helped me get through all the failed experiments in the early days. All the fun conversation with her in the clover office really helped me going through the difficult times. Not just a mentor, Priya is also a great friend and I will not forget all those great boba and food we had together. I am also super excited to now she has a wonderful start for her professional career. I also want to thank Ryan Cho, who is my mentor for neuroscience. His dedication to neuroscience is a strong motivation for me to keep my passion for the exploration of the brain. The malibu chicken sandwich that we got to have together from Ernie’s truck always came with fun scientific discussions. There is no doubt that the future Cho Lab will produce amazing science.

There are amazing colleagues in the Gradinaru lab that contributed a lot to my science. I want to thank Damien Wolfe, who is an important part of many of the work I was involved in. Working and growing with him has been a great experience. I am also super proud of him now taking on the responsibility to help other underrepresented students gain access to research. I want to thank Yaping Lei and Erin Sullivan for experimental support. I want to thank Pat Anguiano, Elisha Mackey and Zhe Qu. My work would be impossible without their wonderful lab managing skills. I want to thank Catherine Oikonomou for her help with manuscript preparation.

I also got to work with and have fun together with lots of the wonderful Glab members. I also want to thank all the past and present amazing lab members Xiaozhe Ding, Tim Shay, Miguel Chuapoco, Acacia Mayfield, Changfan Lin, Mátè Borsos, Mengying Zhang, Min Jee Jang, Seongmin Jang, Cynthia Arokiaraj, Yujie Fan, Tatyana Dobreva, David Brown, David Goertsen, Gerry Coughlin, Anat Khan, Elliot Robinson, Michael Altermatt, Jennifer Treweek, Collin Challis, Rosemary Challis, Nick Flyzanis, Nick Goeden, Alexander Wang, Umesh Padia, Jimin Park, Alex Jin Chung, Cameron Jackson, Sayan Dutta, Jonathan Hoang, Josette Medicielo, Karan Mahe, Nathan Appling, and Tyler Brittian.

Outside of the Gradinaru Lab, I would like to thank Sarkis Mazmanian, Yuki Oka, and Carlos Lois for taking time to serve on my committee. Their research guidance and feedback during the committee meetings greatly facilitated my academic growth. I would also like to thank Henry Lester, who allowed me to TA his Neuropharmocology course.

I also was fortunate to have collaborators outside of the lab for my thesis work. I would like to thank Daping Yang and Isaac Chiu at Harvard Medical School, Dhanesh Sivadasan Bindu and Cagla Eroglu at Duke, Ana Badimon and Anne Schaefer at Mount Sinai, Lillian Campos and Andrew Fox at UC Davis, Victoria Ngo and Cory Miller at UCSD, Cameron Adams and Janet Keast at University of Melbourne, Tongtong Wang, Jessica Griffiths and Takako Ichiki at Caltech, Annika Keller and Sheng-Fu Huang at University of Zürich, Jonathan Ting, Boaz Levi, Naz Taskin, John Mich, Deja Monet, Victoria Ngo, Victoria Omstead, Natalie Weed, Yeme Bishaw, Bryan Gore, and Ed Lein at Allen Brain Institute,

Athena Akrami and Viktor Plattner at UCL. I would like to thank all the OLAR staffs at Caltech for their help over the year.

I am also super fortunate to have made lots of friends at Caltech including Zhiyang Jin, Kun Miao, Shumao Zhang, Yuxing Yao, Peiwei Chen, Yuelin Shi, Jiajun Du, Di Wu, Zhihao Cui, Tian Zeng, Ziyang Qin, Fangzhou Xiao, Yicheng Luo, Ronghui Zhu, Yapeng Su, Peng He, Ke Ding, Aditya Nair, Sangjun Lee, Xun Wang, Can Li, Yitong Ma, Sheng Wang, Ruohan Wang, Runze Mao, Yalu Chen, Xinyan Liu, Xinying Ren, Weilai Yu, Quan Gan, Shuoyan Xiong, Allen Shang, William Kuo, Yuwei Wu, Liuchi Li, Mengyu Liu, Zikun Zhu, Chenxi Qian, Kai Chen, Jingling Huang, Haolu Zhang, and many, many more. The PhD journey would have been much more challenging without all your support.

I want to thank my girlfriend, Yajuan Shi. I feel extremely lucky to have met her and have fallen in love with her during my PhD. We actually met during one of the academic conference where we presented our work. Words cannot describe how amazing it is to have her by my side when I finish the PhD journey and move on to my next step. I am looking forward to the upcoming exciting life chapters together with her.

Most importantly, I would like to dedicate this thesis to my parents, Muhui Zhu and Shaojie Chen. They provided me with the best environment in which to grow up that I could imagine and helped nurture my passion for science. During the many years that I could not come home due to visa issues, phone calls with them have constantly been the source for my inner peace. Without their unconditional love and support throughout the year, I wouldn’t be who I am today.

ABSTRACT

The normal function of the central nervous system (CNS) and peripheral nervous system (PNS) relies on precise regulation. When this regulation breaks down in diseases, genetic access to the nervous system is critical for therapeutic intervention. However, access to the nervous system remains difficult, reflecting the critical need for development of effective and non-invasive gene delivery vectors across species. By applying directed evolution approach, we identified 2 capsids, AAV-MaCPNS1 and AAV-MaCPNS2, which efficiently transduced the PNS in rodents following intravenous administration. Combining with rational optimization, we also identified AAV-X1 capsid family, which transduce brain endothelial cells specifically and efficiently following systemic administration in wild-type mice with diverse genetic backgrounds and rats. Some previously-engineered AAVs that target the nervous system fail to translate across non-human primate (NHP). We thus also further tested our novel vectors across species and showed that AAV-MaCPNS1/2 efficiently transduced both the PNS and CNS in NHPs. AAV-X1.1 also exhibit superior transduction of the CNS in rhesus macaques and *ex vivo* human brain slices although the endothelial tropism is not conserved across species.

With these enhanced systemic AAVs, we wanted to explore whether they could enable neuronal recording and modulation which has been challenging with the nature AAV serotypes. We used AAV-MaCPNS1 to systemically deliver the neuronal sensor jGCaMP8s to record calcium signal dynamics in nodose ganglia. We observed specific nodose neuronal response to physiological modulation in the gut. Furthermore, we showed that the MaCPNS1-delivered neuronal actuator DREADD to dorsal root ganglia could enable non-invasive neuronal modulation and create a model of pain. The functional utility of the novel systemic vectors demonstrated here provide a non-invasive approach to better explore the nervous system, which would lead to better therapeutic intervention. To this end, we also demonstrated that the X1 capsids can be used to genetically engineer the blood-brain barrier by transforming the mouse brain vasculature into a functional biofactory for production of therapeutic agents for CNS. We showed that vasculature-secreted Hevin (a synaptogenic protein), whose coding sequence is delivered by X1 vectors, rescued synaptic deficits in a mouse model.

AAV repeated dosing could be favorable for certain therapeutic applications, however, neutralizing antibody generated following the first injection creates major obstacle for second injection. We explored whether serotype switching with 2 AAV capsids that have a distinguished neutralizing antibody profile could be a potential solution. To this end, we firstly showed that the X1 capsid modifications translate from AAV9 to other serotypes such as AAV1 and AAV-DJ. We then combined the different engineered serotype to enable serotype switching for sequential AAV administration in mice, showing the first AAV-delivered receptor for the second AAV could boost its CNS targeting.

In general, we developed strategies to enable non-invasive functional gene delivery to the central and peripheral nervous system across species, which would be incremental for both basic neuroscience research and gene therapies for neurological disorders.

PUBLISHED CONTENT AND CONTRIBUTIONS

- **Chen, Xinhong**#, Sripriya Ravindra Kumar#, Cameron D. Adams, Daping Yang, Tongtong Wang, Damien A. Wolfe, Cynthia M. Arokiaraj, Victoria Ngo, Lillian J. Campos, Jessica A. Griffiths, Takako Ichiki, Sarkis K Mazmanian, Peregrine B Osborne, Janet R Keast, Cory T Miller, Andrew S. Fox, Isaac M. Chiu, Viviana Gradinaru*. 2022. Engineered AAVs for non-invasive gene delivery to rodent and non-human primate nervous systems. *Neuron*, 110(14), 2242-2257. https://doi.org/10.1016/j.neuron.2022.05.003

  #equal contribution. X.C. designed and performed the experiments, data analysis, and prepared the manuscript.

- **Chen, Xinhong**, Damien A. Wolfe, Dhanesh Sivadasan Bindu, Mengying Zhang, Naz Taskin, David Goertsen, Timothy F. Shay, Erin E. Sullivan, Sheng-Fu Huang, Sripriya Ravindra Kumar, Cynthia M. Arokiaraj, Viktor Plattner, Lillian J. Campos, John K. Mich, Deja Monet, Victoria Ngo, Xiaozhe Ding, Victoria Omstead, Natalie Weed, Yeme Bishaw, Bryan Gore, Ed S. Lein, Athena Akrami, Cory Miller, Boaz P. Levi, Annika Keller, Jonathan T. Ting, Andrew S. Fox, Cagla Eroglu, Viviana Gradinaru*. 2023. Functional gene delivery to and across brain vasculature of systemic AAVs with endothelial-specific tropism in rodents and broad tropism in primates. *bioRixv*, 2023.01.12.523844. https://doi.org/10.1101/2023.01.12.523844

  X.C. designed and performed the experiments, data analysis, and prepared the manuscript.

- Ravindra Kumar, Sripriya, Timothy F. Miles#, **Xinhong Chen**#, David Brown, Tatyana Dobreva, Qin Huang, Xiaozhe Ding, Yicheng Luo, Pétur H. Einarsson, Alon Greenbaum, Min J. Jang, Benjamin E. Deverman, Viviana Gradinaru*. 2020. Multiplexed Cre-dependent selection yields systemic AAVs for targeting distinct brain cell types. *Nature Methods*, 17, 541–550. https://doi.org/10.1038/s41592-020-0799-7

  #equal contribution. X.C. assisted with virus production and performed characterization of AAV variants in mice.

- Cho, Jounhong Ryan, **Xinhong Chen**, Anat Kahan, J. Elliott Robinson, Daniel A. Wagenaar and Viviana Gradinaru*. 2021. Dorsal raphe dopamine neurons signal motivational salience dependent on internal state, expectation, and behavioral context. *Journal of Neuroscience*, 41, 2645-2655. https://doi.org/10.1523/JNEUROSCI.2690-20.2021

  X.C. performed stereotaxic surgery for in vivo calcium imaging in mice and conducted animal behavior assays.

- Badimon, Ana, Hayley J. Strasburger, Pinar Ayata, **Xinhong Chen**, Aditya Nair, Ako Ikegami, Philip Hwang, Andrew T. Chan, Steven M. Graves, Joseph O. Uweru, Carola Ledderose, Munir Gunes Kutlu, Michael A. Wheeler, Anat Kahan, Masago Ishikawa, Ying-Chih Wang, Yong-Hwee E. Loh, Jean X. Jiang, D. James Surmeier, Simon C. Robson, Wolfgang G. Junger, Robert Sebra, Erin S. Calipari, Paul J. Kenny, Ukpong B. Eyo, Marco Colonna, Francisco J. Quintana, Hiroaki Wake, Viviana Gradinaru, Anne Schaefer*. 2020. Negative feedback control of neuronal activity by microglia. *Nature*, 586, 417–423. https://doi.org/10.1038/s41586-020-2777-8

  X.C. designed and performed the in vivo 2 photon imaging experiments and prepared the analysis and figure.

- Ding, Xiaozhe, **Xinhong Chen**, Erin E. Sullivan, Timothy F. Shay, Viviana Gradinaru*. 2023. Fast, accurate ranking of engineered proteins by receptor binding propensity using structural modeling. *bioRxiv*, 2023.01.11.523680. https://doi.org/10.1101/2023.01.11.523680

  X.C. engineered and characterized AAV-PHP.D.

- Challis, Rosemary C., Sripriya Ravindra Kumar, **Xinhong Chen**, David Goertsen, Gerard M. Coughlin, Acacia M. Hori, Miguel R. Chuapoco, Thomas S. Otis, Timothy F. Miles, Viviana Gradinaru*. 2022. Adeno-associated virus toolkit to target diverse brain cells. *Annual Review of Neuroscience*, 45. https://doi.org/10.1146/annurev-neuro-111020-100834

  X.C. performed the AAV experiment in rhesus macaque and contributed to the preparation of the manuscript.

- Jang, Min J., Gerard M. Coughlin, Cameron R. Jackson, **Xinhong Chen**, Miguel R. Chuapoco, Julia L. Vendemiatti, Alexander Z. Wang and Viviana Gradinaru*. 2023. Spatial transcriptomics for profiling the tropism of viral vectors in tissues. *Nature Biotechnology*, 1-15. https://doi.org/10.1038/s41587-022-01648-w

  X.C. performed AAV-PHP.AX engineering with preliminary characterization and performed the pool experiment in marmoset.

- Shay, Timothy F.#, Erin E. Sullivan#, Xiaozhe Ding#, **Xinhong Chen**, Sripriya Ravindra Kumar, David Goertsen, David Brown, Jost Vielmetter, Máté Borsos, Annie W. Lam, Viviana Gradinaru*. 2023. Primate-conserved Carbonic Anhydrase IV and murine-restricted Ly6c1 are new targets for crossing the blood-brain barrier. *bioRxiv*, 2023.01.12.523632. https://doi.org/10.1101/2023.01.12.523632

X.C. performed and analyzed AAV-PHP.eC selections, tested AAVs in wild-type mice and performed in vivo experiment to verify the role of Car4 for AAV transduction.

- Campos, Lillian J.#, Cynthia M. Arokiaraj#, Miguel R. Chuapoco, **Xinhong Chen**, Nick Goeden, Viviana Gradinaru*. 2023. Advances in AAV technology for delivering genetically encoded cargo to the nonhuman primate nervous system. *Current Research in Neurobiology*, 100086.
https://doi.org/10.1016/j.crneur.2023.100086

  X.C. provided the NHP data and contributed to the writing and editing.

- Kahan, Anat#, Alon Greenbaum#, Min J. Jang, J. Elliott Robinson, Jounhong Ryan Cho, **Xinhong Chen**, Pegah Kassraian, Daniel A. Wagenaar, Viviana Gradinaru*. 2021. Light-guided sectioning for precise in situ localization and tissue interface analysis for brain-implanted optical fibers and GRIN lenses. *Cell Reports*, 36(13), 109744. https://doi.org/10.1016/j.celrep.2021.109744

  X.C. performed stereotaxic surgery for GRIN lens implantation in mice brain.

- Chuapoco, Miguel#, Nicholas Flytzanis#, Nick Goeden#, J Octeau, Kristina Roxas, Ken Chan, Jon Scherrer, Janet Winchester, Roy Blackburn, Lillian Campos, Kwun-Nok Man, Junqing Sun, **Xinhong Chen**, Arthur Lefevre, Vikram Singh, Cynthia Arokiaraj, Timothy Miles, Julia Vendemiatti, Min Jang, John Mich, Yeme Bishaw, Bryan Gore, Victora Omstead, Naz Taskin, Natalie Weed, Jonathan Ting, Cory Miller, Benjamin Deverman, James Pickel, Lin Tian, Andrew Fox, Viviana Gradinaru* (2023). Intravenous functional gene transfer throughout the brain of non-human primates using AAV. *Nature Nanotechnology*, in press. https://doi.org/10.21203/rs.3.rs-1370972/v1

  X.C. made virus, planned, and analyzed the ex vivo adult macaque tissue characterization.

TABLE OF CONTENTS

Chapter 1

INTRODUCTION

The nervous system is critical for our life, it receives feedback and sends signals when we perform our daily tasks such as eating, drinking and sleeping. The complex cognitive function stemmed from the nervous system also creates art, music, science, and philosophy. All functions of our nervous system relies on precise regulation and synchronized action. When these complex regulations break down, it creates detrimental neurological disease conditions (Thakur et al., 2016; Ravi et al., 2021). In order to study the nervous system and tackle neurological diseases, gaining genetic access to the nervous system would be required. Recombinant adeno-associated viruses (AAVs) are becoming the delivery vector of choice for both neuroscience research and gene therapies for neurological disorders (Bedbrook et al., 2018; Deverman et al., 2018; Haery et al., 2019; Hudry & Vandenberghe, 2019; Challis et al., 2022). Direct injection has been used the most for delivery to the nervous system. However, the limited spread of the virus in big primate brain and the inflammation response to the invasive procedure makes direct administration the less ideal path for nervous system delivery (Gray et al., 2010). Systemic delivery, in the other hand, provides an attractive path to access the nervous system from the blood stream. However, systemic delivery to the nervous system remained challenging. For the central nervous system (CNS), the existence of the blood brain barrier applies high selectivity for agents to cross into the CNS. For the peripheral nervous system, the broad distribution of ganglions requires high efficiency and coverage from the delivery vector.

To enable non-invasive functional gene delivery to the nervous system, there are several key questions that need to be answered: How to engineer AAVs for efficient and specific nervous system targeting? Could the engineered AAVs be used across species? Could we use these systemic AAVs for neuronal recording and modulation? Could we use systemic AAVs for providing therapeutic agents for the nervous system? Could we enable repeated dosing of AAV if needed?

In this thesis work, I tried to tackle these key challenges and develop methods to enable functional gene delivery to the central and peripheral nervous system across species**.**

1.1 ENGINEERIG NOVEL AAVS FOR EFFICIENT AND SPECIFIC TARGETING OF THE CENTRAL AND PERIPHERAL NERVOUS SYSTEM

The lack of understanding of mechanisms behind transcytosis across BBB is one of the challenges preventing the development of efficient CNS delivery method. To that end, directed evolution, a method commonly used in protein engineering and recognized by 2018 chemistry Nobel prize, provides a viable path (Zhao et al., 1998; Arnold, 2001; Romero & Arnold, 2009). Directed evolution mimics the process of natural selection to steer proteins toward a user-defined goal by mutagenesis and applying certain type of selection pressure. It provides a goal-driven strategy to find candidates that has desired property without the knowledge of how they gained those novel properties (Arnold, 1998).

The development of directed evolution approach including CREATE (Recombinase-based AAV Targeted Evolution) has been instrumental for the engineering of novel AAVs that target the nervous system, led to the identification of PHP.B and PHP.eB, which targeted the rodent CNS efficiently with intravenous injection (Deverman et al., 2016; Chan et al., 2017). While being quite useful for identifying promising AAV capsid variants, CREATE's low throughput read out prevent the researchers from examining the candidates' comprehensive tropism and selecting for specificity. Specificity at Organ or cell-type level is a highly-desired feature for gene delivery vehicle, which would be an important engineered feature that could arise from a updated directed evolution approach with more detailed readouts. Earlier during my PhD, I contributed to the development for the second generation of CREATE, namely M-CREATE (Multiplexed Recombinase-based AAV Targeted Evolution) (Ravindra Kumar et al., 2020). The next-generation-sequencing component of the M-CREATE provide enrichment readout for the AAVs across organs and cell types.

With M-CREATE method, now one can start looking into the candidates' targeting profile for off-target cell types and organs, then selecting the candidates that have the desired efficiency and specificity. In chapter 2.3, I discuss the effort using M-CREATE to engineer AAVs against the peripheral nervous system in rodents. With 2 rounds of selection, I was able to identify 2 AAV vectors, AAV-MaCPNS1 and AAV-MaCPNS2, which shows improve targeting of the nervous system while showing reduction in off-target organ expression. In chapter 3.3, I discuss the effort to identify a novel vector, AAV-X1, which targets the brain endothelial cell specifically following systemic administration. In short, the application of M-CREATE enables us to identify novel AAV capsid variants that target the central and peripheral nervous system efficiently and specifically.

Based on the vectors identified from directed evolution, researchers could also start incorporating some rational engineering approach to further optimize their tropism. The AAV's tropism were affected by its capsid, cargo, and administration route. In chapter 3.4, I discuss the effort to further optimize AAV's tropism by rational cargo engineering and capsid engineering. Cargo engineering with added target site of microRNA naturally expressed in liver enabling us to silence the AAV genome in liver. Rational capsid engineering with modification in complimentary sites and active site mutagenesis enable us to further boost the vector's brain targeting while reducing off target expression. These further enhanced vectors laid the ground for further testing and application across species.

1.2 TESTING OF DELIVERY VECTORS ACROSS MODELS AND SPECIES

When it comes to directed evolution, a famous saying is 'you get what you select for'. When the selection process is carried out in certain species, the selected candidate gains new property that enable them to perform well in this specie. However, this gained property may be unique to the species they were selected in thus hampering the translatability of the candidates across other species. Some AAV vectors coming out of previous directed evolution were also shown to be no exception to this phenomenon. PHP.eB, a vector mentioned above, was selected in C57 mice and target brain efficiently following intravenous injection in several mice strain. When being tested in some other mice strain including BalbC, however, it failed to cross BBB efficiently (Challis et al., 2019; Hordeaux et al., 2019; Huang et al., 2019; Matsuzaki et al., 2019). Further testing of PHP.B in non-human primate species also fail to show improvement in CNS targeting (Liguore et al., 2019). Given this uncertainty for transability across species, it is important to test the engineered AAV across species and models that are relevant to future application. These would include rodent, non-human primates, and human tissue.

For testing across rodents, in chapter 2.6 and chapter 3.5, I discuss the effort to test the engineered AAVs across mice strains and rat. I show the translatability of the vectors' performance across species. MaCPNS1 and MaCPNS2 transduce peripheral nervous system efficiently across rodent species while X1 family transduce the brain endothelial specifically across rodent species.

For testing across non-human primates, this became more challenging due to the limited availability of the animals. An ex vivo platform that could mimic the *in vivo* condition of primate and enable high-throughput testing would be an ideal platform. With an *ex vivo* platform, one could also test the engineered candidates in tissue from human biopsy. Allen Brain Institute previously developed a platform using ex vivo brain slices derived from non-human primates or adult human neurosurgically-excised tissue to probe the structure and function of living brain by applying standard procedures originally optimized for rodent neurophysiology research (Ting et al., 2018). In chapter 3.9, I utilize this platform to test a series of AAVs including the engineered vector AAV-X1.1, showing its superior performance over other CNS AAVs in this system. To further verify top candidates' performance *in vivo*, in chapter 2.7, chapter 2.8, and chapter 3.10, I discuss the work to test the engineered vectors across non-human primates including marmoset and macaque *in vivo*. For MaCPNS1 and MaCPNS2, they not only transduced the peripheral nervous system efficiently but also crossed the BBB and targeted brain efficiently in both marmoset and macaque. For X1 vectors, we also observed enhanced neuron targeting in the non-human primate. This difference in tropism between rodent and non-human primate again highlights the need for testing across species. This comprehensive understanding of their respective tropism in key model and species provide more confidence in future application in those models.

1.3 USING SYSTEMIC AAVS FOR FUNCTIONAL READOUT AND NON-INVASIVE NEURONAL MODULATION

With lots of unsolved scientific questions in the nervous system, the ability to record neuronal function and modulate neuronal activity is the key to tackle them. For the monitoring of neuronal function, scientists have developed a series of sensors such as GECI (genetic encoded calcium sensor) and neurotransmitter sensor (Dong et al., 2022). For the modulation of neuronal function, scientists have developed methods such as chemogenetics or optogenetics (Fenno et al., 2011; Sternson & Roth, 2014). With the development of all these amazing sensors and actuators, the efficient delivery of them to the nervous system becomes critical.

Delivery through blood stream provided a non-invasive path to access the nervous system. However, systemic delivery of nature AAV serotypes suffers from low MOI (multiplicity of infection), leading to the inadequate expression level of the sensor and actuator. With the novel systemic AAVs we develop, we could start to see whether we could achieve functional readout and non-invasive neuronal modulation with them. In chapter 2.5, I discuss the work using systemic MaCPNS1-mediated sensor and actuator expression to enable functional characterization of neurons in nodose ganglia (NG) and dorsal root ganglia (DRG). We observed specific NG neuronal responses to physiological modulation in the gut with MaCPNS1-delivered GCAMP. We developed a pain model with MaCPNS1-mediated

DREADD expression in DRG. These provide the first proof-of-concept cases for the application of systemic AAVs in functional readout and non-invasive neuronal modulation. The cross-species potential we observed in these AAVs would also enable similar application in understanding the nervous system in other species such as non-human primates.

1.4 USING SYSTEMIC AAVS TO CREATE BIOFACTORY FOR PROVIDING THERAPEUTICS FOR THE NERVOUS SYSTEM

Our goal of developing better gene delivery vectors for the nervous system is to tackle a variety of neurological diseases. The key component of that is to provide therapeutic proteins for the nervous system. The traditional approach is to target the diseased cell type directly and enable them to express the therapeutic protein for themselves. However, the diseased cell type may already be under great disease burden and may be challenging for them to be transduced and produce enough therapeutic agents. *In vivo* biofactory, on the other hand, could be a potential solution to circumvent this obstacle. An *in vivo* biofactory would use the 'bystander effect'. The 'bystander' would produce the therapeutic proteins and secret them out for the diseased cell types. In the CNS, the brain endothelial cells would be a good 'bystander'. The vasculature is broadly distributed across the brain and in close proximity to other cell types in the brain. I thus introduce the idea of transforming the brain endothelial cells as a biofactory producing therapeutic agents for the CNS.

In chapter 3.7, I discuss the work to use the X1.1 vector to transform brain endothelial cells into a biofactory for secreted protein delivery to the brain. The X1.1-mediated expression of synaptic protein Hevin in the endothelial cells were secreted out and rescued the synaptic loss phenotype in the Hevin KO mice. In general, this demonstrates a novel strategy to provide therapeutic protein to the nervous system that could potentially be applied to many types of neurological diseases.

1.5 REPEATED ADMINISTRATION OF AAVS

For the application of AAV, sometimes repeated dosing is needed to further boost the transgene's expression. However, this has been challenging due to the presence of neutralizing antibody induced by the first injection (Mingozzi & High, 2017; Ronzitti et al., 2020). When AAV is administrated, it was taken up by the macrophages and processed. The AAV capsid-deprived peptides were then presented and activated T cells as well as B cells. The activation of the immune response eventually led to the generation of B memory cells. When similar AAV is administrated again, those memory B cells would recognize the similar antigen pattern and proliferate into plasma cells, producing neutralizing antibody (Nabs) to neutralize the second dosing of AAV (Hamilton & Wright, 2021). The presence of neutralizing antibody is persistent for a long duration after the first administration. Long-Term Follow-Up of the First in Human Intravascular Delivery of AAV for Gene Transfer (AAV2-hFIX16 for Severe Hemophilia B) showed the persistence of high-titer, multi-serotype cross-reactive AAV NAbs for up to 15 years post-AAV vector administration (Mingozzi & High, 2017; George et al., 2020). This adaptive immune response process created huge obstacles for repeated AAV dosing.

There are several strategies involving immune suppressants in development to enable repeated AAV administration, however, most of those strategies involve extra procedures other than the gene therapy itself and could also bring potential side effects (Chu & Ng, 2021; Li et al., 2022). One strategy called 'serotype switching' was also proposed to be an alternative for tackling this challenge. Serotype switching, as its name indicates, combines different AAV serotypes during therapy. The lack of cross-reactivity of the Nabs against one serotype versus the other serotype provides the opportunity for second dosing (Majowicz et al., 2017). For this path, 2 serotypes with similar tropism would be desired for repeated targeting of the same tissue. However, it is rare to find 2 serotypes that have similar tissue tropism outside the liver while having different Nab profiles. In general, development of novel engineered AAV serotypes that exhibit similar tissue tropism while differ in Nab profiles is a key to enable AAV repeated administration.

In Chapter 3.6, I describe my effort to engineer novel AAV serotypes that have different nature serotype parents while having similar specific targeting of brain vasculature upon systemic administration. The development of those vectors enabled me to demonstrate serotype switching as a strategy for AAV repeated dosing. With this strategy, I delivered the first AAV to express the unique receptor required for the second AAV to cross BBB, thus enhancing the BBB permeability for the second AAV. This does not only show the first demonstration of AAV repeated systemic administration targeting the brain but also provides a novel strategy to expand the application of novel AAVs in animals that do not naturally express the receptors required. This strategy laid the ground for our future work in developing more receptor-targeted delivery modalities.

Chapter 2

ENGINEERED AAVS FOR NON-INVASIVE GENE DELIVERY TO RODENT AND NON-HUMAN PRIMATE NERVOUS SYSTEMS

Chen, Xinhong[#], Sripriya Ravindra Kumar[#], Cameron D. Adams, Daping Yang, Tongtong Wang, Damien A. Wolfe, Cynthia M. Arokiaraj, Victoria Ngo, Lillian J. Campos, Jessica A. Griffiths, Takako Ichiki, Sarkis K Mazmanian, Peregrine B Osborne, Janet R Keast, Cory T Miller, Andrew S. Fox, Isaac M. Chiu, Viviana Gradinaru*. 2022. Engineered AAVs for non-invasive gene delivery to rodent and non-human primate nervous systems. *Neuron*, 110(14), 2242-2257. https://doi.org/10.1016/j.neuron.2022.05.003

[#]*equal contribution.*

2.1 SUMMARY

Gene therapy offers great promise in addressing neuropathologies associated with the central and peripheral nervous systems (CNS and PNS). However, genetic access remains difficult, reflecting the critical need for development of effective and non-invasive gene delivery vectors across species. To that end, we evolved adeno-associated virus serotype 9 (AAV9) capsid in mice, and validated two capsids, AAV-MaCPNS1 and AAV-MaCPNS2, across rodent species (mice and rats) and non-human primate (NHP) species (marmosets and rhesus macaques). Intravenous administration of either AAV efficiently transduced the PNS in rodents, and both the PNS and CNS in NHPs. Furthermore, we used AAV-MaCPNS1 in mice to systemically deliver: (1) the neuronal sensor jGCaMP8s to record calcium signal dynamics in nodose ganglia, and (2) the neuronal actuator DREADD to dorsal root ganglia to mediate pain. This conclusively demonstrates the translatability of these two systemic AAVs across four species, and their functional utility through proof-of-concept studies in mice.

2.2 INTRODUCTION

Gene delivery to the central and peripheral nervous systems (CNS and PNS) has greatly accelerated neuroscience research in the last decade, and has the potential to translate this research into novel therapies for neurological disorders. However, the lack of potent vectors enabling non-invasive gene delivery across species is a significant bottleneck that can hinder fast progress (Ingusci et al., 2019; Pena et al., 2020; Piguet et al., 2021).

The success of gene delivery relies on a safe and efficient vector, and for this reason, most *in vivo* applications use adeno-associated viral (AAV) vectors. AAVs offer several advantages, including stable, long-term transgene expression and low immunogenicity (Bedbrook, Deverman, and Gradinaru, 2018; O'Carroll, Cook, and Young, 2021). The natural serotypes of AAV have demonstrated considerable success in targeting different cell populations within the nervous system through direct routes of gene delivery, such as intracranial (Golebiowski et al., 2017; GuhaSarkar et al., 2017), intracerebroventricular (ICV) (Bey et al., 2020), intrathecal (Hirai et al., 2012), intraganglionic (Yu et al., 2013), intrasciatic (Homs et al., 2011) and intracolonic (Gore et al., 2019). These direct delivery routes suffer from limitations, however, including the need for invasive surgery. In addition, anatomical barriers may restrict surgical access (such as for nodose ganglia (NG) or dorsal root ganglia (DRG)). Finally, localized delivery can lead to incomplete coverage of a large complex system such as the enteric nervous system (ENS) or CNS, and multiple direct interventions may be needed to increase coverage (Gray, Woodard, and Samulski, 2010).

An alternative, non-invasive, intravenous (IV) route circumvents these limitations. Some natural serotypes, including AAV9, can target the CNS or PNS systemically. However, lack of specificity towards the target and low efficiency, necessitating high vector load, both potentially lead to toxicity issues (Bourdenx et al., 2014; B. Yang et al., 2014; Vogt et al., 2015; Gombash et al., 2017). Years of capsid engineering efforts have now yielded a toolbox of improved CNS capsids for rodents (Deverman et al., 2016;

Körbelin et al., 2016; Ojala et al., 2018; Ravindra Kumar et al., 2020; Nonnenmacher et al., 2021). These include the potent vector AAV-PHP.eB (engineered using CREATE) for the CNS, but its application is restricted to select mice strains (Deverman et al., 2016; Chan et al., 2017; Hordeaux et al., 2018; Matsuzaki et al., 2018; Hinderer et al., 2018). Unlike PHP.B/eB, the recently engineered AAV-F (engineered using iTransduce) and AAV-PHP.Cs (engineered using Multiplexed-CREATE or M-CREATE) for the CNS work across mouse strains (Hanlon et al., 2019; Ravindra Kumar et al., 2020). However, the heterogeneity of the blood-brain barrier (BBB) depending on genetic background has posed a significant challenge for developing capsids that have the potential to translate across species (Hordeaux et al., 2019; Q. Huang et al., 2019; Batista et al., 2020). This issue is particularly acute for non-human primates (NHPs), which are commonly used as pre-clinical research models for gene therapy (Kimura and Harashima, 2020; Piguet et al., 2021). With several CNS&PNS-based therapies in the pipeline, there is therefore a high demand for next-generation systemic AAV vectors with potent neurotropic behavior in order to achieve efficient and safe gene delivery for translational applications (Deverman et al., 2018; Tosolini and Smith, 2018; Hudry and Vandenberghe, 2019; W. Chen et al., 2021; L. Huang et al., 2021; Challis et al., 2022).

Building on our success selecting improved CNS-targeting capsids using M-CREATE (Ravindra Kumar et al., 2020; Goertsen et al., 2021), we decided to test the potential of this method for selecting improved PNS-targeting capsids outperforming the prior engineered variant, AAV-PHP.S, which requires a high dose to exhibit its potent PNS tropism via IV delivery (Chan et al., 2017). Compared to the CNS, the PNS is a more challenging AAV engineering target. Cell populations are sparser, and there is no strong source of selection pressure across targets (akin to the BBB for the CNS). M-CREATE is uniquely well suited to this problem as it capitalizes on deep recovery of capsid libraries across cell-types/organs to select capsids enriched in areas of interest, and a customized analysis pipeline that incorporates positive and negative selections to help identify variants with desired properties.

In this study, we used M-CREATE to identify a family of 7-mer containing AAV9 capsids that appeared to be biased towards PNS areas, and detailed the properties of two such selected AAVs, AAV-MaCPNS1 and AAV-MaCPNS2, in rodents and NHPs. We provide *in vivo* validation of their tropism in mice, and demonstrate their potential applications with proof-of-concept studies for functional readout and modulation of sensory ganglia. In addition to finding improved PNS-targeting capsids, we sought to address the fundamental question of the translatability of capsids selected in mouse models. To this end, we examined these capsids across four species commonly used in basic through pre-clinical applications: mice, rats, marmosets, and rhesus macaques. The variants discussed in this study show improved efficiency and specificity towards the PNS, and translate their potent behavior across mammalian species. Interestingly, and potentially due to the heterogeneity of the BBB, these variants also show efficient crossing of the BBB to infect the CNS in NHPs (Table S1).

2.3 AAV CAPSID SELECTION IN MICE IDENTIFIES TWO AAV VARIANTS WITH PNS SPECIFICITY

As a starting point for capsid engineering, we chose AAV9 due to its broad tropism when delivered systemically, including for the nervous system (both CNS and PNS) (Foust et al., 2009; Bevan et al., 2011). We diversified the AAV9 capsid by inserting a randomized 7-mer peptide between positions 588 and 589 (Fig. 1A), and intravenously injected the resulting virus library into adult mice of three Cre-transgenic lines: SNAP-Cre (for neurons), GFAP-Cre (for glia), and Tek-Cre (for endothelial cells forming the blood-organ barrier). Two weeks post-injection, we processed peripheral tissues (such as heart, small and large intestines, and DRG) and selectively extracted viral genomes from Cre+ cells using Cre-dependent PCR (see Methods, Fig. 1A-2).

After round-1 (R1) selection, we recovered a total of ~9,000 variants from the Cre lines in the PNS tissues of interest: heart, DRG, small and large intestine. Of these, ~10% overlapped with the CNS libraries (Fig. 1A-3). We then synthesized these variants in an equimolar ratio to create a synthetic oligopool library for round-2 (R2) PNS selection. This synthetic pool also included a spike-in library of previously-validated internal controls (see Methods). We intravenously injected the R2 virus library into different Cre lines: Nestin-Cre (for neurons), CHAT-Cre (for cholinergic neurons), TRPV1-Cre (for primary afferent thermosensitive neurons), and Tek-Cre (for endothelial cells, providing a negative selection). Two weeks post-injection, we selectively recovered capsids by Cre-dependent PCR from tissues of interest (DRG, heart, small and large intestine, brain, and spinal cord (SC)), and other targets (spleen, liver, lung, kidney, testis and muscle) by performing Cre-independent PCR (see Methods, Fig. 1A-4, 1B).

After two rounds of *in vivo* selection, among all the variants that we included in the R2 library, 6,300 variants showed a bias towards one or more of the PNS tissues (Fig. 1B, Supplementary Fig. 1A). We next sought to further classify the recovered variants based on distinct tropisms. We used the Uniform Manifold Approximation and Projection (UMAP) algorithm (McInnes, Healy, and Melville, 2020), which takes into account differences among variants' enrichments across organs, to identify clusters of variants representing distinct tropisms (Fig. 1C, top panel). Members of Cluster-1 (1,846 variants), which includes AAV9, show relatively higher enrichment in off-target tissues such as the liver (Fig. 1C, bottom left panel). Cluster-2 members (7,148 variants), including our previously engineered variant PHP.S, exhibit relatively higher enrichment in the PNS and lower enrichment in off-target tissues (Fig. 1C, bottom right panel). Cluster-3 members (5 variants), including variants from the internal control, were highly enriched in the CNS.

Based on this analysis, we reasoned that Cluster-2 might contain promising variants distinct from the parental AAV9, which we indeed observed by comparing their tropism directly to that of AAV9 (Fig. 1D). We identified two new capsids from Cluster-2 that exhibited low off-target transduction compared to AAV9 and PHP.S (Fig. 1E) and that could package viral genomes with similar efficiency to AAV9 (see Methods, Supplementary Fig. 1B). The first capsid, with a 7-mer peptide insertion of PHEGSSR between the 588-89 residues of the AAV9 parent, we will henceforth refer to as AAV-

MaCPNS1. The second, with an insertion of PNASVNS, we will refer to as AAV-MaCPNS2 (Fig. 1F).

2.4 IV-DELIVERED AAV-MACPNS1/2 EFFICIENTLY TRANSDUCES SENSORY AND ENTERIC GANGLIA IN MICE, WITH LOW LIVER TRANSDUCTION

To characterize the transduction capability of AAV-MaCPNS1 and AAV-MaCPNS2 variants *in vivo*, we packaged these variants with a single-stranded (ss) AAV genome carrying a strong ubiquitous promoter, CAG, driving expression of nuclear-localized eGFP reporter and intravenously injected them into adult mice at $3x10^{11}$ vg per animal (Fig. 2A-H,J-L; see Methods). By quantifying expression in nodose ganglia (NG) that overlapped with the NeuN neuronal marker, we found that MaCPNS1 and MaCPNS2 had mean transduction efficiencies of ~28% and ~35%, respectively. By comparison, the efficiency of AAV9 was ~16%, and AAV-PHP.S ~12% (Fig. 2B-C). Thus, MaCPNS1/2 capsids exhibit about 2-fold higher transduction of NG than previously available vectors.

Next, we investigated the efficiency of DRG transduction from selected spinal levels (thoracic and lumbar). The MaCPNS1 vector demonstrated a mean transduction efficiency of ~18%, and MaCPNS2 ~16%, compared to ~11% for AAV9 and ~7% for AAV-PHP.S (Fig. 2B bottom panel, 2D, left), with some variability in transduction across different segments of the SC (Fig. 2D, right). Thus, compared to known capsids, MaCPNS1/2 can achieve about 2-fold higher transduction of DRG via IV delivery. Increasing the vector dose to $1x10^{12}$ vg, we observed that PHP.S had higher transduction in DRG compared to AAV9 while MaCPNS1 exhibited even higher transduction (Supplementary Fig. 2A-C), further confirming that MaCPNS1/2 capsids transduce DRG in adult mice more efficiently than either AAV9 or PHP.S.

To investigate the transduction efficiency of the new vectors in the ENS, we assessed AAV-mediated eGFP expression in the enteric ganglia of the myenteric plexus across different areas of the GI tract-stomach, duodenum, jejunum, ileum, proximal colon, and cecum (Fig. 2E-F). We observed a mean transduction efficiency of ~8% by MaCPNS1,

~17% by MaCPNS2, ~13% by PHP.S and ~12% by AAV9 (Fig. 2F). By analyzing individual GI segments, we noticed variability in transduction of enteric ganglia, with a bias of MaCPNS2 transduction towards small intestinal (SI) segments (duodenum, jejunum and ileum) over other areas, indicating a modest improvement in SI ENS transduction by MaCPNS2 compared to other vectors. To more closely examine this SI bias, we slightly lowered the vector dose to $1x10^{11}$ vg and observed a 2-fold increase in transduction of the SI by MaCPNS2 compared to AAV9 (Fig. 2G-H). Next, we investigated if the transduction efficiency across large intestinal (LI) segments could be improved by a higher dose (Fig. 2I, Supplementary Fig. 2D). Compared to the initial dose of $3x10^{11}$ vg, we observed that a MaCPNS2 dose of either $5x10^{11}$ vg or $7x10^{11}$ vg achieved robust and uniform transduction of the enteric ganglia of the myenteric plexus in the proximal colon as well as sparser transduction in the distal colon. Thus intravenously-administered MaCPNS2 offers improved transduction of enteric ganglia in the SI, with the option of additional targeting of LI segments at higher doses.

To investigate the liver transduction of MaCPNS1/2 capsids, we assessed eGFP expression *in vivo* (Fig. 2J-L). MaCPNS1 exhibited 1.5-fold lower transduction compared to the same dose of AAV9 or PHP.S (Fig. 2K). Quantifying the mean brightness of the eGFP fluorescence signal revealed that the new vectors also exhibited 1.3- to 2.1-fold lower signal compared to AAV9 or PHP.S (Fig. 2L), suggesting reduced transgene expression per cell. Collectively these data suggest that MaCPNS1 exhibits lower transduction of hepatocytes and lower transgene expression per liver cell compared to other vectors used for PNS. In addition to the liver, we also investigated other tissues, including the CNS, given AAV9's ability to cross the BBB. At a modest IV dose of $3x10^{11}$ vg, CNS transduction was low for all vectors we tested, including AAV9 (Supplementary Fig. 2E). Even when we increased the dose of MaCPNS2 to $5\text{-}7x10^{11}$ vg, we did not observe CNS transduction in mice (Supplementary Fig. 2F). In addition, MaCPNS1/2 transduction of cardiac muscle was similar to that of AAV9 (Supplementary Fig. 2E).

All of the above experiments were conducted in adult mice. However, many potential applications require early age intervention (Gray, 2016; Privolizzi et al., 2021; Ali et al., 2021). We therefore investigated MaCPNS1/2 transduction in DRG in neonates using an alternative delivery route. We introduced MaCPNS1/2 capsids packaged with ssAAV:hSyn-tdTomato into postnatal stage 1 (P1) mice via intraperitoneal (IP) injection, with a dose of $3x10^{11}$ vg per mouse. After 6 weeks of expression, MaCPNS1 transduced ~39% of neurons (marked with Tuj1) in DRG and MaCPNS2 transduced ~35%, including ~55% of all CGRP+ neurons and ~19% of all NF200+ neurons (Supplementary Fig. 2G-I). Examining targeting preference, we found that the capsids were predominantly targeting two types of neurons: about 60% of transduced neurons were CGRP+ and ~11% NF200+ (Supplementary Fig. 2J).

In summary, we found that systemic delivery of MaCPNS1 and MaCPNS2 vectors in mice can efficiently transduce sensory ganglia (such as NG and DRG) compared to AAV9, with MaCPNS2 distinguished from MaCPNS1 by enhanced transduction of the ENS. Further, MaCPNS1 and MaCPNS2 exhibited improved specificity for the PNS, with relatively lower transduction of AAV9's primary target, the liver.

2.5 SYSTEMIC MACPNS1-MEDIATED SENSOR AND ACTUATOR EXPRESSION ENABLE FUNCTIONAL CHARACTERIZATION OF NEURONS IN NODOSE GANGLIA AND DORSAL ROOT GANGLIA.

Functional readout of PNS activity during physiological conditions is key to understanding the interaction between the brain and peripheral system (R. Chen, Canales, and Anikeeva, 2017; Zanos et al., 2018; Walters et al., 2019; Jiman et al., 2020). However, commonly-used imaging with genetically encoded calcium indicators (GECIs) in the CNS has been challenging in the PNS due to the low efficiency of delivering GECI to PNS targets. To test the applicability of MaCPNS1/2 capsids to this problem, we intravenously delivered MaCPNS1 capsid packaged with a recently-developed GECI, jGCaMP8s (Zhang et al., 2020), to adult mice. After three weeks of expression, we recorded calcium signals *in vivo* during procedures on the gut (Fig. 3A-C). We infused the gut with either glucose solution or saline (to induce distension) while recording neuronal activity in the NG of the anesthetized mice and observed distinguishable neuronal responses in NG (Fig. 3A-C). No significant expression was observed in the CNS or liver of these mice.

After verifying the new vectors' potential for enabling functional readout of the PNS, we took the further step of seeing whether we could achieve functional modulation with the vectors. We sought to construct a mouse pain-induction system with improved temporal control, a critical tool for understanding and potentially managing pain. To activate DRG TrpV1 neurons, we packaged Cre-dependent excitatory Designer Receptors Exclusively Activated by Designer Drugs (DREADD) (Krashes et al., 2011) into MaCPNS1 and intraperitoneally injected the vector into P1 TRPV1-Cre pups (Fig. 3D). After 6 weeks of expression (Fig. 3E), we gave mice an intraplantar injection of the DREADD agonist clozapine N-oxide (CNO) and evaluated resulting pain-like behaviors (see Methods). We observed an increase in the number of bouts and overall time spent lifting or licking the injected footpad in the experimental AAV-administered group compared to the control group, indicating nocifensive pain-like behavior (Fig. 3F-G).

Together, these results provide a proof of concept for the application of these new vectors to a wide range of studies involving the monitoring and modulation of sensory processes, including pain.

2.6 IV-ADMINISTERED AAV-MACPNS1/2 EFFICIENTLY TRANSDUCES THE PNS IN ADULT RATS

Having validated the new variants' transduction profiles in mouse models, we next investigated their efficacy in another common research model system, rats. Systemic delivery of MaCPNS1/2 capsids packaged with ssAAV:hSyn-tdTomato in Sprague Dawley adults (Fig. 1A) transduced sensory ganglia (DRG and trigeminal ganglia (TG)), sympathetic chain ganglia (SCG), parasympathetic ganglia (inferior mesenteric ganglia (IMG)), mixed sympathetic-parasympathetic ganglia (the major pelvic ganglion (MPG)), and enteric ganglia across the SI and LI (Fig. 4A-F, Supplementary Fig. 3A-B). The majority of cells transduced in both DRG and TG were NF200+ (about 70-75%), with only 5% either CGRP+ or TRPV1+ (Fig. 4C-D). In terms of efficiency, both capsids transduced ~22% of the NF200+ cells in DRG, and 15%-17% of the NF200+ cells in TG (Fig. 4E). Interestingly, this cell type bias contrasts with what we observed in neonatal mice, where the vectors showed a bias towards CGRP+ neurons (Supplementary Fig. 2I-J). This profile could result from differences in species or age/time of injection, as well as the different systemic routes of vector delivery (similar tropism shifts have been reported elsewhere (Foust et al., 2009)). The tropism diversity highlights the necessity of considering all relevant experimental variables to achieve the desired transduction profile.

The vectors' efficient labeling of sensory ganglia prompted us to look further into the ENS (Fig. 4F, Supplementary Fig. 3C). Analyzing segments of the SI and LI, we found that MaCPNS1 and MaCPNS2 were comparable at transducing the myenteric plexus and the submucosal plexus, including the vascular and periglandular plexuses. Next, we investigated projections to the SC and brainstem (Fig. 4G, Supplementary Fig. 3D). Sensory nerve fibers entering the dorsal horn of the SC were densely labeled, and the ascending afferent tracts in the dorsal column were also strongly transduced by both virus vectors. In the brainstem, fibers were densely labeled in the spinal trigeminal nucleus oralis (Sp5O), which potentially projected from the TG. In addition to the transduction in the PNS and the nerve projections labeling in the CNS, we also observed some labeling of neuronal cell bodies across regions in the brain (Supplementary Fig. 3D). Furthermore, we observed no expression in the liver (Supplementary Fig. 3E).

Together, these results show that the potent PNS tropism of the MaCPNS1/2 vectors is conserved across rodent models tested.

2.7 IV-DELIVERED AAV-MACPNS1/2 TRANSDUCES THE ADULT MARMOSET CNS AND PNS MORE EFFICIENTLY THAN AAV9

Novel capsids selected in mice do not always translate to NHPs (Hordeaux et al., 2018; Matsuzaki et al., 2018). After validating the MaCPNS1/2 capsids in mice and rats, we therefore decided to assess their performance in NHPs. We first chose the marmoset, a New World monkey and an emerging animal model for translational research. Owing to the limited availability of these animals, in each adult animal we tested two viral capsids (AAV9, MaCPNS1 or MaCPNS2) packaging different fluorescent reporters (either ssAAV:CAG-eGFP or ssAAV:CAG-tdTomato) (Fig. 5A). Compared to the parent AAV9, intravenously-delivered MaCPNS1/2 capsids carrying either ssAAV:CAG-eGFP or ssAAV:CAG-tdTomato genome showed robust transduction of the PNS and the CNS. In the PNS, we observed enhanced transduction of DRG, the SI and the ascending fiber tracts in the dorsal column of the SC (Fig. 5B-D), similar to what we observed in rodents. In the CNS, robust brain-wide transduction by MaCPNS1/2 capsids, but not AAV9, was evident in regions including the cortex, thalamus, globus pallidus, cerebellum and brainstem (Fig. 5E-F). Further antibody staining and quantification revealed that capsids mainly transduce neurons and astrocytes in the marmoset brain. In the marmoset cortex, MaCPNS2 displayed a ~5.5-fold increase in neuronal transduction over AAV9 while MaCPNS1 displayed a ~4-fold increase over AAV9 (Supplementary Fig. 4A-C). Among the neurons transduced, few overlapped with the PV marker, indicating the vectors' potential bias to excitatory population (Supplementary Fig. 4D). For astrocyte transduction, MaCPNS2 displayed a ~25-fold increase over AAV9 in cortex (Supplementary Fig. 4B). Similar improvement in both neuronal and astrocytic transduction was also observed in the thalamus (Supplementary Fig. 4C).

These results demonstrate that the MaCPNS1/2 capsids can efficiently cross the BBB in adult marmosets, while still exhibiting the enhanced PNS tropism observed in rodents.

2.8 IV-DELIVERED AAV-MACPNS1/2 TRANSDUCE THE INFANT RHESUS MACAQUE CNS AND PNS MORE EFFICIENTLY THAN AAV9

Encouraged by the tropism of MaCPNS1/2 capsids in marmosets, we further assessed their transduction potential in another NHP, the rhesus macaque, an Old World monkey and a common pre-clinical research model for AAV gene therapy. We employed the same strategy as in marmosets, intravenously administering AAV9, MaCPNS1 and MaCPNS2 capsids packaging either ssAAV:CAG-eGFP or ssAAV:CAG-tdTomato to an infant rhesus macaque (Fig. 6A). Similar to our results in marmosets, we observed that MaCPNS1/2 efficiently targeted both the CNS and PNS compared to the parent AAV9 after three weeks of expression. We saw enhanced transduction in the SC, DRG and GI tract, including the esophagus, colon and SI (Fig. 6B-D), as observed in rodents and marmosets. In the SC, there was strong labeling of both ascending fiber tracts in the dorsal column as well as the peripheral fiber tracks coming into the dorsal horn. Within the grey matter of the lumbar SC, MaCPNS1 displayed a ~25-fold increase in neuronal transduction over AAV9. For non-neuronal cells, MaCPNS2 displayed a ~130-fold increase in transduction over AAV9 (Supplementary Fig. 5A-B). Similar improvement in transduction was also observed in the thoracic SC (Supplementary Fig. 5C-D). In the lumbar and thoracic DRG, MaCPNS2 displayed ~77-fold and ~44-fold increases in neuronal transduction over AAV9, respectively. MaCPNS1 also showed ~37-fold and ~22-fold increases in neuronal targeting in lumbar and thoracic DRG. Within lumbar DRG (Supplementary Fig. 5E), MaCPNS2 was highly specific to neurons, with ~94% of all transduced cells being neurons. In thoracic DRG, both vectors displayed high specificity in targeting neurons (Supplementary Fig. 5F). In the CNS, MaCPNS1/2 capsids mediated enhanced brain-wide transduction including in areas such as the cortex, hippocampus, putamen and brainstem (Fig. 6E-F, Supplementary Fig. 6, Video S1-4), similar to our observations in marmosets. Both vectors transduced neurons and astrocytes but not oligodendrocytes or endothelial cells (Supplementary Fig. 7A-B). In the macaque cortex, neuron transduction by MaCPNS1 and MaCPNS2 was ~6-fold and ~11-fold higher, respectively, than AAV9 (Supplementary Fig. 7B). Most neurons transduced by both vectors were PV-, indicating a potential bias to excitatory populations (Supplementary Fig. 7D). MaCPNS2 also displayed a ~44-fold increase in astrocyte transduction over AAV9 in cortex (Supplementary Fig. 7B). A similar improvement in neuronal and astrocytic transduction was also observed in the thalamus (Supplementary Fig. 7C). Consistent with our observations in marmoset, MaCPNS1's transduction was more biased towards neurons while MaCPNS2 showed increased transduction of both neurons and astrocytes. No significant difference in liver transduction was observed between MaCPNS1, MaCPNS2 and AAV9 (Supplementary Fig. 6).

These experiments demonstrate that the new capsids, MaCPNS1/2, can efficiently transduce the PNS and CNS in both New and Old World monkeys, making them useful vectors for translational research across the nervous system.

2.9 DISCUSSION

In this study, we describe systemic AAVs which address the pressing need for efficient gene delivery vectors to target the nervous system across species. By *in vivo* selection and data analysis, we identified a library of capsids with divergent tropism compared to their parent, AAV9. Two variants, MaCPNS1 and MaCPNS2, were noteworthy for their potent neurotropic behavior in the mouse model in which they were selected. In contrast to our previously-engineered PNS-targeting variant, AAV-PHP.S, which requires a high dose to be potent, intravenous delivery of a modest dose of the new variants in adult mice showed about 2-fold improvement in the transduction of NG and DRG compared to AAV9. In addition to improved sensory ganglia transduction, the MaCPNS2 capsid showed improved transduction of the SI of the ENS. These MaCPNS1/2 capsids also stood out from AAV9 and PHP.S in their specificity for the PNS, with lower transduction in the liver. In addition to their performance in adult mice, the new vectors efficiently transduced DRG when delivered at the P1 neonatal stage in mice, via a technically easy intraperitoneal injection. In neonatal mice, both vectors showed a significant bias towards transducing CGRP+ neurons.

Experiments involving functional readout or modulation in the sensory system require a high copy-number of functional proteins. This can be challenging to achieve with systemic delivery, and is thought to require a combination of both an efficient vector and an engineered genetic indicator/probe (Bedbrook et al., 2019; Michelson, Vanni, and Murphy, 2019; Grødem et al., 2021). In this study, we demonstrate that it is possible to use the new MaCPNS1 capsid systemically for both monitoring and modulating neuronal function. By systemically delivering a recently engineered GECI, jGCaMP8s, we were able to visualize vagal neuron calcium dynamics in response to gut glucose infusion and distension. By demonstrating the use of viral vector-mediated GECI delivery for imaging in wild-type mice, we highlight the possibility of performing similar imaging studies in species where transgenic models may not be available. Following our success with GECI sensor delivery, we extended the application of the MaCPNS1 vector to systemic delivery of a DREADD actuator to a TrpV1-Cre neonate, enabling pain induction by chemogenetic modulation of TrpV1+ neurons in DRG, which mediate thermosensation and pain (Cavanaugh et al., 2011; Mishra et al., 2011; Pogorzala, Mishra, and Hoon, 2013). These proof-of-concept experiments demonstrate the potential of MaCPNS1/2 for modulating different sensory modalities with higher temporal resolution. With the rapid development of ultra-sensitive opsins (Bedbrook et al., 2019; Gong et al., 2020) and a wireless light source (Yang et al., 2021), these newly-developed AAV variants could potentially open the door to less invasive modulation of hard-to-access peripheral ganglia with precise temporal control.

MaCPNS1 and MaCPNS2 also show promise in rats, another commonly used research model for PNS applications (Ravagli et al., 2020; Draxler et al., 2021). Both capsids translated their potent PNS tropism across rodents, showing efficient transduction of sensory ganglia, sympathetic ganglia, parasympathetic ganglia, and enteric neurons. Detailed cell-type characterization in DRG and TG of adult rats showed that the vectors were biased towards transducing NF200+ neurons, in contrast to the bias towards CGRP+ neurons we observed in DRG in mice injected intraperitoneally at the neonate P1 stage. Such tropism shifts have been previously noted with other AAV serotypes, and emphasize the importance of considering the roles various experimental conditions play in determining a vector’s tropism in a given animal model (Foust et al., 2009; Matsuzaki et al., 2018).

The conservation of the vectors' potent PNS tropism across rodents prompted us to test their performance in NHPs. We first tested the new AAVs in a New World monkey, the marmoset, which has recently been gaining attention in the neuroscience community as a promising animal model for biomedical research (Marx, 2016; Miller et al., 2016; Jennings et al., 2016). Intravenous delivery of MaCPNS1 and MaCPNS2 to adult marmosets showed potent PNS tropism. However, the vectors also efficiently crossed the BBB to transduce the CNS, making them potent vectors across the nervous system. We further validated the vectors' tropism in an Old World monkey, the rhesus macaque, which is more closely related to humans and is widely used as an animal model for pre-clinical research, including gene therapy (Jennings et al., 2016; Hudry and Vandenberghe, 2019; Bey et al., 2020). As in marmosets, intravenously delivered MaCPNS1 and MaCPNS2 efficiently transduced both the PNS and CNS in an infant rhesus macaque. The enhanced CNS tropism we observed in NHPs may be explained by the heterogeneity of the BBB across species.

The conservation of these AAV variants' potent PNS tropism across species validates the usefulness of selecting capsids in mouse models, a preferred model among capsid engineers due to the relatively fewer challenges implementing iterations of *in vivo* selection or capsid evolution given animal availability. However, the question of translatability for CNS tropism requires further investigation. Prior CNS-specific selections have yielded capsids which may or may not be translatable across species (Matsuzaki et al., 2018; Goertsen et al., 2021) or whose potential has yet to be tested.

In summary, here we introduce new AAVs to address some significant challenges in the field of gene delivery vectors for the nervous system (Table S1). Non-invasive delivery of transgenes across the nervous system can be transformative for many applications, including basic science, as demonstrated with our previously-engineered AAV vectors (Chakrabarti et al., 2020; Marvaldi et al., 2020; Reynaud-Dulaurier and Decressac, 2020; Levy et al., 2020; Takano et al., 2020; Asencor et al., 2021; Duan et al., 2021; Monteys et al., 2021). With several therapeutic candidates now in the pipeline for various neurological disorders (Deverman et al., 2018; Hudry and Vandenberghe, 2019; Sevin and Deiva, 2021; Privolizzi et al., 2021), the new systemic AAV vectors described in this study, AAV-MaCPNS1 and AAV-MaCPNS2, offer hope to accelerate translational research as well.

2.10 FIGURES

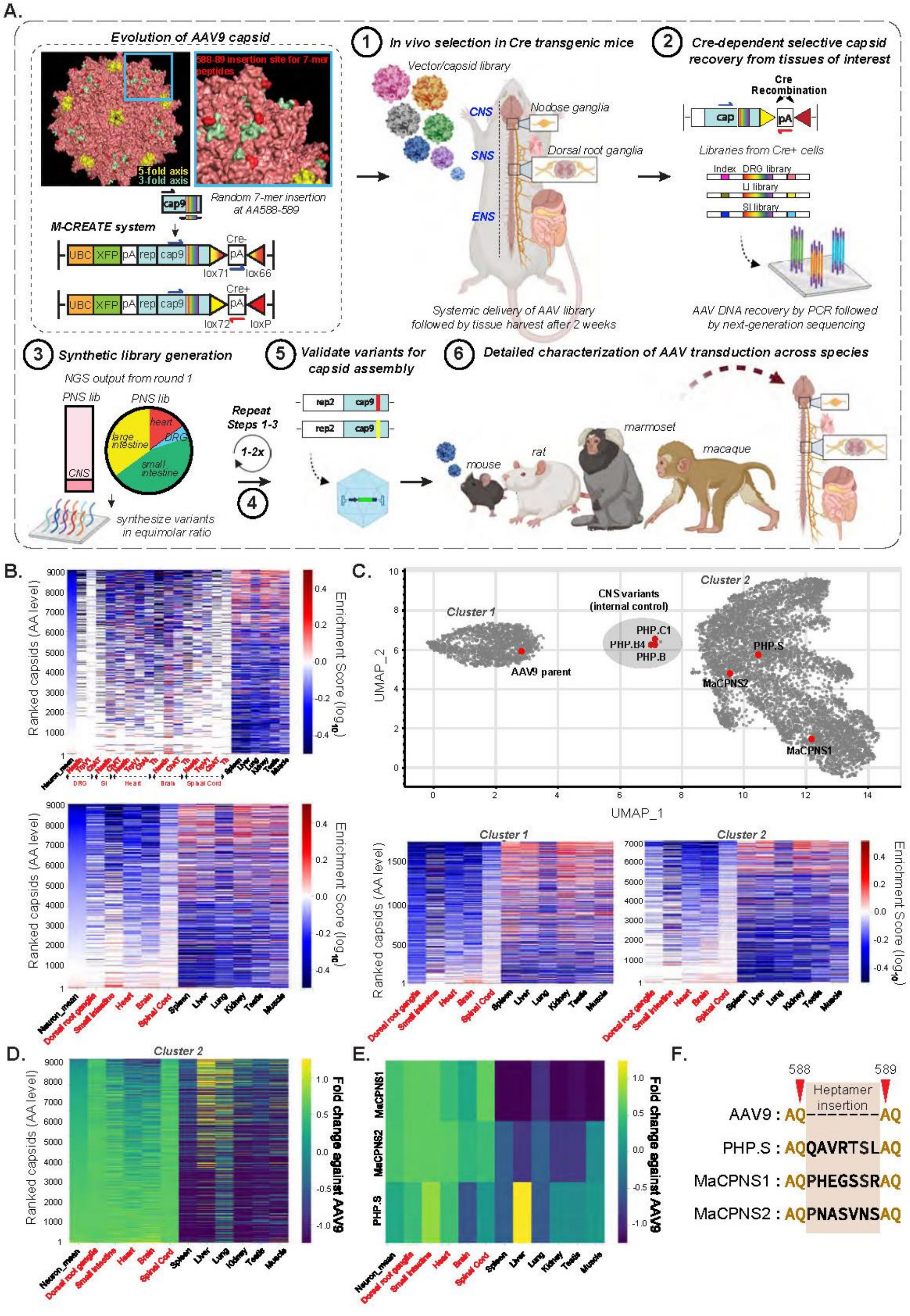
A.
Evolution of AAV9 capsid
588-89 insertion site for 7-mer peptides
5-fold axis
3-fold axis
cap9
Random 7-mer insertion at AA588-589
M-CREATE system
UBC XFP pA rep cap9
Cre-
pA
lox71 lox66
Cre+
lox72 loxP
1 In vivo selection in Cre transgenic mice
Vector/capsid library
CNS
SNS
ENS
Nodose ganglia
Dorsal root ganglia
Systemic delivery of AAV library followed by tissue harvest after 2 weeks
2 Cre-dependent selective capsid recovery from tissues of interest
Cre Recombination
cap
pA
Libraries from Cre+ cells
Index DRG library
LI library
SI library
AAV DNA recovery by PCR followed by next-generation sequencing
3 Synthetic library generation
NGS output from round 1
PNS lib
PNS lib
CNS
heart
DRG
large intestine
small intestine
synthesize variants in equimolar ratio
Repeat Steps 1-3
1-2x
4
5 Validate variants for capsid assembly
rep2 cap9
6 Detailed characterization of AAV transduction across species
mouse
rat
marmoset
macaque
B.
Ranked capsids (AA level)
Enrichment Score (log$_{10}$)
Neuron_mean
DRG
SI
Heart
Brain
Spinal Cord
Spleen
Liver
Lung
Kidney
Testis
Muscle
Dorsal root ganglia
Small intestine
C.
UMAP_2
UMAP_1
Cluster 1
Cluster 2
CNS variants (internal control)
PHP.C1
PHP.B4
PHP.B
AAV9 parent
PHP.S
MaCPNS2
MaCPNS1
D.
Cluster 2
Fold change against AAV9
E.
MaCPNS1
MaCPNS2
PHP.S
F.
588
589
Heptamer insertion
AAV9 : AQ-------AQ
PHP.S : AQQAVRTSLAQ
MaCPNS1 : AQPHEGSSRAQ
MaCPNS2 : AQPNASVNSAQ

Figure 1: Multiplexed-CREATE selection for AAV capsids targeting the nervous system across species.

A. An overview of the capsid selection method, Multiplexed-CREATE, and characterization of selected capsids across species. Top left panel illustrates evolution of the AAV9 capsid (PDB 3UX1) with a zoom-in (blue) of a three-fold axis and the *7-mer-i* library insertion site between residues 588-589 highlighted in red. The diagrams below demonstrate the arrangement of the acceptor vector in the absence (top) or presence (bottom) of Cre, with the corresponding orientations of the forward/reverse primers used for Cre+ selective recovery. The selection workflow involves four key steps: (1) generation of capsid library and intravenous (IV) delivery into transgenic mouse lines where Cre is restricted to cell types of interest (SNAP-Cre, GFAP-Cre, Tek-Cre, n=2 mice per Cre line). (2) Two weeks post-injection, viral DNA is recovered across cell-types/tissues using Cre-dependent PCR and Illumina next-generation sequencing (NGS), and (3) fed into synthetic pool library production. (4) This library then goes through a second round of *in vivo* selection. Following this selection process, identified variants are validated for (5) virus production and (6) *in vivo* transduction across species. **B.** Heatmaps of capsid variants' mean enrichment by Cre-dependent recovery across tissues of interest (red text) and Cre-independent recovery across off-targets (black text) after two rounds of selection. Cre lines are plotted separately (top panel, n=3 mice per organ) or grouped by organs (bottom panel). The y-axis represents capsids unique at the amino acid (AA) level, ranked by 'neuron mean', which is the mean of the enrichment of all targets of interest. **C.** UMAP cluster representation of ~9,000 variants that were recovered after two rounds of selection (UMAP parameters: n_neighbors=15, min_dist=0.1, n_components=2, random_state=42, metric='correlation', verbose=3). Three separable clusters are shown along with the positions of known capsids (AAV9, PHP.S, PHP.B, PHP.B4, PHP.C1) and new capsids (MaCPNS1 and MaCPNS2). Heatmaps (below) show enrichment of representative capsids from Clusters-1 and -2 across organs. **D.** Heatmap of enrichment fold changes against parental AAV9 across organs. **E.** Heatmap of enrichment fold changes against parental AAV9 of variants MaCPNS1 and MaCPNS2 and previously-engineered variant PHP.S across organs. **F.** Identity of hepta-AA peptides inserted between positions 588-589 of AAV9 for PHP.S, MaCPNS1 and MaCPNS2 capsids.

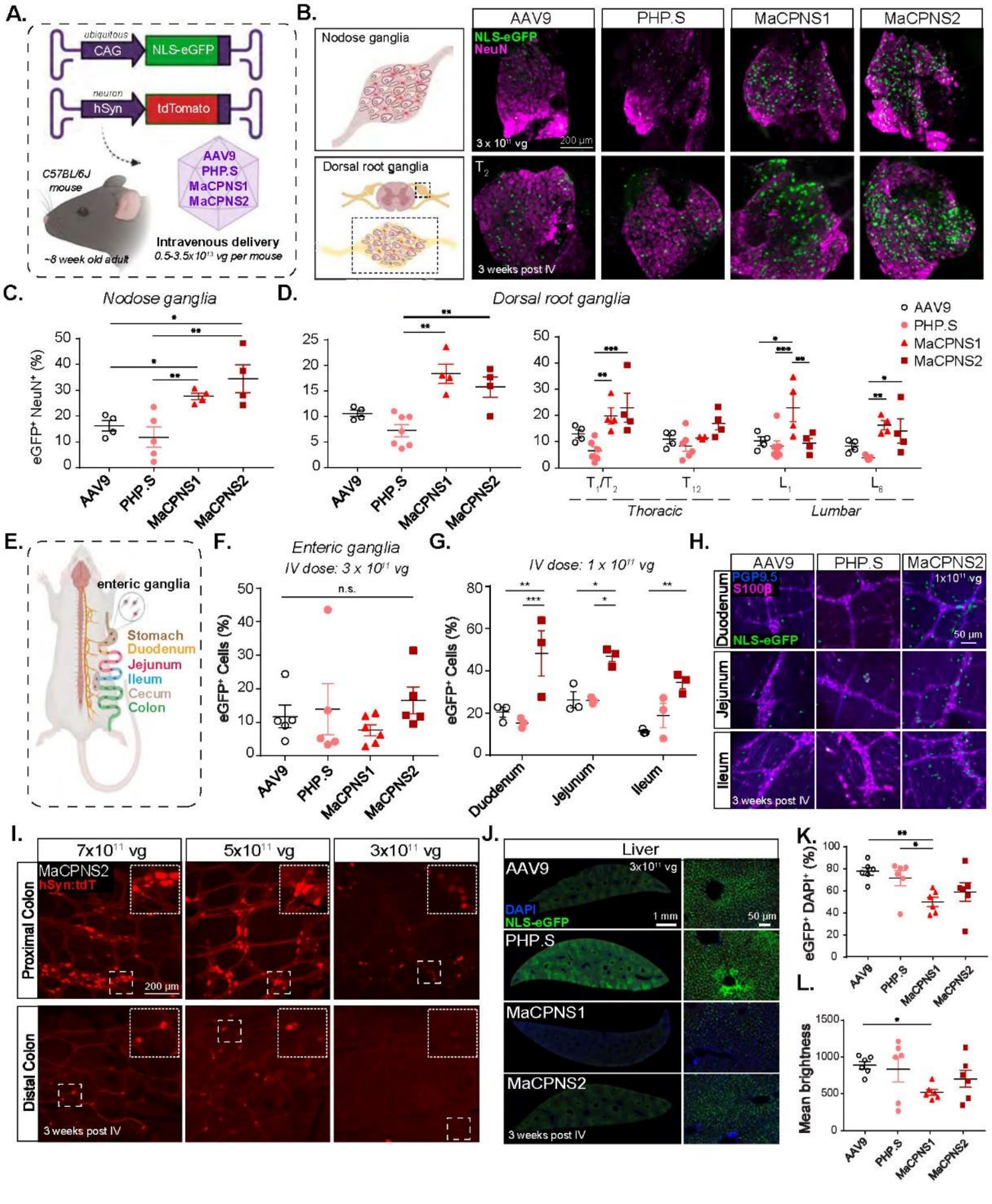

Figure 2: Engineered AAVs can efficiently target the peripheral nervous system in mice following systemic delivery.

A. Illustration demonstrating the IV administration of AAV capsids packaged with ssAAV:CAG-2xNLS-eGFP and ssAAV:hSyn-tdTomato genome in a mouse model (~8 week-old young C57BL/6J adults). **B.** (Top) An illustration of the nodose ganglia (NG) (left), and representative images of AAV9, PHP.S, MaCPNS1 and MaCPNS2 vector-mediated expression of nuclear-localized (NLS) eGFP (green) in NG (right). (Bottom) An illustration of the dorsal root ganglia (DRG) in the spinal cord (left) and (right) representative images of AAV vector-mediated expression of NLS-eGFP (green) in DRG across segment T2 (Thoracic) of the spinal cord (n≥4 per group, ~8 week-old C57BL/6J males, $3x10^{11}$ vg IV dose per mouse, 3 weeks of expression). Magenta: αNeuN antibody staining for neurons. Images are matched in fluorescence intensity to the respective AAV9 control. Scale bar: 200 µm. **C.** Percentage of AAV-mediated eGFP expression overlapping with the αNeuN marker in NG. One-way ANOVA non-parametric Kruskal-Wallis test (exact P=0.0003), and follow-up multiple comparisons with uncorrected Dunn's test are reported (P=0.0499 for AAV9 versus MaCPNS1, P=0.0251 for AAV9 versus MaCPNS2, P=0.0094 for PHP.S versus MaCPNS1, P=0.0038 for PHP.S versus MaCPNS2). $*P \leq 0.05$, $**P \leq 0.01$ are shown, $P > 0.05$ is not shown; n≥4 per group, same experimental parameters as **B.** Each data point represents 1-2 nodose ganglia per mouse comprising >700 cells, mean ± s.e.m is plotted. **D.** Percentage of eGFP expression overlapping with the αNeuN marker in DRG (left) where each data point shows the mean per mouse across select DRGs within thoracic and lumbar segments of the spinal cord. A one-way ANOVA, non-parametric Kruskal-Wallis test (exact P=0.0005), and follow-up multiple comparisons with uncorrected Dunn's test are reported (P=0.0018 for PHP.S versus MaCPNS1, P=0.0087 for PHP.S versus MaCPNS2). $*P \leq 0.05$, $**P \leq 0.01$ are shown, $P > 0.05$ is not shown; n≥4 per group, same experimental parameters as **B.** Each data point shows mean ± s.e.m of DRGs across different areas of each mouse, comprising a mean of 1-2 DRGs per area with >200 αNeuN+ cells per DRG. (Right) Percentage of eGFP expression overlapping with the αNeuN marker in DRG across spinal cord areas in individual mice. A two-way ANOVA and Tukey's multiple comparisons tests with adjusted P values are reported ($*P \leq 0.05$, $**P \leq 0.01$ and $***P \leq 0.001$ are shown, $P > 0.05$ is not shown). Each data point shows the mean ± s.e.m of 1-2 DRG per mouse comprising >200 αNeuN+ cells per DRG. **E.**

Illustration of the adult mouse gastrointestinal (GI) tract, highlighting the enteric ganglia (zoom-in) that are spread across the different segments of the GI tract. **F.** Percentage of cells expressing NLS-eGFP delivered by AAV vectors in the myenteric plexus across the GI tract: stomach, duodenum, jejunum, ileum, proximal colon and cecum (ssAAV:CAG-2xNLS-eGFP genome, n≥5 per group, ~8 weeks old C57BL/6J males, 3x10^{11} vg IV dose per mouse, 3 weeks of expression). A one-way ANOVA non-parametric Kruskal-Wallis test (approximate P=0.2985), and follow-up multiple comparisons using uncorrected Dunn's test are reported (individual P > 0.05, n.s.). Each data point shows the mean ± s.e.m of >100 enteric ganglia per intestinal segment per mouse). **G.** Percentage of cells expressing NLS-eGFP (green in **H**) in the myenteric plexus of small intestinal segments: duodenum, jejunum and ileum delivered by AAV vectors: AAV9, PHP.S and MaCPNS2 (ssAAV:CAG-2xNLS-eGFP genome, n=3 per group, 1x10^{11} vg IV dose per mouse, 3 weeks of expression). Two-way ANOVA, Tukey's multiple comparisons tests with adjusted P values are reported (*P ≤ 0.05, **P ≤ 0.01 and ***P ≤ 0.001 are shown, P > 0.05 is not shown). Each data point shows the mean ± s.e.m of ≥ 2 images per mouse comprising >100 enteric ganglia. **H.** shows representative images of AAV-mediated eGFP expression across the individual intestinal segments analyzed in **G.** Scale bar: 50 µm. The tissues were co-stained with αS100β (magenta) antibody for glia and αPGP9.5 (blue) for neurons. The images are matched in fluorescence intensity to the respective AAV9 control. **I.** MaCPNS2 vector-mediated expression of tdTomato (red) from ssAAV:hSyn-tdTomato in the proximal and distal segments of the colon at three different IV doses per mouse: 7x10^{11} vg, 5x10^{11} vg, 3x10^{11} vg (3 weeks of expression, n=3 per group, scale bar: 200 µm, dotted white box inset represents a zoomed-in view of the indicated area in each image). Images in the distal and proximal colon are matched in fluorescence intensity. **J.** Representative images of AAV vector-mediated expression of NLS-eGFP (green) from ssAAV:CAG-2xNLS-eGFP in the liver (n=6 per group, 3x10^{11} vg IV dose/mouse, 3 weeks of expression, blue: DAPI staining of nuclei, scale bar: 1 mm (left, full cross-sectional image), and 50 µm (right, higher magnification view). The images are matched in fluorescence intensity to the respective AAV9 control. **K.** Percentage of eGFP+ cells overlapping with the DAPI marker in the liver. A non-parametric Kruskal-Wallis test (approximate P=0.0168), and follow-up multiple comparisons with uncorrected Dunn's test (P=0.0035 for AAV9 versus MaCPNS1 and P=0.0189 for PHP.S versus MaCPNS1) are reported (*P ≤ 0.05, **P ≤ 0.01 are shown, P > 0.05 is not shown; same experimental parameters as **J.**, each data point shows the mean ± s.e.m of 4 images per mouse comprising >780 DAPI+ cells per image). **L.** Mean brightness of the eGFP+ cells quantified in **K.** A non-parametric Kruskal-Wallis test (approximate P=0.1698), and follow-up multiple comparisons with uncorrected Dunn's test (P=0.0433 for AAV9 versus MaCPNS1) is reported (*P ≤ 0.05 is shown, P > 0.05 is not shown; each data point shows the mean ± s.e.m of 4 images per mouse comprising >780 DAPI+ cells per image).

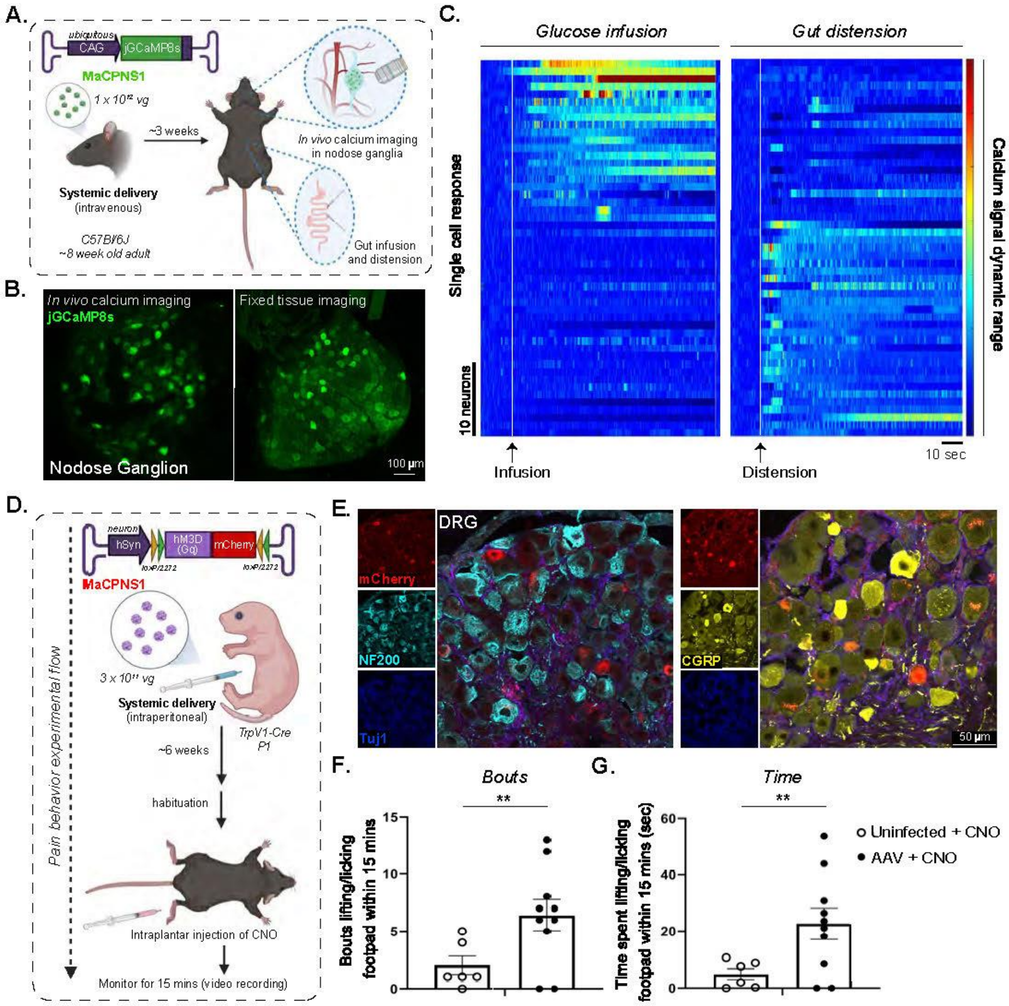

Figure 3: Systemic delivery of GCaMP sensor and excitatory DREADD actuator

using AAV-MaCPNS1 enable functional characterization of DRG neurons in mouse models.

A. Illustration of IV administration of MaCPNS1 capsid packaged with ssAAV:CAG-jGCaMP8s genome in mice (~8 week-old young adults, C57BL/6J males, $1x10^{12}$ vg IV dose/mouse, n=4). Three weeks post-expression, the mice were anesthetized and subjected to *in vivo* calcium imaging in nodose ganglia (NG, top zoom-in), and glucose infusion and distension in the gut (bottom zoom-in). **B.** Representative images of MaCPNS1 vector-mediated expression of jGCaMP8s (green) in NG *in vivo* (left), and in post-hoc fixed tissue (right) (scale bar: 100 µm). **C.** Single-cell activity response measured by calcium signal dynamics in the NG (data pooled from 4 experimental mice). Left panel: NG neuronal response to glucose infusion (white dotted line). Right panel: NG neuronal response to gut distension (white dotted line). **D.** Illustration of the pain induction experimental workflow. MaCPNS1 vector with ssAAV:hSyn-DIO-hM3D(Gq)-mCherry was intraperitoneally administered to a TrpV1-Cre mouse model (postnatal stage 1 (P1), males, $3x10^{11}$ vg IV dose/mouse). After six weeks of expression, the mice (AAV injected or untreated) were habituated and subjected to intraplantar injection with the agonist CNO, after which the mice were monitored for nocifensive lifting/licking behaviors. **E.** Representative images of DRG sections showing MaCPNS1 vector-mediated mCherry (red) expression. The tissues were co-stained with αNF200 (cyan), αTuj1 (blue) and αCGRP (yellow) markers. **F**. Total bouts of, and **G** total time spent lifting or licking the footpad within 15 minutes of injection in uninfected (n=6) and MaCPNS1-infected (n=10) mice treated with CNO. $^{**}P \leq 0.01$ by unpaired t-test. Mean+/- sem are shown.

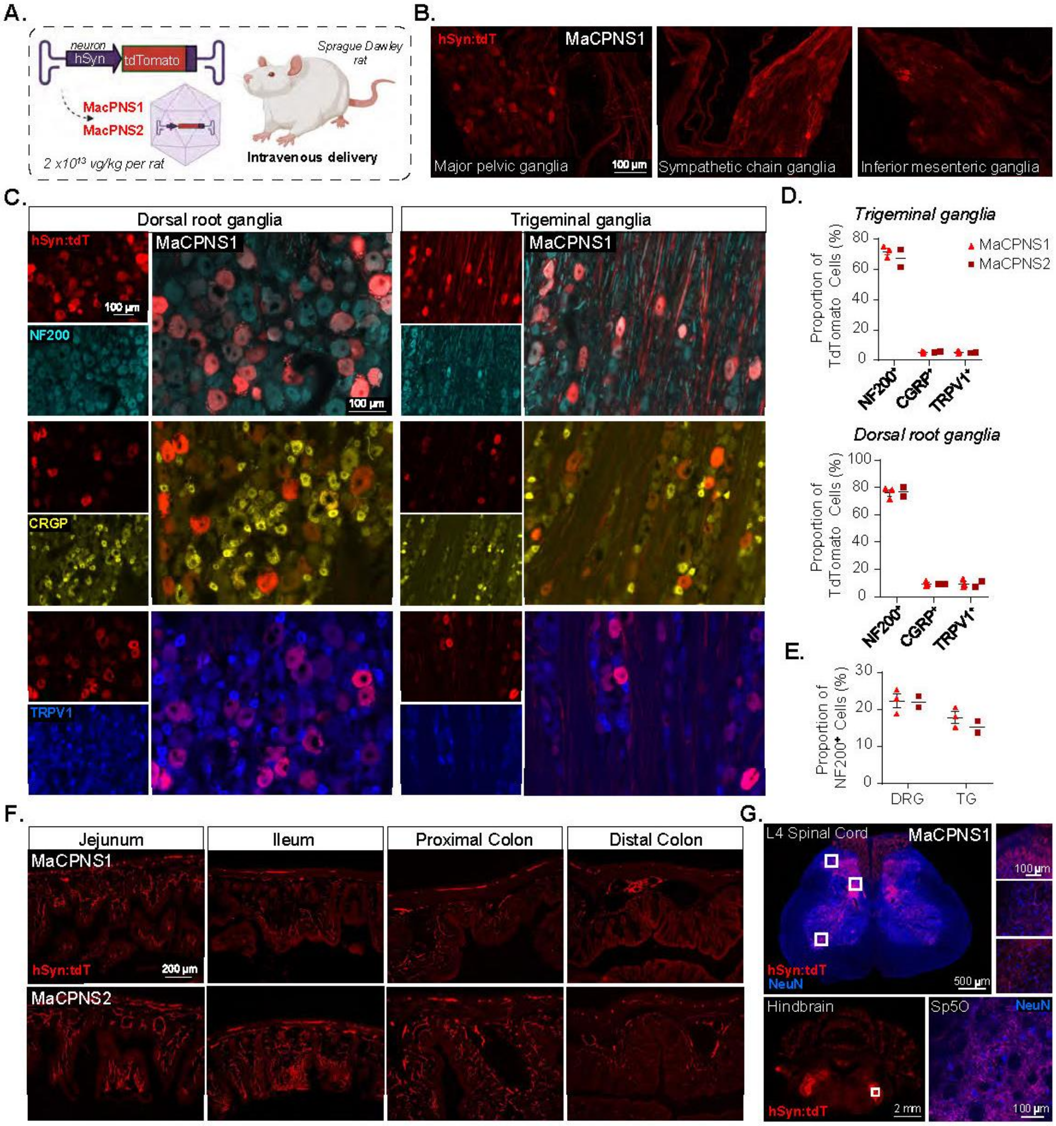

Figure 4: Engineered AAVs can efficiently target the peripheral nervous system in adult rats following systemic administration.

A. Illustration of IV administration of AAV capsids MaCPNS1 and MaCPNS2 packaged with ssAAV:hSyn-tdTomato genome in a rat model (young adults, Sprague Dawley, male, 2×10^{13} vg/kg per rat). The rat tissues were stained with αDsRed (red) antibody against tdTomato **B.** Representative images of MaCPNS1 vector-mediated tdTomato (red) expression in major pelvic ganglia (left), sympathetic chain ganglia (middle) and inferior mesenteric ganglia (right) in adult rats 3 weeks post expression (n≥2 per group, scale bar:

100 µm). **C.** Representative images of MaCPNS1 vector-mediated tdTomato (red) expression in DRG (left) and TG (right). The tissues were co-stained with either αNF200 (cyan), αCGRP (yellow), or αTRPV1 (blue) markers (scale bars: 100 µm). **D.** Quantification of proportion of AAV-mediated tdTomato expressing cells that overlap with αNF200, αCGRP and αTRPV1 markers in TG (above) and DRG (below), and **E.** proportion of αNF200 marker+ cells that overlap with the AAV-mediated tdTomato expressing cells in DRG and TG (n≥2 per group, each data point represents the average of at least 3 images from each rat, mean ± s.e.m is plotted for n>2, mean is plotted for n=2). **F.** Representative images of MaCPNS1 and MaCPNS2 vector-mediated tdTomato expression across different segments of the GI tract: jejunum, ileum, proximal colon and distal colon (scale bar: 200 µm). **G.** Representative images of MaCPNS1 vector-mediated tdTomato expression in the spinal cord (above, scale bar: 500 µm) with zoomed-in views of selected areas (white boxes, right, scale bar: 100 µm), and hindbrain (below, scale bar: 2 mm) with zoomed-in view of Sp5O region (scale bar: 100 µm). The tissues were co-stained with αNeuN (blue) antibodies.

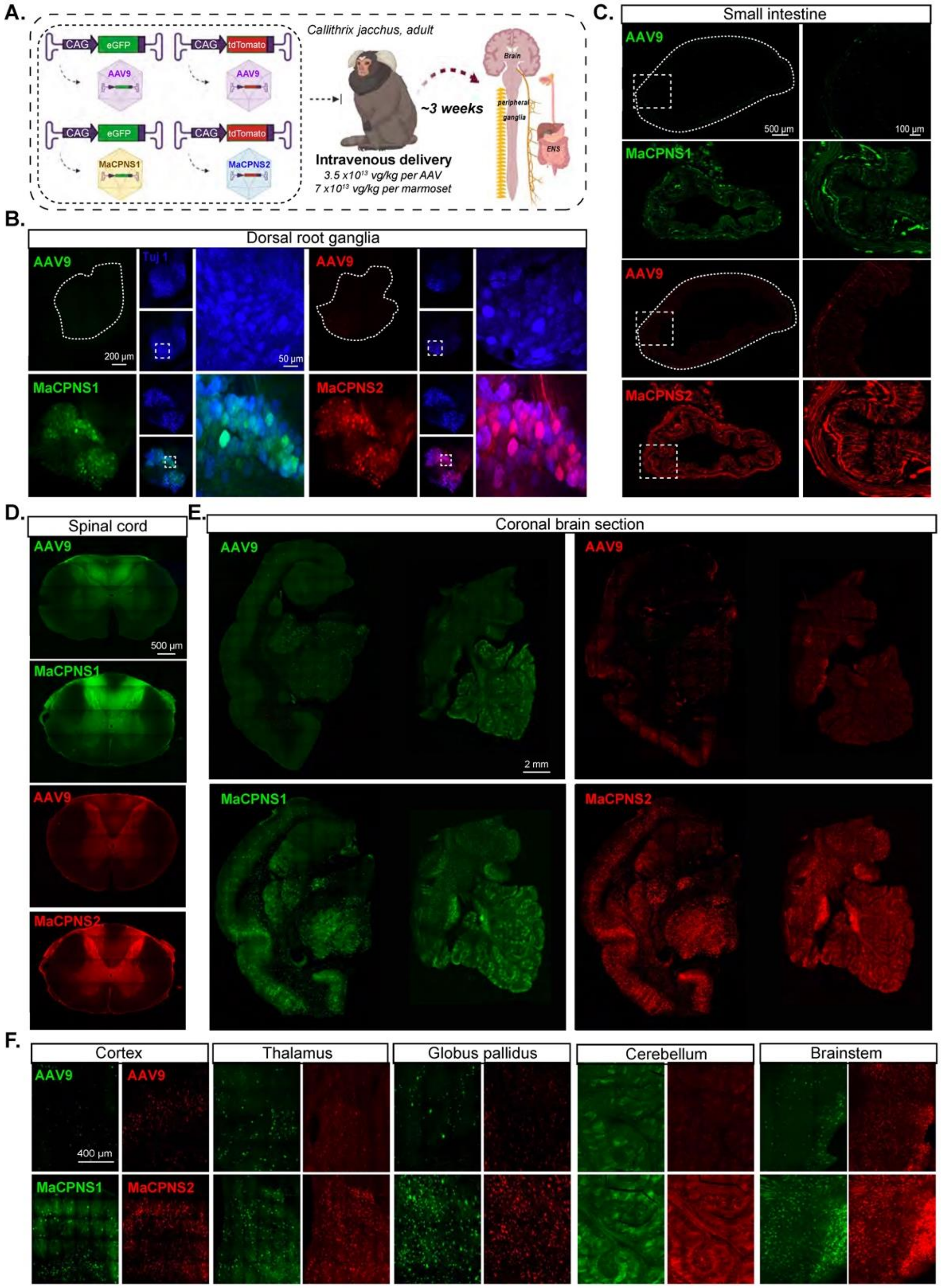

Figure 5: Engineered AAVs can efficiently transduce the central and peripheral nervous system in marmoset.

A. Illustration of AAV vector delivery to adult marmoset to study transduction across the CNS and PNS after 3 weeks of expression. The capsids (AAV9/MaCPNS1/MaCPNS2) and their corresponding genomes (ssAAV:CAG-eGFP/tdTomato) are shown on the left. Two AAV vectors packaged with colored fluorescent reporters were mixed and intravenously delivered at a total dose of $7x10^{13}$ vg/kg per adult marmoset (16 month old *Callithrix jacchus*, i.e. $3.5x10^{13}$ vg/kg per AAV). Representative images of marmoset **B.**, DRGs (scale bar: 200 µm, left and 500 µm, right), **C.**, small intestine (scale bar: 500 µm, left and 100 µm, right), **D.**, fibers in the dorsal column of the spinal cord (scale bar: 500 µm), **E.**, coronal brain sections of midbrain (left) and hindbrain (right) (scale bar: 500 µm), and **F.**, select brain areas: cortex, thalamus, globus pallidus, cerebellum and brainstem (scale bar: 400 µm), showing AAV9 vector-mediated expression of eGFP (green) or tdTomato (red), MaCPNS1-mediated expression of eGFP (green) and MaCPNS2-mediated expression of tdTomato (red). The images are matched in fluorescence intensity to the respective AAV9 control. Zoomed-in views of selected areas (dotted white boxes) are shown on the right in **B.** and **C**. In **B.** the zoomed-in view shows the overlap of MaCPNS1 and MaCPNS2-mediated expression with the neuronal marker Tuj1 (blue).

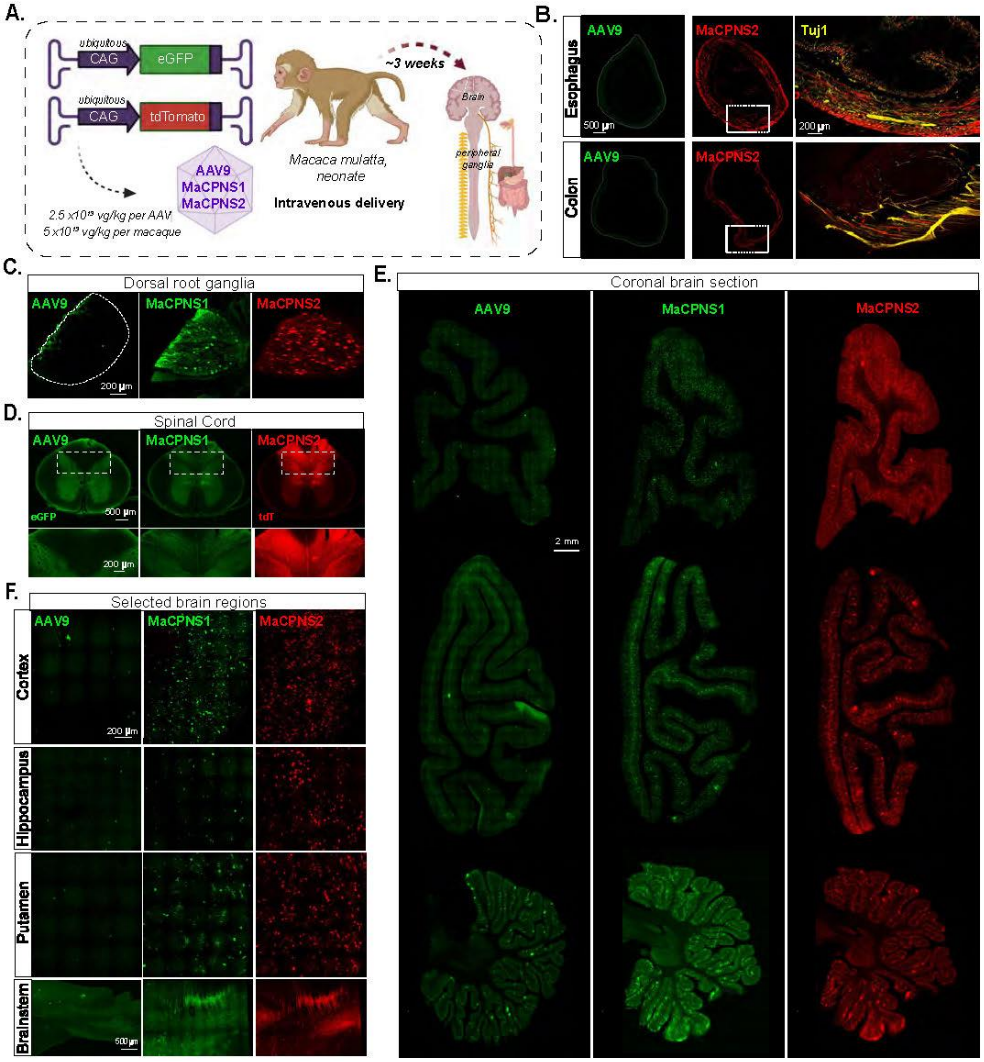

Figure 6: Engineered variants efficiently target the central and peripheral nervous system in macaque following systemic delivery.

A. Illustration of AAV vector delivery to macaque to study transduction across the CNS and PNS after 4 weeks of expression. The capsids (AAV9/MaCPNS1/MaCPNS2) and their corresponding genomes (ssAAV:CAG-eGFP/tdTomato) are shown on the left. Two AAVs packaged with different fluorescent proteins were mixed and intravenously injected at a dose of 5x10^{13} vg/kg per macaque (*Macaca mulatta*, injected within 10 days of birth, female, i.e. 2.5x10^{13} vg/kg per AAV). Representative images of macaque **B.**, GI regions of esophagus (top panel) and colon (bottom panel) (scale bar: 500 µm, left and 200 µm, right),

C., DRGs (scale bar: 200 µm), **D.**, spinal cord (scale bar: 500 µm, top and 200 µm, bottom), **E.**, coronal sections of forebrain, hindbrain and cerebellum (scale bar: 2 mm), and **F.**, selected brain areas: cortex, hippocampus, putamen, and brainstem (scale bar: 200 µm, top and 500 µm, bottom), showing AAV9 vector-mediated expression of eGFP (green), MaCPNS1-mediated expression of eGFP (green) and MaCPNS2-mediated expression of tdTomato (red). The eGFP images of MaCPNS1 are matched in fluorescence intensity to the AAV9 control. The zoomed-in views in **B** (right panels) show the overlap of MaCPNS2-mediated expression of tdTomato (red) with the neuronal marker Tuj1 (yellow). The zoomed-in views in **D** (bottom panels) show AAV-mediated expression of eGFP (green) and tdTomato (red) in the fibers in the dorsal column (white dashed boxes).

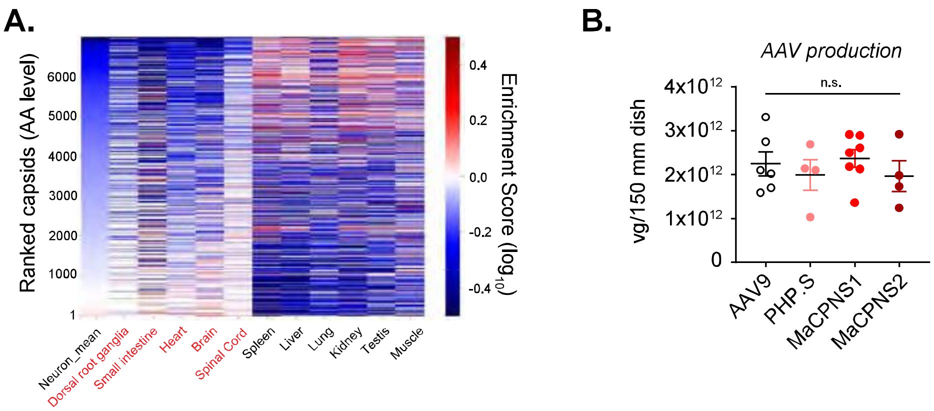

Supplementary Figure 1: AAV capsid library outcome post round-2 *in vivo* selection. Related to Figure 1.

A. Heatmap of 6300 capsid variants which showed a bias towards one or more of the neuronal tissues. Heatmap shows mean enrichment by Cre-dependent recovery across tissues of interest (red text) and Cre-independent recovery across off-targets (black text) after two rounds of selection. Cre lines are grouped by organs. The y-axis represents capsids unique at the amino acid (AA) level, ranked by ‘neuron mean’, which is the mean of the enrichment of all targets of interest. **B.** AAV vector yields from an established laboratory protocol (see Methods). One-way analysis of variance (ANOVA) non-parametric Kruskal-Wallis test (approximate P=0.6407, n.s.), and follow-up multiple comparisons with uncorrected Dunn’s test are reported (individual $P > 0.05$, n.s.; $n \geq 4$ per group, each data point is the mean of 3 technical replicates, mean ± s.e.m is plotted).

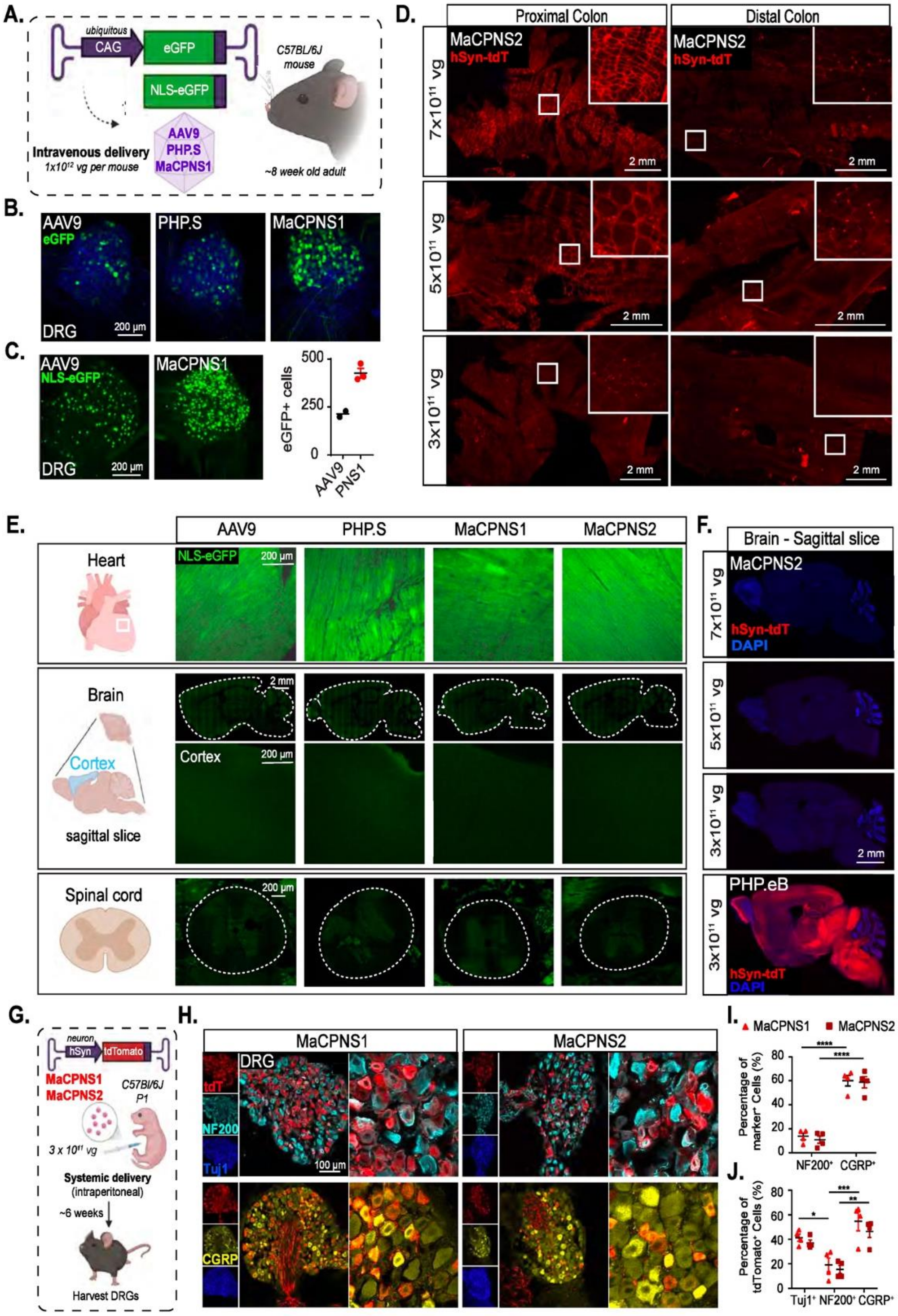

Supplementary Figure 2: Characterization of AAV variants across different organs in mice following systemic delivery. Related to Figure 2.

A. Illustration of IV administration of AAV9/PHP.S/MaCPNS1 capsid packaged with either ssAAV:CAG-eGFP or ssAAV:CAG-NLS-eGFP genome in mice (~8 weeks old, C57BL/6J males) at 1×10^{12} vg dose/mouse. **B**. Vector (AAV9/PHP.S/MaCPNS1)-mediated expression of eGFP (green) in DRG after 3 weeks of expression *in vivo* (n=3 per group). **C.** Vector-mediated expression of NLS-eGFP (green) in DRG after 3 weeks of expression, with imaging parameters matched across samples. Quantification of eGFP+ cells in DRG is shown at right (n=2-3 per group, mean ± s.e.m is plotted for n>2, mean is plotted for n=2). **D.** MaCPNS2 vector-mediated expression of tdTomato (red) from ssAAV:hSyn-tdTomato in the proximal and distal segments of the colon at three different IV doses per mouse: 7×10^{11} vg, 5×10^{11} vg, 3×10^{11} vg (3 weeks of expression, n=3 per group, white boxes show zoomed-in views of selected areas). **E.** Vector (AAV9, PHP.S, MaCPNS1 and MaCPNS2)-mediated expression of NLS-eGFP (green) in organs after 3 weeks of expression. Top panels show expression in heart. Middle panels show expression in the brain with zoomed-in views of the cortex. Bottom panels show expression in the spinal cord. **F.** MaCPNS2 vector-mediated expression of tdTomato (red) from ssAAV:hSyn-tdTomato in the brain at three different IV doses per mouse: 7×10^{11} vg, 5×10^{11} vg, 3×10^{11} vg (3 weeks of expression, n=3 per group). Bottom panel shows PHP.eB vector-mediated expression of tdTomato (red) using ssAAV:hSyn-tdTomato in the brain at an IV dose per mouse of 3×10^{11} vg (3 weeks of expression, n=3 per group). The tissues were co-stained with the nuclear stain DAPI (blue). Imaging parameters in **B-F** were matched across samples to the respective control in the experiment or the area. **G.** Illustration of intraperitoneal administration of MaCPNS1 vector packaged with ssAAV:hSyn-tdTomato in a C57BL/6J mouse model (postnatal stage 1 (P1), males, 3×10^{11} vg IV dose/mouse). After six weeks of expression, the DRG were harvested. **H.** Representative images of DRG sections showing MaCPNS1 vector-mediated tdTomato (red) expression. The tissues were co-stained with αNF200 (cyan), αTuj1 (blue) and αCGRP (yellow) markers. **I.** Quantification of the proportion of αNF200 and αCGRP marker+ cells that overlap with the AAV-mediated tdTomato-expressing cells in DRG, and **J.** proportion of AAV-mediated tdTomato-expressing cells that overlap with αTuj1, αNF200 and αCGRP markers in DRG (n=4 per group, unpaired t-test. Mean+/- sem are shown.)

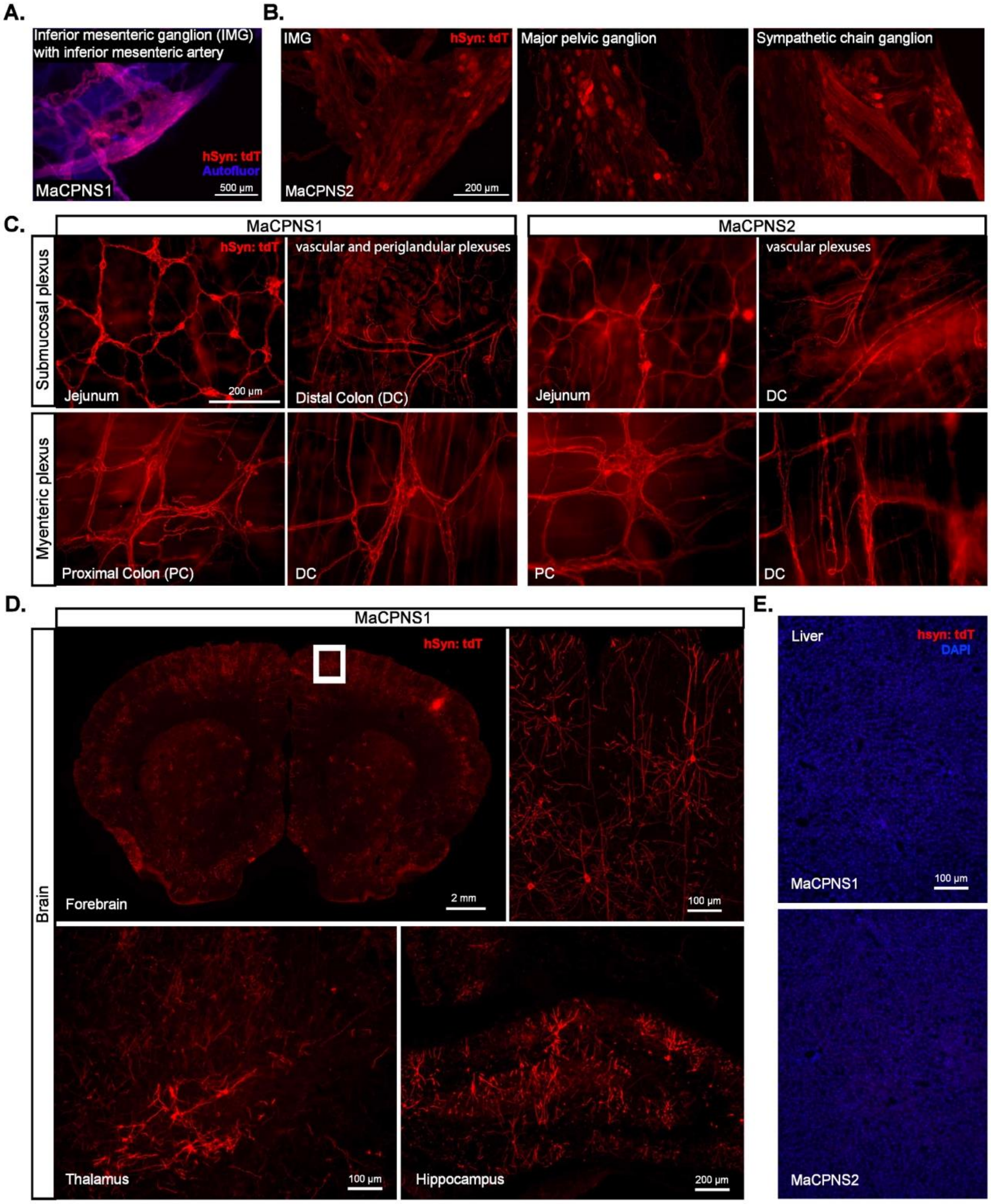

Supplementary Figure 3. Novel variants transduce peripheral ganglia and CNS in rats. Related to Figure 3.

AAV capsids (MaCPNS1 and MaCPNS2 packaged with ssAAV:hSyn-tdTomato genome) were intravenously administered in a rat model (young adults, Sprague Dawley, male, $2\mathrm{x}10^{13}$ vg/kg per rat). The tissues were stained with αDsRed (red) antibody against tdTomato.**A.** Representative image of MaCPNS1 vector-mediated tdTomato (red) expression in inferior mesenteric ganglion with inferior mesenteric artery (scale bar: 500 µm). **B**. Representative images of MaCPNS2 vector-mediated tdTomato (red) expression in major pelvic ganglia (left), sympathetic chain ganglia (middle) and inferior mesenteric ganglia (right) in adult rats after 3 weeks of expression (n≥2 per group, scale bar: 200 µm). **C.** Representative images of MaCPNS1 (left) and MaCPNS2 (right) vector-mediated tdTomato expression in the jejunum and distal colon at the submucosal plexus layer (top) and proximal colon and distal colon at the myenteric plexus layer (bottom). (scale bar: 200 µm). **D.** Representative images of MaCPNS1 vector-mediated tdTomato expression in the brain including forebrain (top left, scale bar: 2mm) with zoomed-in view of the cortex (white box, scale bar: 100 µm), thalamus (bottom left, scale bar: 100 µm) and hippocampus (bottom right, scale bar: 200 µm). **E.** Representative images of MaCPNS1 and MaCPNS2 vector-mediated tdTomato expression in the liver. The tissues were co-stained with DAPI (blue) (scale bar: 100 µm).

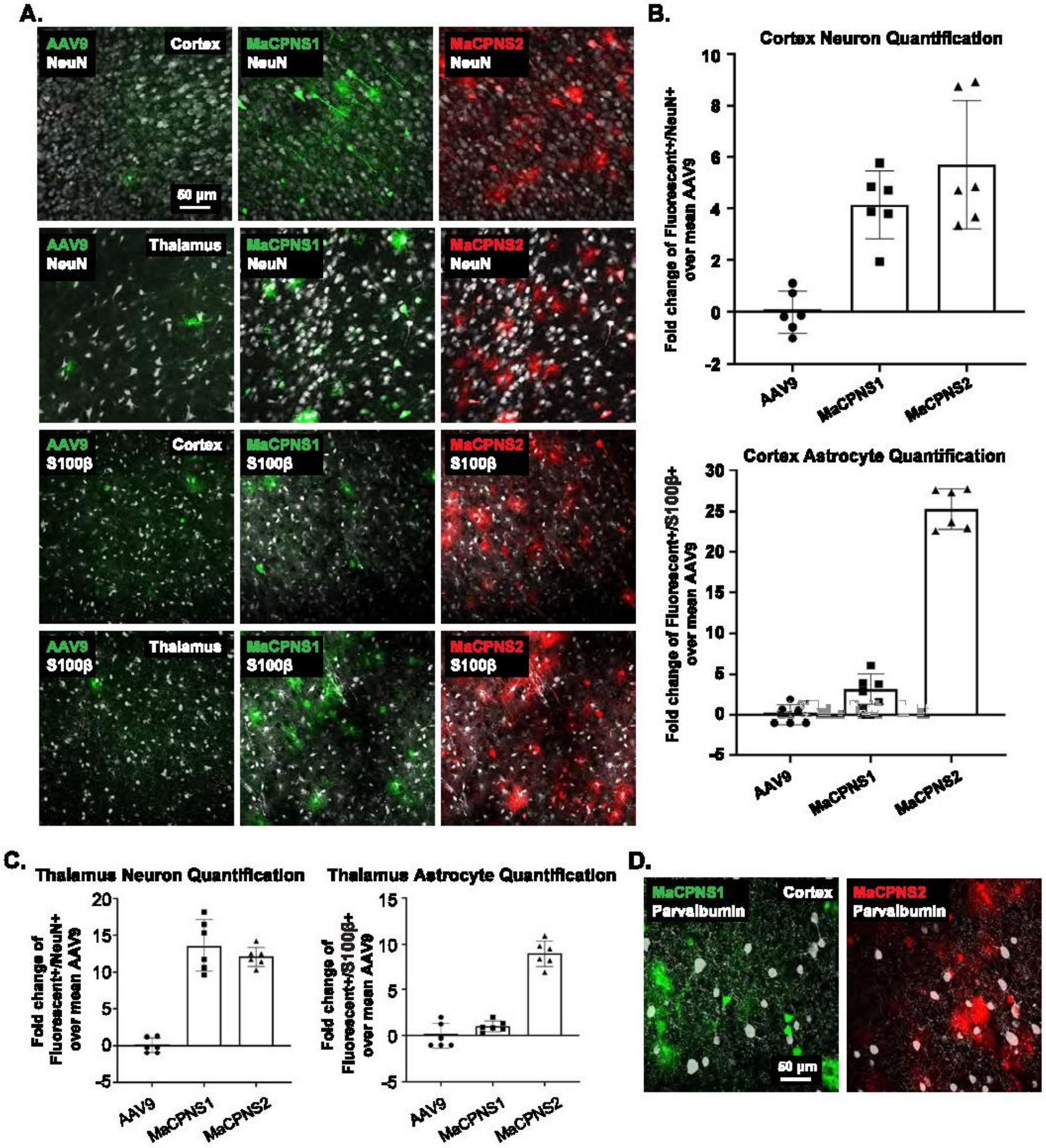

Supplementary Figure 4. Cell-type profiles of engineered AAVs in marmoset brain. Related to Figure 5.

A. Representative images of AAV9, MaCPNS1 and MaCPNS2 vector-mediated fluorescent protein expression in the marmoset cortex and thalamus (scale bar: 50 µm). Slices were co-stained with NeuN (top 2 rows, white) or S100β (bottom 2 rows, white). **B,**

C. Quantification of the fold change of Fluorescent+/marker over mean AAV9 in cortex and thalamus. Each data point is a slice. **D.** Representative images of MaCPNS1 and MaCPNS2 vector-mediated fluorescent protein expression in the marmoset cortex (scale bar: 50 µm). Slices were co-stained with Parvalbumin (white).

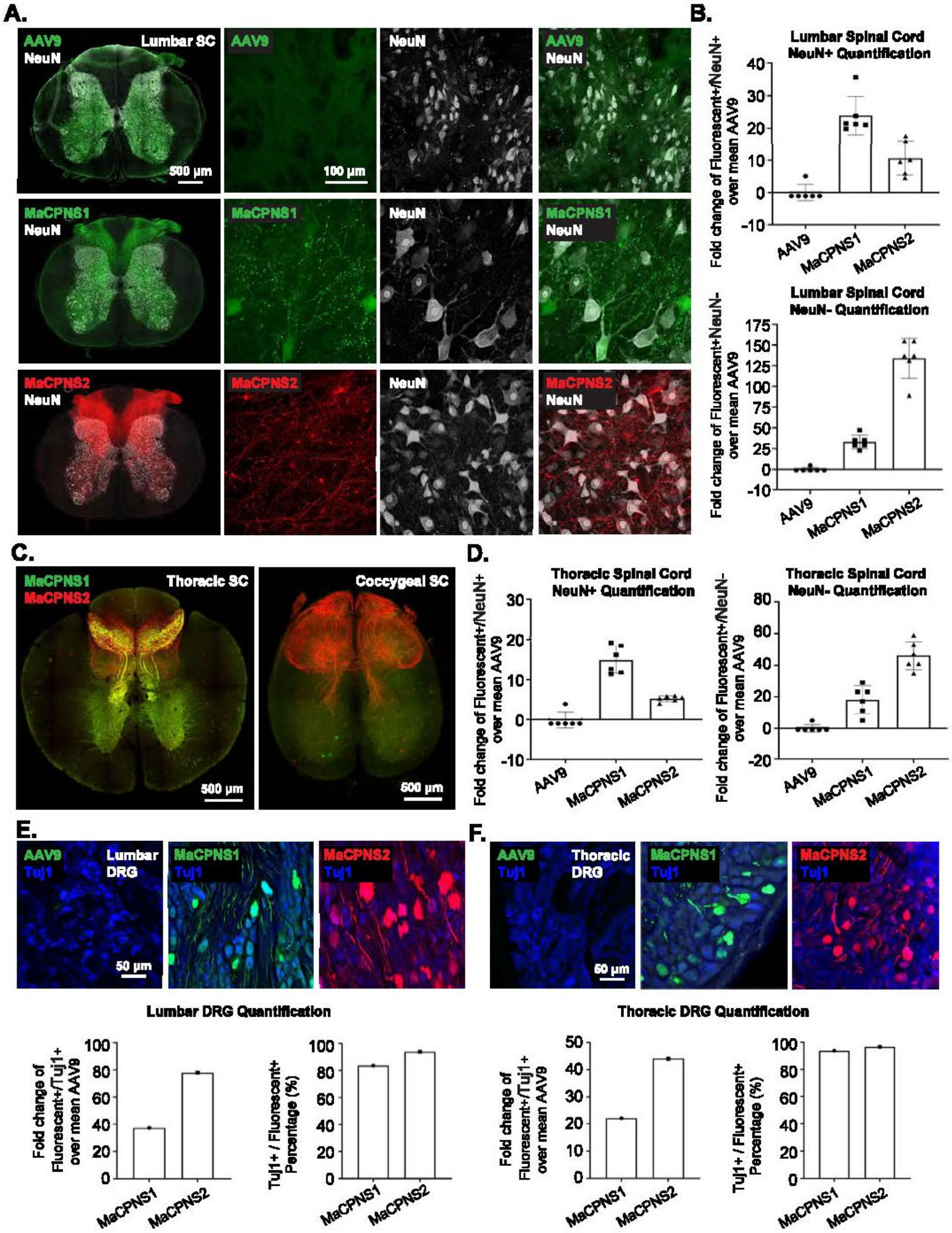

Supplementary Figure 5. Engineered vectors transduce spinal cord and DRG in macaque efficiently. Related to Figure 6.

A. Representative images of AAV9, MaCPNS1 and MaCPNS2 vector-mediated fluorescent protein expression in the macaque lumbar spinal cord (scale bar: 500 µm) with zoomed-in views of each channel (scale bar: 100 µm). Slices were co-stained with NeuN (white). **B.** Quantification of the fold change of Fluorescent+/marker over mean AAV9 in lumbar spinal cord. Each data point is a slice. **C.** Representative images of MaCPNS1 and MaCPNS2 vector-mediated fluorescent protein expression in the macaque thoracic spinal cord and coccygeal spinal cord (scale bar: 500 µm). **D.** Quantification of the fold change of Fluorescent+/marker over mean AAV9 in thoracic spinal cord. Each data point is a slice. **E, F.** (Top Panel) Representative images of AAV9, MaCPNS1 and MaCPNS2 vector-mediated fluorescent protein expression in the macaque lumbar DRG and thoracic DRG (scale bars: 50 µm). Slices were co-stained with Tuj1 (blue). (Bottom Panel) Quantification of the fold change of Fluorescent+/marker over mean AAV9 in DRGs and percentage of Tuj1+ within the fluorescent+ population. Each data point is a slice.

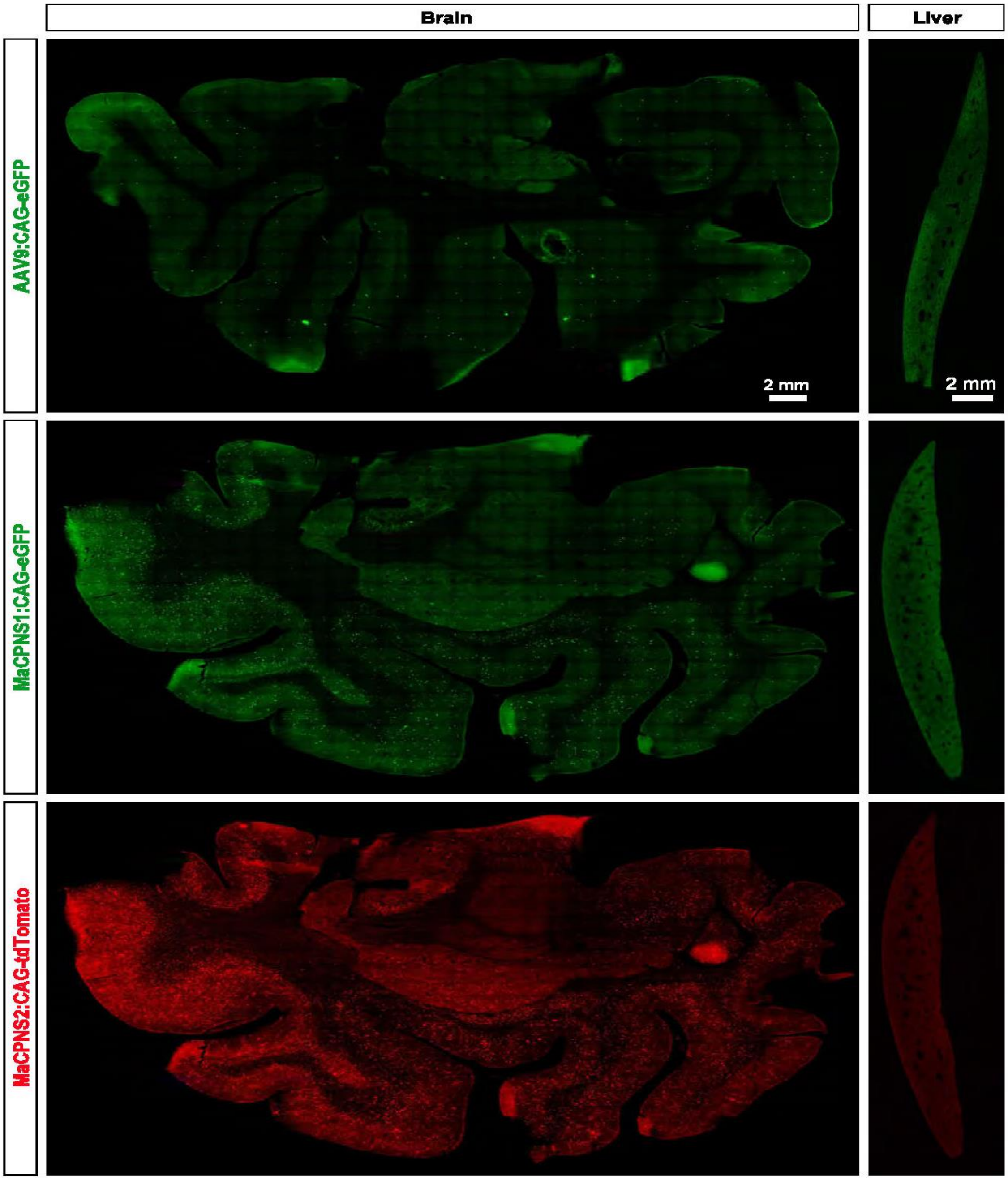

Supplementary Figure 6. Novel variants efficiently transduce macaque CNS while maintaining similar transduction in liver compared to AAV9. Related to Figure 6.

AAV capsids (AAV9/MaCPNS1/MaCPNS2) and their corresponding genomes (ssAAV:CAG-eGFP/tdTomato) were delivered to macaque to study transduction across the CNS and PNS after 3 weeks of expression. Two AAVs packaged with different fluorescent proteins were mixed and intravenously injected at a dose of $5x10^{13}$ vg/kg per macaque (*Macaca mulatta*, female, injected within 10 days of birth, $2.5x10^{13}$ vg/kg per AAV). Representative images of the brain (left) and liver (right) are shown (scale bars: 2 mm).

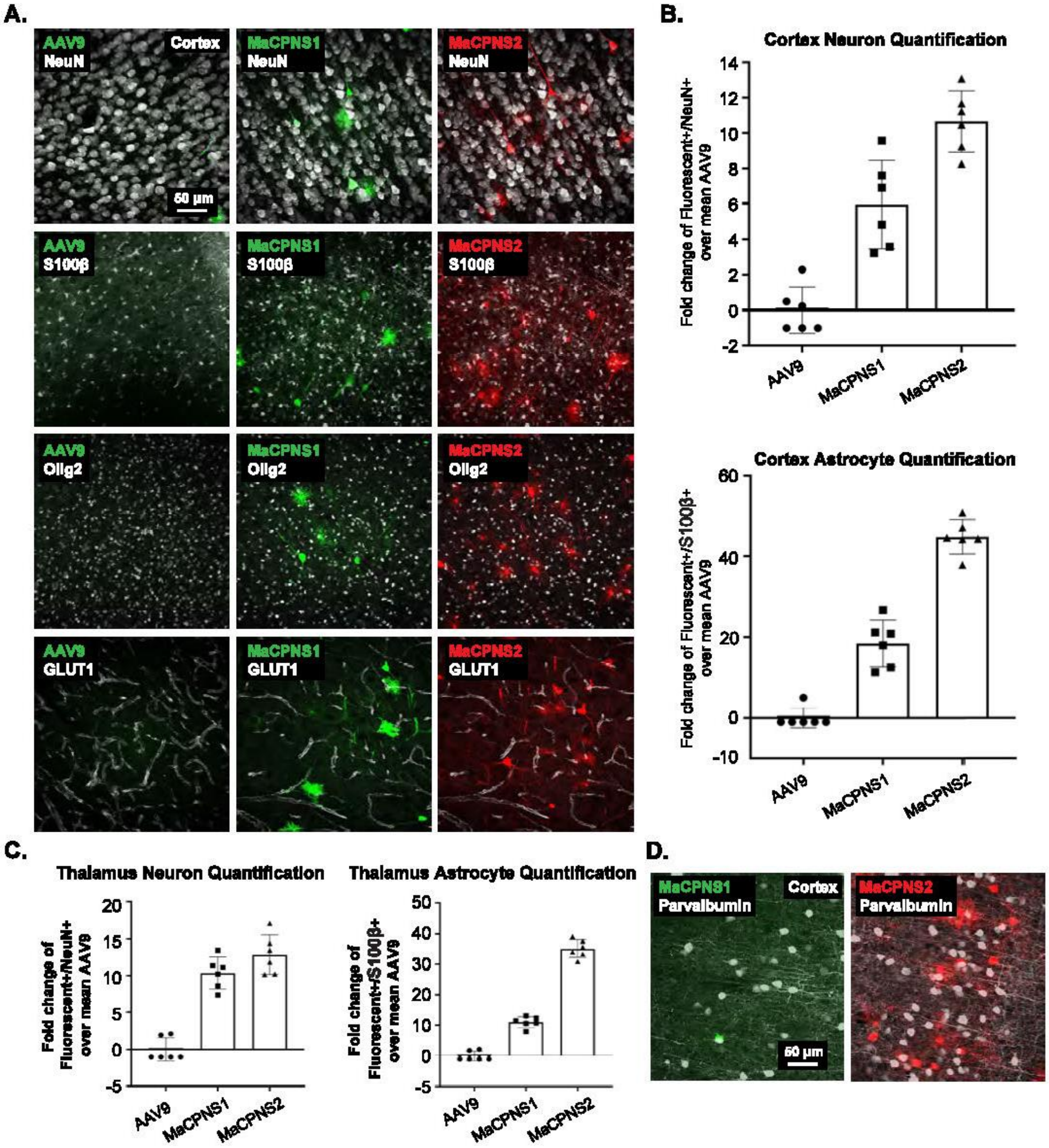

Supplementary Figure 7. Cell-type profiles of engineered AAVs in macaque brain. Related to Figure 6.

A. Representative images of AAV9, MaCPNS1 and MaCPNS2 vector-mediated fluorescent protein expression in the macaque cortex and thalamus (scale bar: 50 µm). Slices were co-stained with NeuN (first row, white), S100β (second row), Olig2 (third row) or GLUT1 (fourth row). **B, C.** Quantification of the fold change of Fluorescent+/marker over mean AAV9 in cortex and thalamus. Each data point is a slice. **D.** Representative images of MaCPNS1 and MaCPNS2 vector-mediated fluorescent protein expression in the macaque cortex (scale bar: 50 µm). Slices were co-stained with Parvalbumin (white).

	Mouse	Rat	Marmoset	Macaque
MaCPNS1	• efficient transduction of sensory ganglia (NG/DRG) • demonstrated functional readout and modulation of sensory ganglia	• transduction of sensory ganglia (DRG/TG), sympathetic chain ganglia, mixed sympathetic-parasympathetic ganglia and enteric ganglia across SI and LI • transduction of sensory nerve fibers entering SC and ascending afferent tracts in dorsal column • observed labeling of neurons across brain	• enhanced transduction of DRG, SI and ascending fiber tracts in dorsal column of the SC • robust transduction of neurons and astrocytes • more biased to neurons in the brain	• enhanced transduction of DRG • transduction of sensory nerve fibers entering SC and ascending afferent tracts in dorsal column • robust transduction of neurons and non-neuronal cells in brain and SC • more biased to neurons
MaCPNS2	• efficient transduction of sensory ganglia (NG/DRG) • efficient transduction of ENS, especially SI	• transduction of sensory ganglia (DRG/TG), sympathetic chain ganglia, mixed sympathetic-parasympathetic ganglia and enteric ganglia across SI and LI • transduction of sensory nerve fibers entering SC and ascending afferent tracts in dorsal column • observed labeling of neurons across brain	• enhanced transduction of DRG, SI and ascending fiber tracts in dorsal column of the SC • robust transduction of neurons and astrocytes in the brain	• enhanced transduction of DRG and GI tract, including esophagus, colon and SI • transduction of sensory nerve fibers entering SC and ascending afferent tracts in dorsal column • robust transduction of neurons and non-neuronal cells in brain and SC

NG: nodose ganglia; DRG: dorsal root ganglia; SI: small intestine; LI: large intestine; SC: spinal cord.

Table S1. Main features of novel AAVs across species following systemic delivery, related to Figure 6.

Video S1. Marmoset brain injected with MaCPNS1 and MaCPNS2, related to Figure 5.

MaCPNS1 packaging ssAAV:CAG-eGFP and MaCPNS2 packaging ssAAV:CAG-tdTomato were mixed and intravenously delivered at a total dose of 7x1013 vg/kg per adult marmoset (16-month-old Callithrix jacchus, i.e. 3.5x1013 vg/kg per AAV). Representative overview of marmoset midbrain.

Videos S2. Macaque midbrain injected with MaCPNS1 and MaCPNS2, related to Figure 6.

MaCPNS1 packaging ssAAV:CAG-eGFP and MaCPNS2 packaging ssAAV:CAG-tdTomato were mixed and intravenously injected at a dose of 5x1013 vg/kg per macaque (Macaca mulatta, injected within 10 days of birth, female, i.e., 2.5x1013 vg/kg per AAV). Representative overview of macaque midbrain.

Videos S3. Macaque hindbrain injected with MaCPNS1 and MaCPNS2, related to Figure 6.

MaCPNS1 packaging ssAAV:CAG-eGFP and MaCPNS2 packaging ssAAV:CAG-tdTomato were mixed and intravenously injected at a dose of 5x1013 vg/kg per macaque (Macaca mulatta, injected within 10 days of birth, female, i.e. 2.5x1013 vg/kg per AAV). Representative overview of macaque hindbrain.

Videos S4. Macaque cerebellum injected with MaCPNS1 and MaCPNS2, related to Figure 6.

MaCPNS1 packaging ssAAV:CAG-eGFP and MaCPNS2 packaging ssAAV:CAG-tdTomato were mixed and intravenously injected at a dose of 5x1013 vg/kg per macaque (Macaca mulatta, injected within 10 days of birth, female, i.e. 2.5x1013 vg/kg per AAV). Representative overview of macaque cerebellum.

2.11 MATERIALS AND METHODS

Experimental model and subject details

All animal procedures in mice that were carried out in this study were approved by the California Institute of Technology Institutional Animal Care and Use Committee (IACUC), and Harvard Medical School Institutional Animal Care and Use Committee (IACUC). C57BL/6J (000664), Tek-Cre (008863) (Kisanuki et al. 2001), ChAT-IRES-Cre (006410) (Rossi et al. 2011), Nestin-Cre (003771) (Giusti et al. 2014), and TRPV1-Cre (017769) (Cavanaugh et al. 2011) mice were purchased from the Jackson Laboratory (JAX). TH-Cre mice were obtained from the European Mouse Mutant Archive (EM::00254) and crossed with wild-type C57BL/6N mice. Heterozygous TH-Cre mice were used. For capsid selection experiments, 6-8 week old male and female mice were used. For *in vivo* validation studies of AAV capsid variants, 6-8 weeks old male mice were used.

All procedures performed on rats in this study were approved by the Animal Ethics Committee of the University of Melbourne (Ethics Number 1814639) and complied with the Australian Code for the Care and Use of Animals for Scientific Purposes (National Health and Medical Research Council of Australia). Six male Sprague-Dawley rats (Biomedical Sciences Animal Facility, University of Melbourne) aged 7 weeks were used in this study. Rats were housed in groups of 3 with environmental enrichment under a 12-hour (h) light-dark cycle with ad libitum access to food and water. Six male animals were used in this study and received tail vein injections of AAVs.

All experimental procedures performed on marmosets were approved by the University of California, San Diego, Institutional Animal Care and Use Committee (IACUC) and in accordance with National Institutes of Health and the American Veterinary Medical Association guidelines. 2 female animals and 1 male animal were used in this study and received intravenous injections of AAVs.

All experimental procedures performed on rhesus macaques were approved by the Institutional Animal Care and Use Committee at the University of California, Davis and the California National Primate Research Center (CNPRC). Two infant female animals were used in this study and received intravenous injections of AAVs.

For all the experiments performed in this study, the animals were randomly assigned, and the experimenters were not blinded while performing the experiments in this study unless indicated otherwise.

Method details

Library plasmid preparation

The plasmids used for AAV library preparation were described previously (Ravindra Kumar et al, 2020, Deverman et al, 2016) (plasmids available from Caltech CLOVER Center upon request). Briefly, plasmid rAAV-ΔCap-in-cis-Lox2 (Fig. 1A) was used for building the heptamer insertion (*7-mer-i*) AAV library. Plasmid pCRII-9Cap-XE was used as a PCR template for the DNA library generation. Plasmid AAV2/9-REP-AAP-ΔCap was used to supplement the AAV library during virus production.

Plasmid preparation for capsid characterization

The AAV capsid variants such as AAV-MaCPNS1 (Addgene plasmid # 185136) and AAV-MaCPNS2 (Addgene plasmid # 185137) capsids were built by inserting 7-mer peptides between AAs 588-589 of the AAV9 cap gene in the pUCmini-iCAP-PHP.B backbone ((Deverman et al. 2016), Addgene plasmid # 103002). The AAV-PHP.S capsid was described previously ((Chan et al. 2017), Addgene plasmid # 103006).

For *in vivo* validation of AAV capsids, we packaged the vectors with a single-stranded (ss) rAAV genome: pAAV:CAG-2xNLS-EGFP (Deverman et al., 2016) (available from Caltech CLOVER Center upon request, a similar version with 1xNLS is in Addgene, plasmid # 104061), pAAV:CAG-EGFP, pAAV:hSyn1-tdTomato (a gift from Hongkui Zeng, Addgene plasmid # 51506, (Oh et al., 2014)), pAAV:CAG-tdTomato (a gift from Edward Boyden, Addgene plasmid # 59462), pAAV:hSyn-DIO-hM3D(Gq)-mCherry (a gift from Bryan Roth, Addgene plasmid # 44361, (Krashes et al., 2011)). To make the pAAV:CAG-jGCaMP8s plasmid, jGCaMP8s was synthesized as a gBlocks Gene Fragment (IDT) based on the sequence in the plasmid pGP-AAV-CAG-FLEX-jGCaMP8s-WPRE (Addgene plasmid # 162380) and subcloned into the plasmid pAAV:CAG-EGFP by replacing the EGFP gene.

AAV capsid library generation

The round-1 (R1) and round-2 (R2) libraries were generated as described previously (Ravindra Kumar et al, 2020). Briefly, the R1 library involved a randomized 21-nucleotide (7xNNK mutagenesis) insertion between AAs 588-589 of AAV9 capsid. The R2 library was built using a *synthetic pool* method (Ravindra Kumar et al. 2020). The R2 library was composed of an equimolar ratio of ~9000 variants that were recovered from the tissues of interest in R1 (DRG, heart, small and large intestine). The *Spike-in* variants as part of the *synthetic pool* library consisted of previously validated variants such as AAV-PHP.B, AAV-PHP.B4, AAV-PHP.C1 (CNS variants), AAV-PHP.S (PNS variant) and AAV9 parent.

In vivo selection and capsid library recovery

For capsid selection *in vivo*, the virus library was intravenously administered to male and female mice of various Cre transgenic lines (n=2-3 per Cre line) at $2x10^{11}$ vg per mouse in R1 selection, and at $1x10^{12}$ vg per mouse in R2 selection. Two weeks post injection, mice were euthanized, the organs of interest were harvested and snap-frozen on dry ice. The tissues were stored at −80°C for long-term. To recover capsids from the tissue, the tissues were processed using Trizol, and the rAAV genomes were recovered by Cre-dependent PCR or Cre-independent PCR as previously described (Ravindra Kumar et al., 2020). The AAV DNA library, virus library and the libraries recovered from tissue post *in vivo* selection were processed for NGS as also described previously (Ravindra Kumar et al., 2020).

AAV vector production for *in vivo* characterization

The AAV vectors were produced using an optimized vector production protocol (Challis et al., 2019). The average yield was ~ 1×10^{12} vg per plate.

AAV vector administration and tissue harvest in Mice

For the intravenous injection procedures in mice, the AAV vectors were injected intravenously via the retro-orbital route into 6-8 week old adult mice at a dose of $0.1\text{-}1 \times 10^{12}$ vg per mouse. The retro-orbital injections were performed as described previously (Yardeni et al., 2011; Challis et al., 2019). The expression times were ~3 weeks from the time of injection. The dosage and expression time were kept consistent across different experimental groups unless noted otherwise.

For the intraperitoneal injection procedures in mice, neonatal pups at postnatal stage 1 (P1) were intraperitoneally injected with the AAV vectors at a dose of 3×10^{11} or 1×10^{12} vg per mouse. Six weeks after AAV administration, tissue collections were performed.

To harvest the tissues of interest, the mice were anesthetized with Euthasol (pentobarbital sodium and phenytoin sodium solution, Virbac AH) and transcardially perfused using 30 – 50 mL of 0.1 M phosphate buffered saline (PBS) (pH 7.4), followed by 30-50 mL of 4% paraformaldehyde (PFA) in 0.1 M PBS. The organs were collected and post-fixed 24-48 h in 4% PFA at 4°C. Following this, the tissues were washed with 0.1 M PBS twice and stored in fresh PBS-azide (0.1 M PBS containing 0.05% sodium azide) at 4°C.

AAV vector administration and tissue harvest in Rat

Six 7-week-old male Sprague Dawley rats received lateral tail vein injections of either MaCPNS1 or MaCPNS2 (2×10^{13} vg/kg – 3 rats/group). After a 3-week incubation period, animals were transcardially perfused with saline followed by 4% PFA, as per a published protocol (dx.doi.org/10.17504/protocols.io.bahzib76). Tissues were then dissected out and post-fixed in 4% PFA for 1 h before being washed in 0.1 M PBS (3 × 30 min). Tissues were stored in PBS-azide until processing. In one rat (MaCPNS2 injection), the perfusion fixation process was unsuccessful, so tissues were fixed only by immersion (18-24 h), prior to washing and storage as described above.

AAV vector administration and tissue harvest in Marmoset

Marmoset monkeys were anesthetized using an intramuscular Ketamine (20 mg/kg) and Acepromazine (0.5 mg/kg) injection. An intravenous catheter was placed in the saphenous vein of the hind leg and flushed with ~2 mL of LRS (Lactated Ringer's solution) for 2 min. Viruses were pooled together in a single syringe (~500-900 µL) and infused at a rate of 200 µL/min into the catheter. Following the infusion, the catheter was flushed with ~3 mL of LRS for 2 min and removed. The animal was then returned to a recovery cage.

Following an incubation period of 4-6 weeks post viral injection, the animals were euthanized by injecting pentobarbital intraperitoneally. Two researchers worked in parallel to harvest the tissue as quickly as possible to limit degradation. Each organ-brain, lungs, kidneys, etc.-was removed and separated into two parts. One half of the tissue was flash-frozen in 2-methylbutane that was chilled with dry ice to preserve mRNA and DNA in the harvested tissues. The other half of the tissue was fixed in 4% PFA solution for estimation of protein expression. Flash-frozen tissue samples were transferred to a -80^{o}C freezer, while PFA-fixed tissue samples were stored in a 4^{o}C fridge.

AAV vector administration and tissue harvest in Rhesus Macaque

Two female rhesus macaques were injected within 10 days of birth. Prior to injection, animals were anesthetized with ketamine (0.1 mL) and the skin over the saphenous vein was shaved and sanitized. AAVs ($2.5x10^{13}$ vg/kg) were slowly infused into the saphenous vein for ~1 min in < 0.75 mL of 0.1 M PBS. Animals were monitored while they recovered from anesthesia in their home enclosure, and daily for the remainder of the study. Monkeys were individually housed within sight and sound of conspecifics.

Tissues were collected 4 weeks post AAV administration. Animals were deeply anesthetized and euthanized using sodium pentobarbital in accordance with guidelines for humane euthanasia of animals at the CNPRC. The whole body was perfused with ice cold RNase-free 0.1 M PBS. Brains were removed from the skull and blocked into 4 mm thick slabs in the coronal plane. Brain slabs and organs were subsequently post-fixed in 4% PFA for 48 h. One hemisphere of each animal was cryoprotected in 10%, 15%, and 30% sucrose in 0.1 M PBS.

Immunohistochemistry on tissues

In mice and NHP experiments, tissue sections, typically 100-µm thick, were first incubated in blocking buffer (10% normal donkey serum (NDS), 0.1% Triton X-100, and 0.01% sodium azide in 0.1 M PBS, pH 7.4) with primary antibodies (rabbit anti-NeuN (Abcam ab177487, 1:500), chicken anti-PGP9.5 (Invitrogen PA1-10011, 1:500), rabbit anti-S100 beta (Abcam ab52642, 1:200), rabbit anti-Parvalbumin (Abcam 181086, 1:200), rabbit anti-Olig2 (Abcam ab109186, 1:200), rabbit anti-GLUT1 (Millipore 07-1401, 1:200)) at appropriate dilutions for 24 h at room temperature (RT) on a rocker. After primary antibody incubation, the tissues were washed 1-3 times with wash buffer 1 (0.1% Triton X-100 in 0.1 M PBS buffer, pH 7.4) over a period of 5-6 h in total. The tissues were then incubated in blocking buffer with secondary antibodies (goat anti-chicken Alexa647 (Invitrogen, A32933, 1:1000), donkey anti-rabbit Alexa555 (Invitrogen, A21432, 1:1000), goat anti-rabbit Alexa647 (Invitrogen, A21245, 1:1000) at appropriate dilutions for 12-24h at RT and then washed 3 times in 0.1 M PBS over a total duration of 5-6 h. When performing DNA staining, the tissues were incubated with 4′,6-Diamidine-2′-phenylindole dihydrochloride (DAPI) (Sigma Aldrich, 10236276001, 1:1000) in 0.1 M PBS for 15 min followed by a single wash for 10 min in 0.1 M PBS. The DAPI and/or antibody-stained tissue sections were mounted with ProLong Diamond Antifade Mountant (ThermoFisher Scientific, P36970) before imaging under the microscope.

For immunostaining of DRG in mice neonates and the pain induction experiment, DRGs from spinal cord segments: thoracic levels 11-13 and lumbar levels 1-5 or 1-6 were dissected, fixed for 2 h in 4% PFA (diluted in 0.1 M PBS) at 4^{o}C, incubated overnight at 4^{o}C in 30% sucrose solution (diluted in 0.1 M PBS), and embedded in OCT (Tissue-Tek®). Sections of 14 µm thickness were cut and blocked with blocking buffer-1 (10% NDS, in PBST solution containing 0.3% Triton X-100 and 0.1 M PBS, pH 7.4) for 2 h at RT. Tissues were stained with primary antibodies (rabbit anti-CGRP (Millipore PC205L, 1:500), rabbit anti-Neurofilament 200 (Sigma N4142, 1:500), mouse anti-Tuj1 (Abcam ab7751, 1:1,000)) that were diluted in blocking buffer-2 (2% NDS in PBST solution) and incubated overnight at 4^{o}C. Sections were washed in PBST buffer, then stained with secondary antibodies (donkey anti-rabbit DyLight488 (Abcam ab96919, 1:1000), donkey anti-mouse Alexa647 (Abcam ab150107, 1:500)) diluted in blocking buffer-2 for 2 hour at RT. After washing with 0.1 M PBS, sections were mounted in VectaShield (Vector Labs), and imaged in an Olympus Fluoview 1000 confocal microscope with 20X magnification at HMS Microscopy Resources on the North Quad (MicRoN) Core. Five DRG images per mouse were used for quantification.

To immunostain rat organs and sensory ganglia, cryosections (14 µm) mounted onto gelatinized slides were washed in PBS (1 × 10 min) followed by 1 h incubation in blocking solution (PBS containing 0.1% Triton X-100 and 10% horse serum). Sections were incubated with primary antibody (hypertonic PBS, 18-24 h in a humid chamber), washed in PBS (1 × 15 min) and incubated with secondary antibody (2 h). Sections were again washed in PBS (1 × 15 min) and then coverslipped using buffered glycerol. This method is described in detail in (dx.doi.org/10.17504/protocols.io.w3ffgjn). DRG and trigeminal tissue were labelled for DsRed and each of the 3 markers (NF-200, CGRP, TRPV1) while liver tissue was labelled for DsRed and DAPI. Primary antibodies were: rabbit anti-dsRed (Takara Bio, 632496, 1:5000); mouse anti-neurofilament 200 (Sigma-Aldrich, N0142, 1:4000); goat anti-calcitonin gene-related peptide, Bio-Rad,1720-9007,1:5000); goat anti-TRPV1 (Neuromics, GT15129, 1:1000). Secondary antibodies were: donkey anti-rabbit AF594 (Jackson ImmunoResearch Laboratories, 711-585-152, 1:1000); donkey anti-mouse AF488 (Jackson, 715-545-150, 1:2000); donkey anti-goat AF488 (Jackson, 705-545-147, 1:1000).

To immunostain rat CNS, cryosections (40 µm) of brain (coronal) and L4-L5 spinal cord (transverse) were collected in a 1 in 4 series and stored in PBS-azide until use. Sections were washed in PBS (3 × 10 min) followed by 2 h incubation in blocking solution (PBS containing 0.5% Triton X-100 and 10% horse serum), washed in PBS (3 × 10 min) then incubated for 48 h with primary antibody (0.1% PBS-azide containing 0.5% Triton X-100 and 2% horse serum). Tissues were then washed in PBS (3 × 10 min) followed by 4 h incubation with secondary antibody. Tissues were washed in PBS (3 × 10 min) and then mounted and coverslipped using buffered glycerol. This method is described in detail in (dx.doi.org/10.17504/protocols.io.bakkicuw). Primary antibodies used were: rabbit anti-dsRed (Takara Bio, 632496, 1:5000) and mouse anti-NeuN (Chemicon, MAB377, 1:2000). Secondary antibodies are described above.

To immunostain whole mounts of autonomic ganglia (IMG, MPG, sympathetic chain) and intestine, tissues were washed in PBS (3 × 30 min) followed by 2 h incubation in blocking solution (PBS containing 0.5% Triton X-100 and 10% horse serum). Tissues were again washed in PBS (3 × 30 min) before 72 h incubation with primary antibody (0.1% PBS-Azide containing 0.5% Triton X-100 and 2% horse serum). Tissues were then washed in PBS (3 × 30 min) followed by 24 h incubation with secondary antibody. Tissues were washed in PBS (3 × 30 min) before being cleared using ethyl cinnamate (Masselink et al. 2019). Briefly, tissues were washed in methanol (100%, 3 × 30 min) followed by dichloromethane (1 × 30 min) and then ethyl cinnamate (2 × 30 min). Tissues were then mounted on glass slides and coverslipped using ethyl cinnamate.

Optical clearing for thick tissues

For imaging tissues >100 microns in thickness such as gut, optical clearing was carried out by incubating small pieces (0.5-1 cm length) of tissue in 1-2 mL of ScaleS4(0) (Hama et al., 2015) solution overnight at RT with gentle agitation. The tissues were then mounted in fresh ScaleS4(0) solution with spacers (0.1-1 mm thick) on glass slides and imaged under the microscope.

Tissue imaging and image processing

The images used in this study were acquired with a Zeiss LSM 880 confocal microscope using the following objectives: Plan-Apochromat 10X 0.45 M27 (working distance 2.0 mm), and Plan-Apochromat 25X 0.8 Imm Corr DIC M27 multi-immersion. The liver images were acquired with a Keyence BZ-X700 microscope using a 20X objective. The images were then processed in the following image processing software: Zen Black 2.3 SP1 (for Zeiss confocal images) and BZ-X Analyzer (for Keyence images).

Image collection and analysis for cryosections of rat sensory ganglia and organs was performed using wide-field fluorescence microscopy with an ApoTome attachment (Zeiss AxioImager M2). Quantification of AAV+ and AAV+/Marker+ neurons was performed for DRG and trigeminal ganglia on 4 non-sequential sections with only nucleated neuronal profiles counted. Counts were performed manually while viewing sections under the microscope. For CNS sections and whole mounts of intestine and ganglia, image collection and analysis was performed using wide-field fluorescence microscopy with an ApoTome attachment (Zeiss AxioImager M2).

Nodose calcium imaging experiment

In vivo vagal ganglion imaging was conducted as previously described (Williams et al. 2016). Briefly, animals were anesthetized with pentobarbital at a dose of 100 mg/kg body weight, injected intraperitoneally (i.p.). A skin incision was made to expose the abdominal region. For intestinal glucose infusion and distension, an input tubing (HelixMark Silicone Tubing 60-011-04) was inserted in the jejunum and the output tubing (HelixMark Silicone Tubing 60-011-09) was set at the ileum. Surgical thread was used to fasten and secure tubing sites. During the abdominal surgery, isotonic saline was applied occasionally to prevent tissue drying. After suturing the abdominal region, a midline neck incision was made. Muscles were separated and retracted laterally to expose the trachea and vagus trunk. To free the vagal ganglion, the carotid artery was retracted aside, and the vagus nerve was transected superior to the jugular ganglion. The vagal ganglion was then placed on a custom 5-mm diameter glass coverslip (72290-01, Electron Microscopy

Sciences), and immediately immersed in silicon adhesive (KWIK-SIL, World Precision Instruments). Imaging was conducted with a Leica SP8 confocal microscope, with a frame rate of 1 Hz. For glucose stimulus, 300 mM glucose solution was infused at a flow rate of 800 µL/min for 2 min. Intestinal distension stimulus was achieved by closing the exit port for 1 min while infusing saline.

Pain behavior experiment

Trpv1-Cre neonatal pups at postnatal stage 1 (P1) were intraperitoneally injected with 10 µL of MaCPNS1:Syn-DIO-hM3D(Gq)-mCherry virus ($3\text{x}10^{13}$ vg/ml). Six weeks after injection, mice were subjected to a pain test in an infrared Behavior Observation Box (iBOB) (Harvard Apparatus) which allowed video recording of mice in the dark and independent of an observer. Prior to Clozapine-N-oxide (CNO) injection, mice were habituated for 30 min in individual chambers of the iBOB. Mice were then given intraplantar injection of 10 µL of CNO or vehicle (5% Dimethyl sulfoxide (DMSO) in 0.1 M PBS). Injections were performed under light restraint without anesthesia. Mice were immediately placed in the iBOB and recorded. Total bouts of lifting/licking of the footpad and total time spent licking/lifting the footpad for the first 15 minutes after CNO injection were quantified.

Analysis of pain behavior

The 20-min videos recorded in the pain-induction experiment were scored by a blinded observer to quantify the total bouts and time spent licking and shaking the injected paw within 15 min. GraphPad Prism was used for statistical comparison and plotting.

Quantification of AAV transduction *in vivo*

The quantification of AAV transduction across NG, DRG and GI tract was carried out by manually counting fluorescent expression resulting from the AAV genome. The Adobe Photoshop CC 2018 Count Tool was used for this purpose. To quantify expression in the liver, we used Keyence Analyzer automated cell count software. The efficiency was determined by the percentage of cells expressing EGFP or tdTomato relative to a specific cell marker, namely, NeuN, PGP9.5, DAPI, CGRP, NF200, TRPV1, Tuj1, GLUT1, Olig2 or S100β.

NGS data alignment, processing and analysis

The raw fastq DNA files were aligned to the AAV9 capsid template using custom alignment software as described previously (Ravindra Kumar et al. 2020) (https://github.com/GradinaruLab/mCREATE). The NGS data analysis was carried out using a custom data-processing pipeline with scripts written in Python https://github.com/GradinaruLab/mCREATE) and plotting software such as Plotly, Seaborn, and GraphPad PRISM 7.05. The AAV9 capsid structure model was produced with PyMOL.

The enrichment score for a variant was determined using the following formula: Enrichment score of variant “x” = log10 [(Variant “x” RC in tissue library1/ Sum of variants N RC in library1) / (Variant 1 RC in virus library/ Sum of variants N RC in virus library)] Where N is the total number of variants in a library. The fold-change of a variant “x” to AAV9 = (The enrichment of “x”-The enrichment of AAV9)/|The enrichment of AAV9|.

UMAP Clustering analysis

For profiling the overall tropism of the AAV library post R2 selection, a non-linear algorithm, UMAP (McInnes, Healy, and Melville 2020), was used for dimension reduction and visualization with a script adapted from https://github.com/lmcinnes/umap. After the M-CREATE data-processing pipeline, the R2 capsid library yielded enrichment scores across 22 targets (tissues, Fig. 1B). These enrichment scores served as 22 dimensions that were fed into the UMAP algorithm, and the parameters considered were n_neighbors (15), n_components (2), random_state (42), distance_metric ('correlation'), verbose (3).

Data analysis for calcium imaging

Imaging data was analyzed using CaImAn-MATLAB (Giovannucci et al. 2019; Corder et al. 2019) with modified MATLAB code adapted from https://github.com/flatironinstitute/CaImAn-MATLAB. Basically, imaging frames from the same animal were first registered to correct for motion. A non-negative matrix factorization (CNMF) algorithm was applied to recognize individual cells and to extract fluorescence activities. A 30 s window before the stimulus onset was used as baseline signal. To quantify signals, the mean (μ) and standard deviation (σ) of $F0(t)$ over the baseline period were computed as $F(t) = (F0(t) - \mu)/\sigma$. Cells were defined as responsive if the average $\Delta F/F(\sigma)$ value during the stimulus period was more than 3 s.d. above the baseline mean activity.

2.12 OTHER INFORMATION

Acknowledgments

We thank members of the Gradinaru group for their assistance in this study: Yaping Lei for help with virus production, Elisha Mackey for mouse colony management, Tim Miles, Zhe Qu, and Erin Sullivan for lab management, Miguel Chuapoco for discussion, on NHP experiments, Patricia Anguiano for administrative assistance and the entire Gradinaru group for discussions. We thank I. Antoshechkin and the Millard and Muriel Jacobs Genetics and Genomics Laboratory at Caltech for providing sequencing service. We thank Cassandra Tang-Wing and Chris Chamberlain at UCSD for the injection of the marmoset. We thank Michael Metke and Vikram Pal Singh at UCSD for the tissue collection from marmoset. We thank the staff at the California National Primate Research Center for support of the macaque experiment. We thank Catherine Oikonomou for help with manuscript editing. Diagrams in figures were created with BioRender.com.

This work was primarily supported by grants from the National Institutes of Health (NIH) to V.G.: NIH BRAIN R01MH117069, NIH Pioneer DP1OD025535 and SPARC 1OT2OD024899. Additional funding includes: (to V.G.) the Vallee Foundation, the Moore

Foundation, the CZI Neurodegeneration Challenge Network, and the NSF NeuroNex Technology Hub grant 1707316, a grant from the Pew Charitable Trusts, the Heritage Medical Research Institute and the Beckman Institute for CLARITY, Optogenetics and Vector Engineering Research (CLOVER) for technology development and dissemination; NIH R01 DK127257 (to I.M.C.); CZI Neurodegeneration Challenge Network (to I.M.C.); NIH R01 DC012087 (to C.T.M.); NIH P51 OD011107 (to A.S.F.); BRAIN Initiative Armamentarium UF1MH128336 (to V.G., A.S.F., C.T.M.); Department of Defense grant W81XWH-17-1-0588 (to S.K.M. and V.G.); and NIH SPARC 3OT2OD023872 (to J.R.K.).

Author contributions

X.C., S.R.K., and V.G. designed the experiments. X.C., S.R.K., C.A., J.K., D.Y., T.W., D.W., V.N., L.C. performed experiments. C.D.A., J.R.K., and P.B.O. assisted with the characterization of variants in rats. D.Y. and I.M.C. assisted with the characterization of the virus in pups and performed the pain induction experiment. T.W. and T.I. assisted with the calcium imaging experiment. D.A.W. assisted with the library selection and characterization of the virus in mice. C.M.A. assisted with the characterization of the DRG and spinal cord of NHPs. V.N. and C.T.M. assisted with the characterization of the virus in marmoset with the support of vet staff at UCSD. L.J.C. and A.S.F. assisted with the characterization of the virus in rhesus macaque with the support of the staff at the California National Primate Research Center. J.A.G. and S.K.M. assisted with the characterization of the virus in mice ENS. X.C. and S.R.K. prepared the figures with input from all authors. X.C., S.R.K., and V.G. wrote the manuscript with input from all authors. V.G. supervised all aspects of the work.

Declaration of interests

The California Institute of Technology has filed and licensed patent applications for some of the work described in this manuscript, with X.C., S.R.K., and V.G. listed as inventors. V.G. is a cofounder and board member of Capsida Biotherapeutics, a fully integrated AAV engineering and gene therapy company. The remaining authors are not aware of any affiliations, memberships, funding, or financial holdings that might be perceived as affecting the objectivity of this paper.

Chapter 3

FUNCTIONAL GENE DELIVERY TO AND ACROSS BRAIN VASCULATURE OF SYSTEMIC AAVS WITH ENDOTHELIAL-SPECIFIC TROPISM IN RODENTS AND BROAD TROPISM IN PRIMATES

Chen, Xinhong, Damien A. Wolfe, Dhanesh Sivadasan Bindu, Mengying Zhang, Naz Taskin, David Goertsen, Timothy F. Shay, Erin E. Sullivan, Sheng-Fu Huang, Sripriya Ravindra Kumar, Cynthia M. Arokiaraj, Viktor Plattner, Lillian J. Campos, John K. Mich, Deja Monet, Victoria Ngo, Xiaozhe Ding, Victoria Omstead, Natalie Weed, Yeme Bishaw, Bryan Gore, Ed S. Lein, Athena Akrami, Cory Miller, Boaz P. Levi, Annika Keller, Jonathan T. Ting, Andrew S. Fox, Cagla Eroglu, Viviana Gradinaru*. 2023. Functional gene delivery to and across brain vasculature of systemic AAVs with endothelial-specific tropism in rodents and broad tropism in primates. *bioRixv*, 2023.01.12.523844. https://doi.org/10.1101/2023.01.12.523844

3.1 SUMMARY

Delivering genes to and across the brain vasculature efficiently and specifically across species remains a critical challenge for addressing neurological diseases. We have evolved adeno-associated virus (AAV9) capsids into vectors that transduce brain endothelial cells specifically and efficiently following systemic administration in wild-type mice with diverse genetic backgrounds and rats. These AAVs also exhibit superior transduction of the CNS across non-human primates (marmosets and rhesus macaques), and *ex vivo* human brain slices although the endothelial tropism is not conserved across species. The capsid modifications translate from AAV9 to other serotypes such as AAV1 and AAV-DJ, enabling serotype switching for sequential AAV administration in mice. We demonstrate that the endothelial specific mouse capsids can be used to genetically engineer

the blood-brain barrier by transforming the mouse brain vasculature into a functional biofactory. Vasculature-secreted Hevin (a synaptogenic protein) rescued synaptic deficits in a mouse model.

3.2 INTRODUCTION

Malfunction of cell types comprising vasculature within the brain, including endothelial cells, can facilitate the progression of neurological disorders (Yu, Ji, and Shao, 2020; Xiao et al., 2020; Profaci et al., 2020; Yang et al., 2022). However, the study of vasculature is hampered by limited options for versatile, cell-type-specific transgene delivery. Adeno-associated virus (AAV) vectors offer promise for gene delivery to the brain, but are commonly administered via intracranial injections, resulting in tissue damage and limited and uneven spatial coverage (Aschauer, Kreuz, and Rumpel, 2013; Watakabe et al., 2015). Systemic AAV delivery provides a non-invasive, brain-wide alternative (Deverman et al., 2018; Hudry and Vandenberghe, 2019; Chen et al., 2022; Challis et al., 2022), but specifically targeting cell types of interest remains a challenge.

Having previously engineered vectors that efficiently cross the blood-brain barrier (BBB) with broad tropism in rodents (e.g. AAV-PHP.eB) (Deverman et al., 2016; Chan et al., 2017; Ravindra Kumar et al., 2020; Goertsen et al., 2021), we recently turned our focus to identifying vectors with cell-type biased tropism. From the PHP.B sequence family, we identified PHP.V1, which, when intravenously delivered, has enhanced potency for endothelial cells although it also transduces astrocytes and neurons (Ravindra Kumar et al., 2020). While an improvement, PHP.V1 still requires cell type-specific promoters whose large size limits the choice of transgenes and only work in certain mice strains. In addition, capsid entry into other cell types may induce an immune response, creating a confounding effect. Similar problems also apply to the previously-reported BR1 endothelial variant, BR1 transduces a large number of neurons and astrocytes other than endothelial cells (Körbelin et al., 2016; Sundaram et al., 2021). With the increasing numbers of engineered AAVs reported, there are also increasing examples showing their potential distinct tropism across species (Chen et al., 2022; Challis et al., 2022), emphasizing the necessity for the testing of engineered variants in different species especially non-human primates.

Another challenge remaining for AAV gene delivery is successful re-administration, which may be needed to maximize therapeutic effect, particularly given the loss of transgene expression over time observed with AAV gene delivery (Greig et al., 2022). While neutralizing antibodies induced by initial AAV administration can prevent sequential administration of the same AAV (Hamilton and Wright, 2021), switching to another AAV serotype with similar or complementary features is a potential solution (Bočkor et al., 2017; Colella, Ronzitti, and Mingozzi, 2018) that remains underexplored.

An AAV with potent and specific tropism for brain vasculature would enable new strategies for gene therapy. As the leading platform for *in vivo* delivery of gene therapies, AAV vectors have been used to deliver diverse therapeutic genes to treat a broad spectrum of disorders (Lykken et al., 2018; Wang, Tai, and Gao, 2019), including those resulting from loss of either cell-autonomous factors or factors which act on neighboring cells regardless of genotype. For disorders caused by the loss of function of a single non-cell-autonomous factor, such as mucopolysaccharidosis (Sawamoto et al., 2018), the factor is typically a secreted protein (Lykken et al., 2018). In these cases, gene therapy could target a healthy cell population, transforming those cells into a ‘biofactory’ for production and secretion of a therapeutic protein that could cross-correct affected cells. Currently, however, therapeutic proteins produced from peripheral biofactories, most commonly the liver, enter the CNS with low efficiency and fall short of rescuing phenotypes in CNS disorders (Ponder and Haskins, 2007; Zapolnik and Pyrkosz, 2021). Given its broad distribution and close proximity to other cell types within the CNS, AAV-transformed brain vasculature may serve as a better biofactory for the CNS.

Here, through a combination of directed evolution and semi-rational engineering, we identified a family of novel vectors, including AAV-X1 and AAV-X1.1, which target brain endothelial cells specifically and efficiently following systemic delivery in mice with a ubiquitous promoter. We characterized these novel AAVs across rodent models (genetically diverse mouse strains and rats), non-human primates (marmosets and rhesus macaques), and *ex vivo* human brain slices, demonstrating brain endothelial-specific cell targeting in rodent and broad CNS targeting in primates. To illustrate the utility of AAV-X1 for CNS delivery of neuroactive proteins, we transformed mouse brain endothelial cells into a biofactory for producing the synaptogenic protein Sparc-like protein 1 (Sparcl1)/Hevin. Hevin/Sparcl1 is an astrocyte-secreted protein that controls formation of vesicular glutamate transporter 2 (VGluT2)-containing synapses such as thalamocortical synapses (Kucukdereli et al., 2011; Risher et al., 2014; Singh et al., 2016). AAV-X1-mediated ectopic expression of Sparcl1/Hevin in brain endothelial cells was sufficient to rescue the thalamocortical synaptic loss phenotype of Sparcl1/Hevin knockout mice. We also demonstrated the transferability of AAV-X1's properties from the AAV9 serotype to AAV1, enabling repeated AAV administration to increase CNS transduction. In general, we provide novel engineered systemic AAVs for brain endothelial-specific cell targeting in rodent and broad CNS targeting from rodent to primate with potential for re-administration.

3.3 A NOVEL AAV CAPSID SPECIFICALLY TARGETS BRAIN ENDOTHELIAL CELLS IN MICE FOLLOWING SYSTEMIC ADMINISTRATION

As a starting point for engineering, we chose AAV9, which targets the CNS with low efficiency following systemic delivery. We inserted randomized 7-mer peptides between positions 588 and 589 of AAV9 and injected the resulting virus library intravenously into transgenic mice expressing Cre from either the Tek (targeting endothelial cells) or Synapsin I (Syn, targeting neuronal cells) promoter. After 2 rounds of M-CREATE selection (Ravindra Kumar et al., 2020), we identified a variant, named AAV-X1, which is among the most enriched in Tek-Cre mice, indicating potential endothelial tropism in mice (Fig. 1A). To characterize the transduction profile of AAV-X1 *in vivo* we packaged it with a single-stranded (ss) AAV genome carrying a strong ubiquitous promoter, CAG, driving the expression of an eGFP reporter. Three weeks after IV administration to C57/BL/6J mice, we observed specific and efficient targeting of the vasculature across brain regions

(Fig. 1B). To compare the vascular targeting of AAV-X1 to that of previously engineered capsids, we repeated the experiment along with AAV9, AAV-PHP.V1, and AAV-BR1 (Körbelin et al., 2016; Ravindra Kumar et al., 2020). After 3 weeks of expression, AAV-X1 exhibited higher efficiency and higher specificity in targeting brain endothelial cells compared to all 3 controls (Fig. 1C). At a dose of 3 x 1011 viral genomes (vg) per mouse, AAV-X1 transduced ~65-70% of GLUT1+ (endothelial markers) cells across the cortex, hippocampus and thalamus. In comparison, AAV-PHP.V1 and AAV-BR1 transduced ~40% of GLUT1+ cells, while AAV9 transduced ~1% of the endothelial cells. AAV-X1 also exhibited superior specificity towards vasculature; ~95% of the cells transduced by AAV-X1 were GLUT1+. In contrast, AAV-BR1 and AAV-PHP.V1 transduced GLUT1+ cells with much less specificity, with only 60% and 40% of transduced cells being GLUT1+, respectively. AAV-BR1 also targeted neurons, while AAV-PHP.V1 also targeted neurons and astrocytes (Fig. 1C). Further staining with CD31 or Podocalyxin (endothelial cells), Calponin 1 (smooth muscle cells), CD206 (perivascular macrophages), GFAP (astrocytes) and CD13 (pericytes) confirmed the high efficiency and specificity of AAV-X1 in targeting brain endothelial cells (Supplementary Fig. 1A-D). Interestingly, the endothelial cells in the choroid plexus (CP) were not transduced by AAV-X1 (Supplementary Fig. 1C). In summary, the novel vector AAV-X1 not only exhibits significant improvement in targeting the CNS compared to its parent AAV9 but also shows high specificity towards brain endothelial cells.

3.4 SEMI-RATIONAL REFINEMENT OF X1'S PERIPHERAL TROPISM BY FURTHER ENGINEERING CARGO AND CAPSID

While the novel variant X1 exhibited significant improvement in transducing the CNS endothelium compared to AAV9, it maintained a similar level of liver transduction. Therefore, we next explored strategies to further refine the vector's tropism, either by incorporating specific cargo elements or by further engineering the capsid (Fig. 2A).

We first explored whether adding a regulatory element to X1's cargo could reduce liver expression. When incorporated into the genome, microRNA target sites induce microRNA-mediated post-transcriptional transgene silencing (Anja Geisler and Fechner, 2016). MicroRNA-122 (miR-122) is highly specific to the liver (Isakova et al., 2020) and incorporation of its target site has been shown to reduce AAV expression in the liver (Geisler et al., 2011). We cloned 3 copies of miR-122's target site (TS) into a CAG-eGFP genome and packaged it in the X1 vector. Three weeks after IV delivery of X1: CAG-eGFP-miR122TS, we observed a large reduction in liver expression, indicating that future applications of X1 could incorporate miR-122 TS for liver detargeting (Fig. 2B, bottom left panel).

While cargo engineering reduced transgene expression in the liver, the AAV capsid still entered the liver and might trigger an immune response. Therefore, we next explored whether further engineering of the X1 capsid could achieve similar liver detargeting, and potentially further boost CNS transduction. Structural information (DiMattia et al., 2012) and previous engineering efforts (Goertsen et al., 2021) suggest that the 455 loop of AAV9 potentially interacts with the 588 loop and affects receptor binding. A 7-mer substitution of 452-458 of PHP.eB was found to further boost that capsid's CNS targeting ability and enable potent transduction of the mouse and marmoset CNS while detargeting the AAV from the liver (Goertsen et al., 2021). We therefore took three 7-mer peptides identified from that PHP.eB 455 loop selection and substituted them into X1, creating X1.1, X1.2, and X1.3. Compared to X1, X1.1 showed further improvement in targeting the CNS, transducing ~82-85% of GLUT1+ cells across brain regions (Fig. 2B-C). X1.1 also maintained high specificity in targeting the brain vasculature; ~90-92% of transduced cells were GLUT1+ (Fig. 2C, right). X1.1 showed a similar expression pattern as X1 and AAV9 in peripheral organ and both weren't vasculature-tropic in the peripheral organs (Supplementary Fig. 2A-B). To fully capture X1.1's performance across organs, we measured its vector genome and RNA transcript following systemic administration in mice. We observed X1.1's increased presence in CNS and X1.1's reduced targeting of some peripheral organs compared to AAV9 especially in RNA transcript presence. In some organs such as heart, higher DNA while lower RNA presence may suggest likely non-specific vascular uptake, which would require further investigation (Supplementary Fig. 2C-F). Some application in mice would require a higher dose of AAVs, we thus injected X1.1 with higher doses and verified that it maintained its high specificity against brain endothelial cells (Supplementary Fig. 2G-H). X1.1 was capable of packaging viral genomes with similar efficiency to AAV9 (Fig. 2D). Given X1.1's high transduction efficiency of brain endothelial cells, we performed a dye perfusion experiment to evaluate whether AAV transduction may compromise BBB integrity. We did not detect increased leakage in the BBB compared to uninjected mice (Supplementary Fig. 3A).

Having seen that X1 can accommodate additional capsid changes, we next investigated whether we could optimize the vector's tropism by mutating sites known to mediate receptor interactions and affect tropism. N272 and W503 have been shown to be required for AAV9's binding to galactose (Pulicherla et al. ,2011; Shen et al., 2012; Bell et al., 2012; Adachi et al., 2014), and mutation of W503 has been shown to reduce the liver transduction of AAV9 (Pulicherla et al., 2011). We therefore decided to mutate N272 or W503 of X1 to alanine, yielding X1.4 and X1.5, respectively. S386 of AAV9 and Q386 of AAV1 have also been shown to mediate receptor interaction (Adachi et al., 2014; Zhang et al., 2019), so we mutated S386 of X1 to alanine, yielding X1.6. Following IV delivery of these vectors in mice, we observed that X1.4 and X1.5 showed reduced liver transduction while maintaining their brain-endothelial tropism (Fig. 2B, bottom).

To explore the novel vectors' potential for application in different physiological contexts, we tested the X1.1 vector in young (2.5 months old) versus aged mice (2.5 years old) and did not observe an obvious difference in CNS transduction after 3 weeks' expression. We also did not observe an obvious sex difference in its CNS tropism (Supplementary Fig. 3B).

3.5 X1 VECTORS TRANSDUCE BRAIN ENDOTHELIAL CELLS ACROSS DIVERSE MOUSE STRAINS AND RATS IN A LY6A-INDEPENDENT MANNER

The previously-engineered AAV-PHP.eB has been shown to rely on improved binding to Ly6a for its increased CNS tropism (Hordeaux et al., 2019; Huang et al., 2019; Batista et al., 2020), and polymorphism of Ly6a across mouse strains contributes to its strain-specific phenotype (Hordeaux et al., 2019; Huang et al., 2019). We therefore explored whether the improved CNS targeting of X1 and its further-engineered versions is also dependent on Ly6a binding. We observed that transient overexpression of Ly6a in HEK cells boosted PHP.eB transduction but had no significant effect on X1 transduction (Supplementary Fig. 3C). Surface Plasmon Resonance (SPR) experiments designed to amplify even weak interactions with Ly6a showed that while both PHP.eB and PHP.V1 exhibited strong binding to Ly6a, explaining the strain-specific phenotype of PHP.V1 (Fig. 3A) (Ravindra Kumar et al., 2020), neither X1 nor X1.1 bound Ly6a (Fig. 3A). These results suggest that X1 and its derivatives utilize a novel mechanism of cell targeting.

The Ly6a-independence of the X1 vectors prompted us to test their translatability across mice strains. Systemic delivery of X1 capsid packaged with ssAAV:CAG-eGFP in BALB/cJ, CBA/J, and FVB/NJ mouse strains resulted in efficient transduction of endothelial cells across brain regions (Fig. 3B,C). Interestingly, though, we observed different expression patterns in the liver across the strains, with minimal liver transduction in BALB/c and CBA/J strains (Fig. 3C).

We next investigated the new variants' transduction profile in rats. Following intravenous delivery of X1.1 capsid packaging ssAAV:CAG-tdTomato in adult Lister Hooded rats, we observed robust expression in the brain (Fig. 3D). X1.1-induced expression overlapped with GLUT1+, indicating that its tropism towards endothelial cells is conserved (Fig. 3E).

To explore tropism when the BBB is not intact, we next tested the vectors in pericyte-deficient mice (Supplementary Fig. 3D) (Armulik et al., 2010; Mäe et al., 2021). We observed increased transduction of other cell types compared to control mice (Supplementary Fig. 3E). Interestingly, astrocytes with end-feet on the brain vasculature were transduced in pericyte-deficient mice but not in control mice (Supplementary Fig. 3F), indicating that the novel vectors' specificity towards endothelial cells may be dependent on the status of the BBB.

3.6 SEROTYPE SWITCHING OF X1 FROM AAV9 INTO AAV1 ENABLES REPEATED ADMINISTRATION OF AAV, INCREASING PERMEABILITY OF THE MOUSE CNS TO AAVS

Repeated administration of AAV is desired for certain applications, however, neutralizing antibodies induced by an initial administration prevent the subsequent delivery of similar AAVs (Bortolussi et al., 2014; Colella, Ronzitti, and Mingozzi, 2018). One potential solution is to switch AAV serotypes in sequential administrations, but most of the novel AAVs engineered to target the CNS, including PHP.B and AAV-X1, are based on AAV9. To overcome this potential hurdle and enable repeated administration, we sought to transfer the X1 peptide and recreate our engineered AAV in another natural serotype.

Mixed results have been reported for previous attempts to directly transfer the PHP.B or PHP.eB peptide to natural serotypes, usually AAV1 due to its CNS tropism (Tan et al., 2019; Lau et al., 2019; Martino et al., 2021; Pietersz et al., 2021). We inserted the 7-mer peptide of PHP.B into the AAV1 capsid, creating the hybrid AAV1-PHP.B (Fig. 4B). Intravenous injection of adult mice with AAV1-PHP.B packaging CAG-eGFP showed no obvious improvement in brain transduction compared to AAV1. However, AAV1-X1, created by a similar strategy, showed robust CNS expression in a pattern similar to that of X1, efficiently and specifically targeting GLUT1+ endothelial cells (Fig. 4C). We also tried tested similar strategy and inserted the X1 peptide in AAV-DJ, creating AAV-DJ-X1. Similar to AAV1-X1, AAV-DJ-X1 showed improved CNS targeting compared to AAV-DJ following systemic delivery (Supplementary Fig. 4A). These results indicate that X1's phenotype can be transferred to some other serotypes by transferring the 7-mer peptide, while it would need to be tested individually for each new serotype.

To test AAV1-X1's potential to enable repeated administration, we utilized the virus for Ly6a supplementation. Polymorphisms in Ly6a in certain mouse strains such as CBA/J and BALB/cJ greatly reduce the CNS permeability of PHP.eB (Hordeaux et al., 2019; Huang et al., 2019; Batista et al., 2020). The brain endothelial cell tropism of X1 and AAV1-X1 prompted us to utilize them to express C57BL/6J-like Ly6a in the BBB of these non-permissive strains, and thereby increase the permeability of those animals' BBB for AAV9-based PHP.eB when it is subsequently administered. We intravenously delivered AAV1-X1 or X1.1 capsid packaged with Ly6a into adult CBA/J mice. After three weeks of expression, we then injected PHP.eB packaged with eGFP into the same mice (Fig. 4A, D). We observed increased eGFP expression in the brains of CBA/J mice injected with AAV1-X1: CAG-Ly6a but not the mice injected with X1.1: CAG-Ly6a, indicating that AAV1-X1 enables the subsequent administration of PHP.eB and also facilitates the permeability of PHP.eB (Fig. 4D). This result indicates that the serotype switching paradigm enabled by AAV1-X1 could potentially provide a solution for AAV re-administration in mice.

3.7 THE X1.1 VECTOR CAN TRANSFORM BRAIN ENDOTHELIAL CELLS INTO A BIOFACTORY FOR SECRETED PROTEIN DELIVERY TO THE BRAIN

The broad distribution of vasculature across brain regions creates the opportunity to transform endothelial cells into a biofactory for the broad production of therapeutic agents such as secreted proteins with trophic properties for other cell types within the CNS. For secreted proteins, this would remove the production burden from the target cell, which may already reside in a disease state. Since our novel vectors transduce brain endothelial cells efficiently and specifically, they provide a unique tool for us to explore this concept.

Sparc-like protein 1 (Sparcl1), which is also known as Hevin, is a matricellular secreted protein that is predominantly expressed by astrocytes and a subset of neurons in the CNS. Endothelial cells also express Sparcl1 mRNA; however, protein expression by these cells has not been observed (Lloyd-Burton and Roskams, 2012; Mongrédien et al., 2019). Downregulation or missense mutations in SPARCL1/Hevin have been reported in numerous neurological disorders such as autism, schizophrenia and depression (Kähler et al., 2008; Zhurov et al., 2012; De Rubeis et al., 2014). In the developing mouse visual cortex, Hevin is specifically required for the formation and plasticity of thalamocortical connections (Risher et al., 2014; Singh et al., 2016). Hevin knockout mice (Hevin KO) display a dramatic loss of Vesicular Glutamate Transporter 2 positive (VGluT2+) thalamocortical synapses both in the first three postnatal weeks and as adults (Fig. 4E) (Risher et al., 2014).

To determine if ectopic expression of Hevin by CNS endothelial cells can rescue the deficits observed in Hevin KO mice, we generated a viral vector for Hevin expression using our capsid AAV X1.1. Indeed, AAV X1.1 packaging Hevin efficiently transduced brain endothelial cells and drove the expression of Hevin in these cells. To investigate whether Hevin production via endothelial cells would rescue the deficits in thalamocortical synapses observed in Hevin KO mice, we retro-orbitally delivered both Hevin-HA and eGFP driven by the CAG promoter into 4-month-old Hevin KO mice (Fig. 4E). After 3 weeks, we observed robust and specific expression of transgenes in brain endothelial cells (Fig. 4F; Supplementary Figure. 4B-C). Further, a synapse assay using the presynaptic thalamocortical marker VGlut2 and postsynaptic marker PSD95 in Hevin KO mice showed a significantly higher number of thalamocortical synapses in layer IV of the V1 cortex in the treated group (CAG-Hevin) compared to the control (CAG-eGFP) (Fig. 4G). This result indicates that the Hevin produced and secreted from the brain endothelial cells was able to mimic endogenous Hevin function, rescuing the thalamocortical synapse formation that is severely deficient in Hevin KO mice. This system thus illustrates a new potential therapeutic strategy for Hevin-related disorders.

3.8 THE X1 VECTOR FAMILY EFFICIENTLY TRANSDUCES HUMAN BRAIN ENDOTHELIAL CELLS *IN VITRO*

After validating the novel vectors' transduction profiles and demonstrating their functional application in rodent species, we next explored translation to higher organisms. We measured the performance of X1 in transducing isolated human brain microvascular endothelial cells (HBMECs). At an MOI of 3 x 10^4, X1 transduced ~42% of HBMECs, ~180 fold higher than its parent AAV9. The further engineered versions X1.1 and X1.2 transduced 44% and 53% of HBMECs, respectively. In contrast, previously-engineered AAV vectors including PHP.eB and BR1 transduced ~0-2% of HBMECs, showing no obvious improvement in transduction compared to natural serotypes (Fig. 5A). AAV1-X1 and AAV-DJ-X1 also showed improvement in transduction pf HBMECs compared to their parent serotype, respectively (Supplementary Figure. 4D). We next examined the vectors' performance at a lower MOI of 3 x 10^3 and again observed an improvement in transduction efficiency for X1.1 and X1.2, which transduced ~22% and ~28% of HBMECs (Fig. 5A). In addition to transducing HBMECs, X1 and its engineered derivatives exhibited robust transduction of multiple other human-derived cell lines, including HeLa, U87 and IMR-32 (Supplementary Fig. 4A).

3.9 X1.1 EFFICIENTLY TRANSDUCES CULTURED *EX VIVO* BRAIN SLICES FROM MACAQUE AND HUMAN

The strong performance of the novel vectors in HBMECs prompted us to investigate their efficacy in a system that may better mimic *in vivo* conditions in non-human primates. We thus turned to an *ex vivo* brain slice culture system (Fig. 5B). The brain slices were freshly extracted from primate brains and cultured ex vivo. The versatile nature of this ex vivo system provides us with a rare opportunity to compare most of the CNS-tropic AAVs engineered in our lab within the same condition in primate tissue. We packaged CAG-Frataxin(FXN)-HA with unique 12bp barcodes in a panel of AAVs including AAV9, X1.1, and several other engineered CNS-tropic AAVs. We then injected them both individually and together as a pool into brain slices freshly extracted from the southern pig-tailed macaque (*Macaca nemestrina*) and cultured in physiological conditions (Fig. 5B). After 7-10 days, we extracted DNA and RNA from the tissue, and calculated the enrichments of the variants from the AAV pool in the tissue using next-generation sequencing (NGS). X1.1 showed an ~3-fold increase and ~24-fold increase in DNA and RNA, respectively, compared to AAV9. This outperformed all other vectors, including CAP-B10 and CAP-B22, which have been shown to have increased efficiency in transducing the CNS of marmosets after systemic delivery (Goertsen et al., 2021) (Fig. 5C). The previously-reported MaCPNS2, which has increased targeting of the macaque CNS, also showed an ~5-fold increase in RNA compared to AAV9 (Chen et al., 2022) (Fig. 5C). We also observed a higher DNA and RNA presence of X1.1 compared to other AAVs in the pool in the rhesus macaque brain (Supplementary Fig. 5A-B). Immunohistochemistry (IHC) staining of the HA tag confirmed the robust transduction by X1.1 in pig-tailed macaque (Fig. 5D; Supplementary Fig. 5C). Interestingly, X1.1-induced protein expression in the *ex vivo* brain slices were mostly seen in neurons (Fig. 5D; Supplementary Fig. 5D). RNA scope experiment revealed that some X1.1-deliverered GFP mRNA transcripts were also observed in GLUT1+ cells while most of them remained in neurons (Supplementary Fig. 5E-F).

We then performed similar testing on human brain slices originating from a biopsy surgery. X1.1 showed an ~4-fold and ~32-fold increase in DNA and RNA, respectively, compared to AAV9, again outperforming several previously-engineered CNS-targeting vectors (Fig. 5E). The strong performance of X1.1 across macaque and human *ex vivo* slices (Fig. 5F) suggests great potential for the capsid in future translational applications.

3.10 X1.1 EFFICIENTLY TARGETS THE CNS IN RHESUS MACAQUE FOLLOWING IV DELIVERY

Having validated the new variants' transduction profiles in *ex vivo* NHP and human brain models, we decided to investigate their efficacy *in vivo*. We first tested them in the marmoset, a New World monkey. To reduce animal subject numbers, we simultaneously tested two viral capsids (AAV9 and X1.1) packaging different fluorescent reporters (either ssAAV:CAG-eGFP or ssAAV:CAG-tdTomato) in each adult marmoset (Supplementary

Fig. 6A). 3 weeks after IV delivery of the viruses, we observed no obvious differences between the CNS transduction of X1.1 and AAV9 (Supplementary Fig. 6B-C). This result emphasizes again that BBB heterogeneity should be taken into account when performing AAV engineering.

We then tested their efficacy in the rhesus macaque, an Old World monkey. We intravenously injected a pool of AAV9 and X1.1 each packaged a unique barcode into a neonate rhesus macaque (male *Macaca mulatta*, within 10 days of birth, $1x10^{13}$ vg/kg per AAV, n=1 per group) (Supplementary Fig. 7A). After 4 weeks of expression, X1.1 showed an increase in vector genome and RNA transcript across brain regions include cortex, hippocampus and cerebellum, compared to AAV9 (Supplementary Fig. 7B-D). In peripheral tissue such as liver, muscle and enteric system, X1.1 showed a reduction in both DNA and RNA compared to AAV9 (Supplementary Fig. 7B-D). After seeing X1.1 superior performance in targeting CNS while detargeting from peripheral at DNA and RNA levels, we next examined its cell-type targeting profile in the CNS. We packaged ssAAV:CAG-eGFP in AAV9 and ssAAV:CAG-tdTomato in X1.1, then intravenously delivered them as an AAV cocktail to a neonate rhesus macaque (female *Macaca mulatta*, within 10 days of birth, $5x10^{13}$ vg/kg per macaque, $2.5x10^{13}$ vg/kg per AAV, n=1 per group) (Fig. 6A). After 4 weeks of expression, we observed robust expression of X1.1 across brain regions including cortex, lingual gyrus (LG), hippocampus, and cerebellum, compared to AAV9 (Fig. 6B-C; Supplementary Video. 1). Further IHC staining revealed that ~98% of the cells transduced by X1.1 in the cortex were neurons, while a small proportion of the targeted cells were endothelial or glia cells (Fig. 6D-E). Neuron transduction by X1.1 was ~45-fold higher than AAV9 (Fig. 6F). The difference between the neurotropic profile of X1.1 in neonate macaque and its endothelial cell-tropic profile in rodents both opens up new potential applications and highlights the necessity of profiling AAV vectors across species. These experiments demonstrate that the new capsid AAV-X1.1 can efficiently transduce the CNS in infant Old World monkeys, making it a potentially useful vector for research of neurological disorders.

3.11 DISCUSSION

In this study, we describe a family of novel vectors including AAV-X1 and AAV-X1.1, which specifically and efficiently transduces mouse brain endothelial cells with a ubiquitous promoter following systemic administration. This level of specificity in the mouse CNS is unprecedented among both natural and previously-engineered AAV serotypes. The previously-engineered AAV vector PHP.eB (Chan et al., 2017) has been widely used for targeting most cell types in mice CNS, while the more recently-engineered vector PHP.V1 (Ravindra Kumar et al., 2020) has been shown to have increased potency for, but not selective targeting of, brain endothelial cells. However, the enhanced CNS tropism of both vectors is absent in a subset of mouse strains, including BALB/cJ. Here we show that, similar to PHP.eB, PHP.V1 relies on Ly6a, while AAV-X1 vectors are Ly6a-independent and efficiently target brain endothelial cells across mouse strains. This Ly6a independence suggests that these novel vectors may utilize a novel receptor for CNS targeting and adds to the vectors' translational promise, as Ly6a is a murine-specific factor.

A major challenge in achieving successful gene therapy is the presence of neutralizing antibodies against AAVs. The neutralizing antibodies induced by an initial AAV delivery have been reported to persist long after the treatment, which could prevent the successful repeated administration needed for maintaining transgene expression (Hamilton and Wright, 2021). Serotype switching between administrations could be a potential solution for dealing with neutralizing antibodies against the initially-administered serotype. We successfully transferred the 7-mer X1 peptide from AAV9 to AAV1, yielding AAV1-X1, which transduces brain endothelial cells efficiently following IV delivery. This result shows that the X1 peptide is more modular than the 7-mer peptide of PHP.B (Martino et al., 2021). Administering AAV1-X1 packaging Ly6a, we successfully made CBA/J mice more permissive for PHP.eB, thus both demonstrating the novel vector's ability to introduce a functional receptor and verifying that serotype switching may be a potential solution for sequential AAV administration (Rivière, Danos, and Douar, 2006; Majowicz et al., 2017). The transferability of the AAV9-based X1's 7-mer peptide to AAV1 and AAV-DJ highlights a general strategy that could be applied to other engineered AAVs, although the previous failure of the transfer of PHP.B's CNS-tropic phenotype along with its peptide to AAV1 (Tan et al., 2019; Lau et al., 2019; Martino et al., 2021; Pietersz et al., 2021) cautions that the success of this strategy could vary case by case (Supplementary Table 1). Engineered AAVs in diverse serotype backbones could not only help with applications involving repeated administration but also circumvent pre-existing neutralizing antibodies to a certain AAV serotype.

Delivering therapeutic agents, or genetic material encoding therapeutics, across the BBB to treat neurological diseases of the CNS remains a challenging task (Stanimirovic, Sandhu, and Costain, 2018; Terstappen et al., 2021). Many enzymes, however, are secreted and can exert cross-correction effects. For these, we could instead deliver the genetic material to brain endothelial cells, transforming these cells into a biofactory to produce and distribute therapeutics to other cell types. The novel endothelial cell-tropic vector we describe here provided us with a unique chance to explore this concept in an animal model. We used the X1.1 vector to induce Sparcl1/Hevin protein production in brain endothelial cells and observed that this rescued the thalamocortical synapse loss phenotype of Hevin KO mice. This proof-of-concept supports the brain endothelial cell biofactory model for production of enzymes, antibodies, or other biological therapeutics, suggesting a novel therapeutic approach for diseases like lysosomal storage disorders.

Previous systemic AAVs for the CNS that were engineered in mice have not always translated to NHPs (Hordeaux et al., 2018; Matsuzaki et al., 2018). Tropism of previously-reported endothelial variants such as BR1 or BI30 (Körbelin et al., 2016; Krolak et al., 2022) remained unexplored in non-human primate. Given the X1 vectors' independence of Ly6a, we tested the novel vectors in various NHP species. We initially tested X1.1 in marmoset, a New World monkey, but did not observe an obvious difference in targeting the CNS compared to AAV9 following systemic delivery. We then turned to the macaque, an Old World monkey, which is more similar genetically to humans and is widely used in research, including gene therapy (Jennings et al., 2016; Hudry and Vandenberghe, 2019; Bey et al., 2020). We first tested the virus on *ex vivo* brain slices from the rhesus macaque (*Macaca mulatta*) and southern pig-tailed macaque (*Macaca nemestrina*). We observed greater increases in DNA, RNA, and protein with X1.1 than other CNS vectors including PHP.eB (Chan et al., 2017), CAP-B10, and CAP-B22 (Goertsen et al., 2021). We then intravenously injected X1.1 in the rhesus macaque and observed a significant improvement in targeting the CNS compared to AAV9. Interestingly, the rodent-endothelial-tropic X1.1 efficiently transduces neurons in the macaque brain. The conservation of enhanced CNS tropism across rodents and NHPs is encouraging for X1.1's potential in tackling neurological disorders in specific condition. We further showed that our engineered vector X1.1 also has increased efficiency in transducing *ex vivo* adult macaque and human brain slices compared to other previously-engineered CNS vectors. Further experiments would be needed to examine the novel vectors' translation potential in adult primates.

The exact mechanism behind the distinction in cell-type tropism of X1.1 across models tested remains unknown. The different ages of animals tested, the difference in BBB maturation and the different route of administration would also need to be taken into consideration for this distinction (Supplementary Table 2). In rodents with a healthy BBB, X1 vectors seem to prefer endocytosis to transcytosis at the BBB, either due to their interactions with novel receptors or the vector's own physiological features. In pericyte-deficient mice where endothelial transcytosis is increased and endothelial cells show occasional hot-spot leakage areas due to altered endothelial cell-cell interaction (Armulik et al., 2010; Mäe et al., 2021), we observed increasing transduction of astrocytes and neurons. In rhesus macaque, X1.1 seems biased towards transcytosis at the BBB and transduces neurons efficiently after crossing the BBB. This distinction in tropism opens up the potential for different applications with X1.1 in endothelial cells and neurons in different species. It also emphasizes the need to test AAV variants across species to capture their complete profile.

In summary, here we describe new systemic AAV tools to expand our understanding of the neurovascular unit across species. The novel vector X1 and its further-engineered family of variants, including X1.1, provide genetic access to brain endothelial cells in mice with unprecedented potency and specificity, and their efficient targeting of the CNS in NHP and human brain slices offers hope of accelerating translational research. The surprising modularity of the X1 variant peptide may allow researchers to apply immunogenically-distinct AAVs at multiple timepoints, and the demonstrated application of the X1 vectors to transform brain endothelial cells into a secretory biofactory validates a novel method to deliver therapeutic agents to the CNS.

3.12 FIGURES

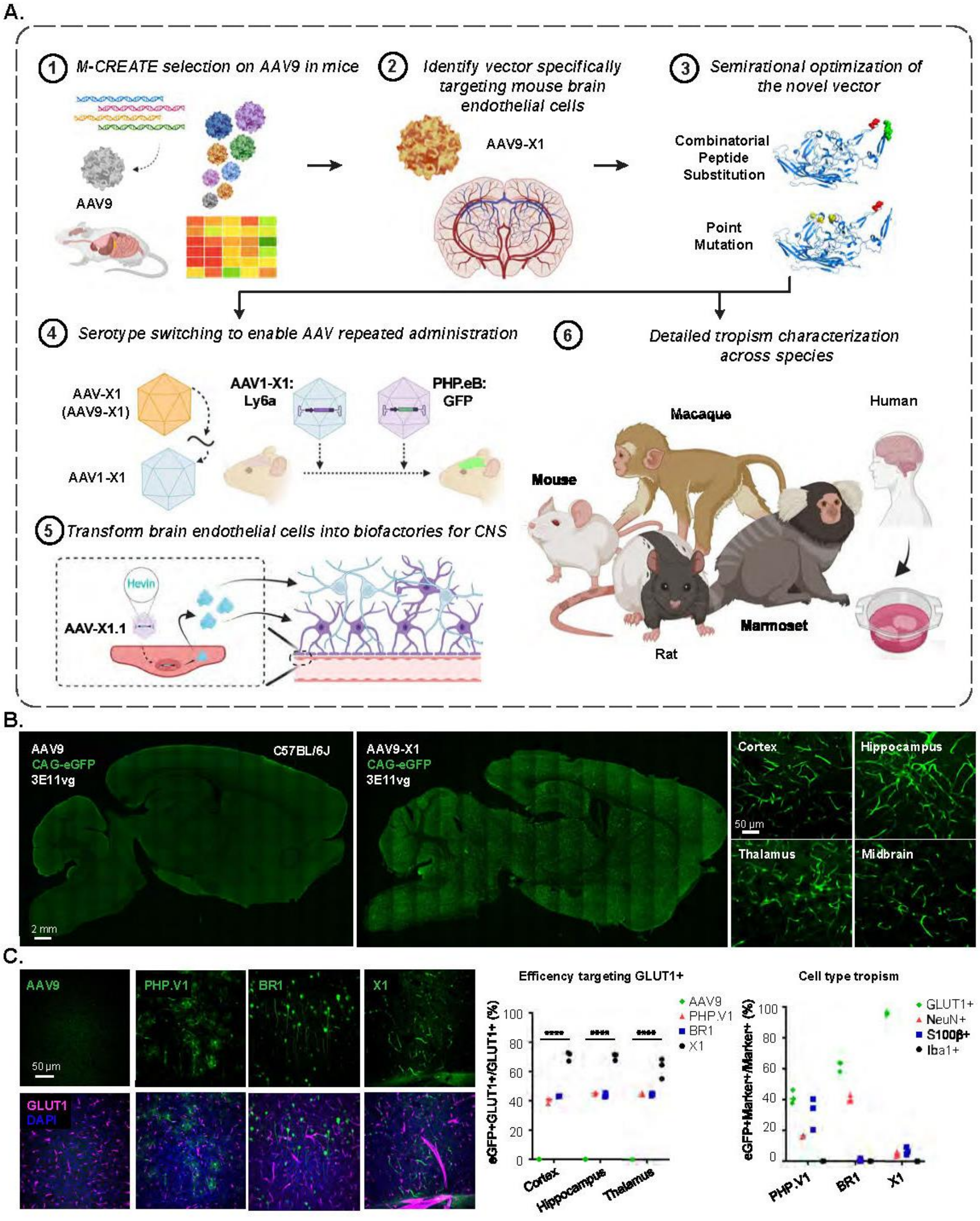

Figure 1: Engineered AAVs can specifically target the brain endothelial cells in mouse following systemic delivery.

A. An overview of the engineering and characterization of the novel capsids. (1), (2): Evolution of AAV9 using Multiplexed-CREATE and identification of a novel vector, AAV-X1, that transduces brain endothelial cells specifically and efficiently following systemic administration in mice. (3): Combinatorial peptide substitution and point mutation to further refine the novel vector's tropism, yielding improved vectors. (4): Transferring the X1 peptide to the AAV1 backbone to enable serotype switching for sequential AAV administration. (5): Utilizing AAV-X1 to transform the brain endothelial cells into a biofactory, producing Hevin for the CNS. (6): Validation of the novel AAVs across rodent models (genetically diverse mice strains and rats), NHPs (marmosets and macaques), and *ex vivo* human brain slices. **B.** (Left) Representative images of AAV (AAV9, AAV-X1) vector-mediated expression of eGFP (green) in the brain (scale bar: 2 mm). (Right) Zoomed-in images of AAV-X1-mediated expression of eGFP (green) across brain regions including the cortex, hippocampus, thalamus, and midbrain (scale bar: 50 µm). (C57BL/6J, n=3 per group, 3E11 vg IV dose per mouse, 3 weeks of expression). **C.** (Left) Representative images of AAV (AAV9, PHP.V1, BR1, AAV-X1) vector-mediated expression of eGFP (green) in the cortex. Tissues were co-stained with GLUT1 (magenta) (scale bar: 50 µm). (Middle) Percentage of AAV-mediated eGFP-expressing cells that overlap with the GLUT1+ marker across brain regions, representing the efficiency of the vectors' targeting of GLUT1+ cells. A two-way ANOVA and Tukey's multiple comparisons tests with adjusted P values are reported (****P<0.0001 for AAV9 versus X11 in cortex, hippocampus, and thalamus). Each data point shows the mean ± s.e.m of 3 slices per mouse. (Right) Percentage of GLUT1+ markers in AAV-mediated eGFP-expressing cells across brain regions, representing the specificity of the vectors' targeting of GLUT1+ cells. (C57BL/6J, n=3 per group, 3E11 vg IV dose per mouse, 3 weeks of expression).

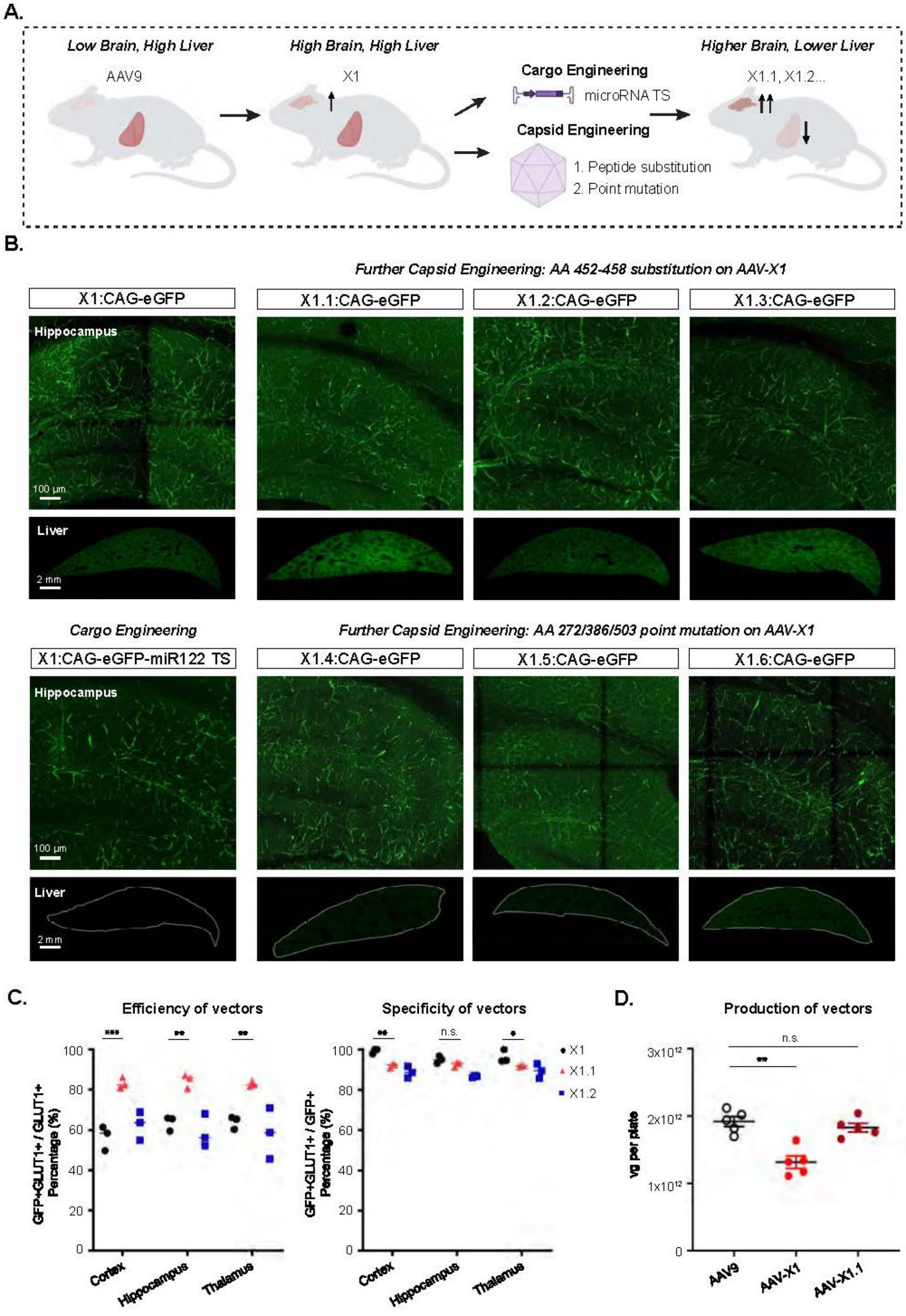

Figure 2: Semi-rational refinement of X1 capsid's tropism by further cargo and capsid engineering.

A. Illustration demonstrating cargo and capsid engineering to refine X1's tropism to increase brain targeting and lower liver targeting. **B.** Representative images of novel vector-mediated expression of eGFP (green) in hippocampus and liver. Images are matched in fluorescence intensity to the X1: CAG-eGFP image. Brain scale bar: 100 µm. Liver scale bar: 2mm. (n≥4 per group, ~8 week-old C57BL/6J males, 3x10^{11} vg IV dose per mouse, 3 weeks of expression). (Top left) X1-mediated expression of CAG-eGFP. (Bottom left) X1-mediated eGFP expression with cargo engineering by incorporating MicroRNA-122 target sites (miR-122TS) in the CAG-eGFP genome. (Top right) Further capsid engineering by substitution at AA 452-458 of AAV-X1 yielding X1.1, X1.2 and X1.3. Vector-mediated expression of eGFP is shown. (Bottom right) Further capsid engineering on AAV-X1 by mutating AA272/AA386/AA503 to alanine to yield X1.4, X1.6, and X1.5, respectively. Vector-mediated expression of eGFP is shown. **C.** (Left) Percentage of AAV-mediated eGFP-expressing cells that overlap with GLUT1+ markers across brain regions, representing the efficiency of the vectors' targeting of GLUT1+ cells. A two-way ANOVA and Tukey's multiple comparisons tests with adjusted P values are reported (P=0.0002 for X1 versus X1.1 in the cortex, P=0.0022 for X1 versus X1.1 in the hippocampus, P=0.0049 for X1 versus X1.1 in the thalamus; *P ≤ 0.05, **P ≤ 0.01 and ***P ≤ 0.001 are shown, P > 0.05 is not shown). Each data point shows the mean ± s.e.m of 3 slices per mouse. (Right) Percentage of GLUT1+ markers in AAV-mediated eGFP-expressing cells across brain regions, representing the specificity of the vectors' targeting of GLUT1+ cells. A two-way ANOVA and Tukey's multiple comparisons tests with adjusted P values are reported (P=0.0013 for X1 versus X1.1 in the cortex, P=0.3854 for X1 versus X1.1 in the hippocampus, P=0.0413 for X1 versus X1.1 in the thalamus; *P ≤ 0.05, **P ≤ 0.01, ***P ≤ 0.001, n.s. P > 0.05). Each data point shows the mean ± s.e.m of 3 slices per mouse. **D.** AAV vector yields from an established laboratory protocol (see Methods). One-way analysis of variance (ANOVA) non-parametric Kruskal-Wallis test (approximate P=0.0014), and follow-up multiple comparisons with uncorrected Dunn's test are reported (P=0.0099 for AAV9 versus AAV-X1, P>0.9999 for AAV9 versus AAV-X1.1; n≥4 per group, each data point is the mean of 3 technical replicates, mean ± s.e.m is plotted). **P ≤ 0.01, n.s. P > 0.05.

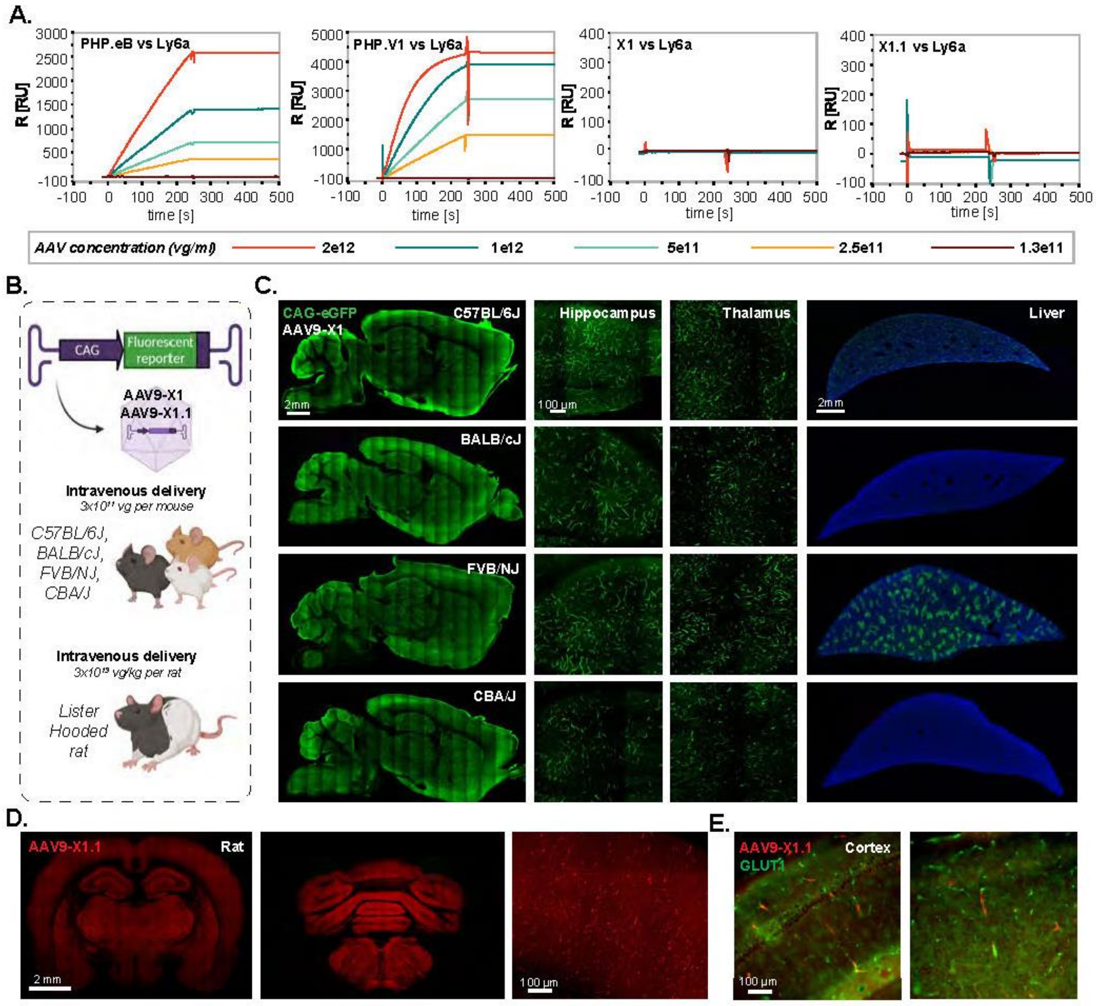

Figure 3: AAV9-X1 and AAV9-X1.1 efficiently transduce brain endothelial cells across diverse mice strains and rats.

A. Surface plasmon resonance (SPR) plots of PHP.eB, PHP.V1, AAV-X1, and AAV-X1.1 binding to surface-immobilized Ly6a-Fc protein captured on a protein A chip. Colored lines show binding response for each vector across a range of vector concentrations. **B.** Illustration demonstrating the IV administration of AAV-X1 capsid packaged with ssAAV:CAG-eGFP genome in genetically diverse mice strains (~8 week-old young C57BL/6J, BALB/cJ, FVB/NJ and CBA/J, 3E11 vg per mouse) and IV administration of AAV-X1.1 capsid packaged with ssAAV:CAG-tdTomato genome in Lister Hooded rats (adult, 3E13 vg per rat). **C.** Representative brain and liver images of AAV-X1-mediated eGFP expression (green) in C57BL/6J, BALB/cJ, FVB/NJ and CBA/J mice with zoomed-in images of hippocampus and thalamus. Sagittal brain section scale bar: 2mm. Hippocampus and thalamus scale bar: 100 µm. Liver scale bar: 2mm. **D.** Representative images of forebrain and hindbrain of AAV-X1.1-mediated tdTomato expression (red) in Lister Hooded rat. Scale bar: 2 mm, zoom-in image scale bar: 100 µm. **E.** Representative images of cortex of AAV-X1.1-mediated tdTomato expression (red) in Lister Hooded rat, tissue were co-stained with GLUT1 (green).

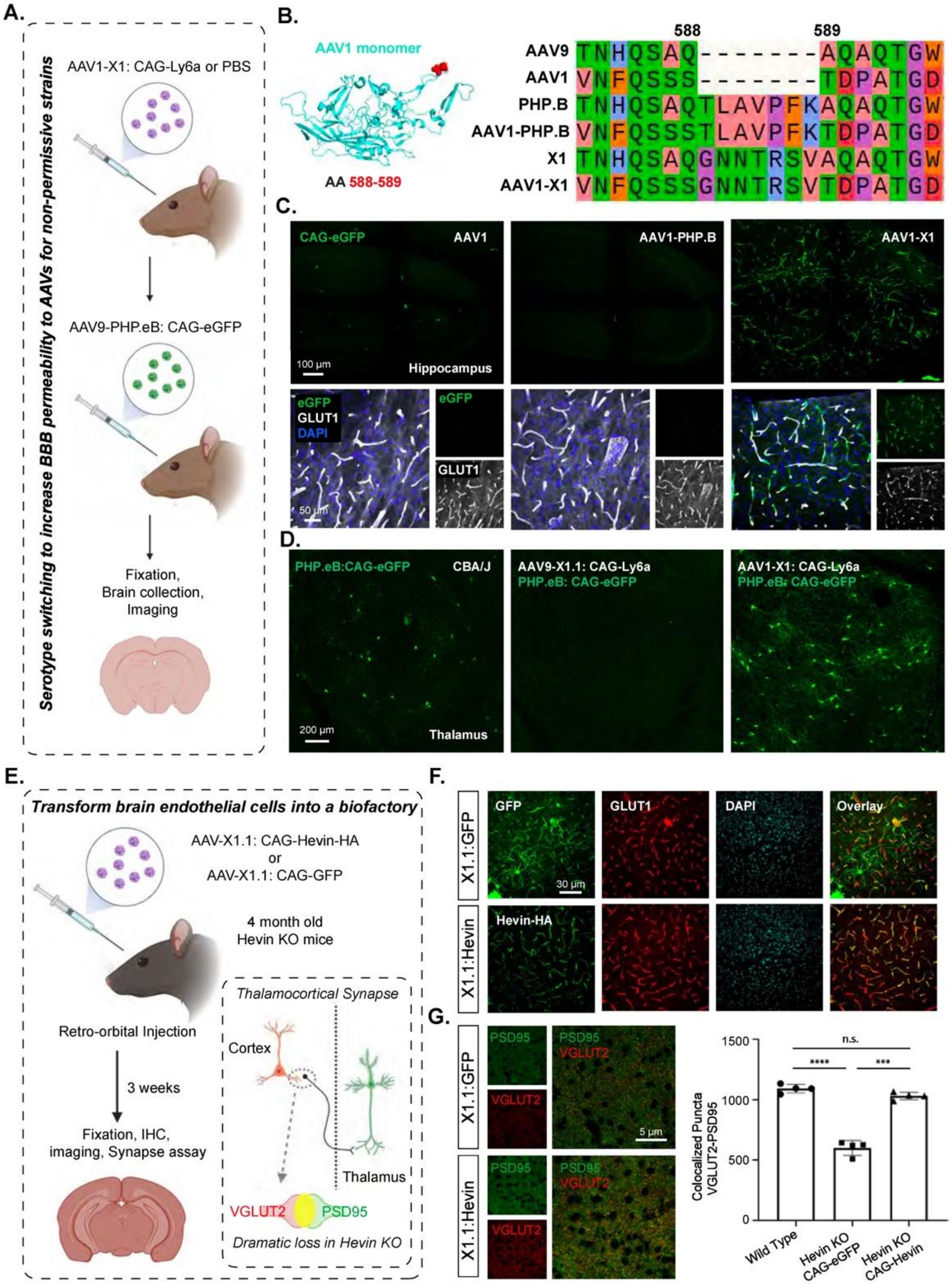

Figure 4: X1 capsids can enable AAV repeated administration with serotype switching and can transform the BBB into a biofactory.

A. Illustration of utilizing serotype switching to increase BBB permeability for AAVs in non-permissive strains. IV administration of AAV1-X1 capsid packaged with ssAAV: CAG-Ly6a or PBS in CBA/J mice (~8-week-old young adults, $3x10^{11}$ vg IV dose/mouse, n=4). After 3 weeks, AAV9-PHP.eB packaged with CAG-eGFP was intravenously administered into CBA/J mice. 3 weeks after the second injection, the brain was collected and imaged. **B.** (Left) Illustration of AAV1 monomer structure with the position of the 7-mer insertion, AA 588/589, highlighted (red). (Right) Sequences of AAV9, AAV1, PHP.B, AAV1-PHP.B, X1 and AAV1-X1 around the insertion site are shown, colored based on physicochemical properties (Zappo). **C.** (Top) Representative images of AAV1, AAV1-PHP.B and AAV-X1-mediated eGFP expression in the hippocampus (scale bar: 100 µm). (Bottom) Zoomed-in images of tissues co-stained with GLUT1 (white) and DAPI (blue). **D.** (Left) Representative image of PHP.eB-mediated eGFP expression in the brain of CAB/J mice (scale bar: 200 µm). (Right) Representative images of the brains of CAB/J mice following sequential administration of either AAV9-X1.1: CAG-Ly6a or AAV1-X1: CAG-Ly6a followed by PHP.eB:CAG-eGFP. **E.** Illustration of transforming brain endothelial cells into a biofactory. IV administration of AAV-X1.1 capsid packaged with ssAAV:CAG-Hevin-HA or ssAAV:CAG-eGFP genome in Hevin-KO mice (~4-month-old young adults, $1x10^{12}$ vg IV dose/mouse, n=4). Three weeks post-expression, the mice were anesthetized and perfused and fixation and IHC were performed on the brains. (Bottom right) Illustration of the thalamocortical synapses identified by co-localization of VGLUT2 and PSD95 staining. Thalamocortical synapses are lost in Hevin-KO mice. **F.** (Top) Representative images of AAV-X1.1 vector-mediated expression of eGFP (green) in the brain. The tissues were co-stained with either GLUT1 (red) or DAPI (blue) markers (scale bars: 30 µm). (Bottom) Representative images of AAV-X1.1 vector-mediated expression of Hevin in the brain. The tissues were co-stained with HA (green), GLUT1 (red) and DAPI (blue) markers (scale bar: 30 µm). **G.** (Left) Representative images of a cortical slice stained for PSD95 (green) and VGLUT2 (red) (scale bar: 5 µm). (Right) Quantification of colocalized puncta of VGLUT2 and PSD95 in mice administered X1.1: CAG-eGFP and X1.1: CAG-Hevin-HA. One-way analysis of variance (ANOVA) Brown-Forsythe test (****$P<0.0001$ for WT versus Hevin KO: CAG-eGFP, ***$P=0.0006$ for Hevin KO: CAG-eGFP versus Hevin KO: CAG-Hevin, n.s. P=0.1156 for WT versus Hevin KO: CAG-Hevin; n=4 per group, each data point is the mean of 15 slices for one animal, mean ± s.e.m is plotted).

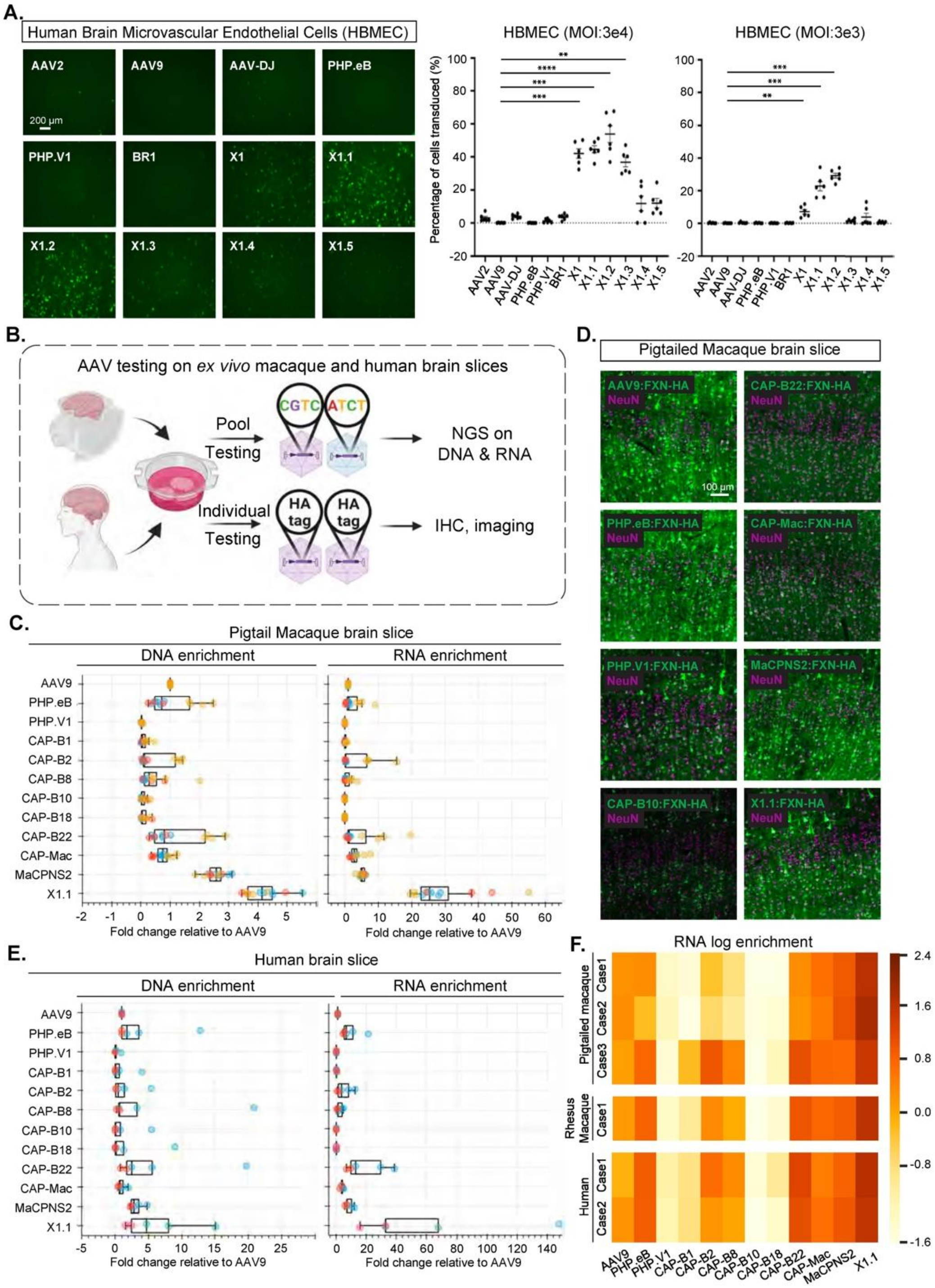

Figure 5: Engineered AAVs can efficiently transduce cultured human brain microvascular endothelial cells, *ex vivo* macaque and human brain slices.

A. (Left) Representative images of AAV (AAV2, AAV9, AAV-DJ, PHP.eB, PHP.V1, BR1, X1, X1.1, X1.2, X1.3, X1.4, X1.5)-mediated eGFP expression (green) in Human Brain Microvascular Endothelial Cells (HBMECs). (AAVs packaged with ssAAV:CAG-eGFP, n= 6 per condition, 1 day expression). (Right) Percentage of cells transduced by the AAVs. In the condition of MOI:3E4, one-way analysis of variance (ANOVA) non-parametric Kruskal-Wallis test (approximate $P<0.0001$), and follow-up multiple comparisons with uncorrected Dunn's test are reported ($P=0.0004$ for AAV9 versus AAV-X1, $P=0.0002$ for AAV9 versus AAV-X1.1, $P<0.0001$ for AAV9 versus AAV-X1.2, $P=0.002$ for AAV9 versus AAV-X1.3; n=6 per group, each data point is the mean of 3 technical replicates, mean ± s.e.m is plotted). In the condition of MOI:3E3, one-way analysis of variance (ANOVA) non-parametric Kruskal-Wallis test (approximate $P<0.0001$), and follow-up multiple comparisons with uncorrected Dunn's test are reported ($P=0.0082$ for AAV9 versus AAV-X1, $P=0.0004$ for AAV9 versus AAV-X1.1, $P=0.0001$ for AAV9 versus AAV-X1.2; n=6 per group, each data point is the mean of 3 technical replicates, mean ± s.e.m is plotted). $^{**}P \leq 0.01$, $^{***}P \leq 0.001$, $^{****}P \leq 0.0001$ are shown, $P > 0.05$ is not shown. **B.** Illustration of AAV testing in *ex vivo* macaque and human brain slices. The brain slices were freshly extracted from southern pig-tailed macaque brain, rhesus macaque brain, and human brain. The slices were cultured at physiological conditions *ex vivo*. In the pool testing pipeline (top), a pool of AAVs packaged with CAG-FXN-HA genome containing a unique barcode was applied to the slice, and DNA extraction and RNA extraction were performed after 7 days. Next-generation sequencing (NGS) was performed to determine the proportion of each barcode (AAV) in DNA and RNA. In the individual testing pipeline (bottom), AAVs packaged with CAG-FXN-HA were individually applied to the slices. Fixation, IHC, and imaging were performed on the slices after 7 days. **C.** DNA and RNA level in southern pig-tailed macaque brain slices for AAVs, with DNA and RNA levels normalized to AAV9. **D.** Representative images of AAV-mediated CAG-FXN-HA expression in *ex vivo* southern pig-tailed macaque brain slices. The tissues were co-stained with antibodies against HA (green) and NeuN (magenta). **E.** DNA and RNA level in human brain slices for AAVs, with DNA and RNA levels normalized to AAV9. **F.** RNA log enrichment of AAVs across pigtailed macaque, rhesus macaque and human brain slices.

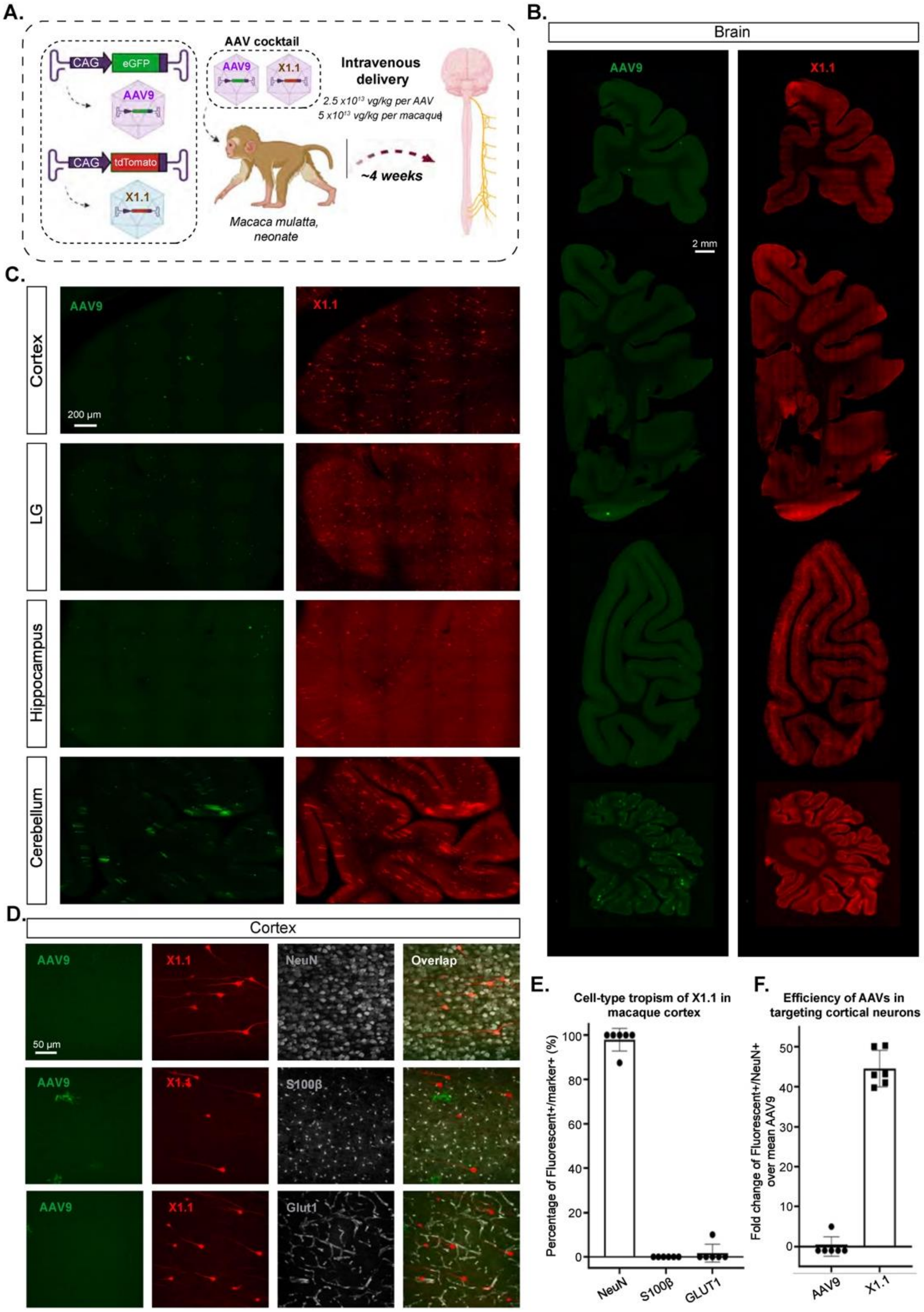

Figure 6: Engineered AAVs can efficiently transduce the central nervous system in rhesus macaque.

A. Illustration of AAV vector delivery to rhesus macaque to study transduction across the CNS and PNS after 3 weeks of expression. The capsids (AAV9/X1.1) and their corresponding genomes (ssAAV:CAG-eGFP/tdTomato) are shown on the left. Two AAVs packaged with different fluorescent proteins were mixed and intravenously injected at a dose of 5×10^{13} vg/kg per macaque (*Macaca mulatta*, injected within 10 days of birth, female, i.e. 2.5×10^{13} vg/kg per AAV). Representative images of macaque **B.**, coronal sections of forebrain, midbrain, hindbrain and cerebellum (scale bar: 2 mm), and **C.**, selected brain areas: cortex, lingual gyrus (LG), hippocampus and cerebellum (scale bar: 200 µm). **D.** Brain tissues were co-stained with NeuN (white) or S100β (white) or GLUT1 (white); representative images of the cortex are shown. **E.** Cell-type tropism of X1.1 in macaque brain, shown by percentage of Fluorescent+/Marker+. Each data point is a slice. **F.** Quantification of the fold change of Fluorescent+/NeuN+ over mean AAV9 in the macaque brain. Each data point is a slice.

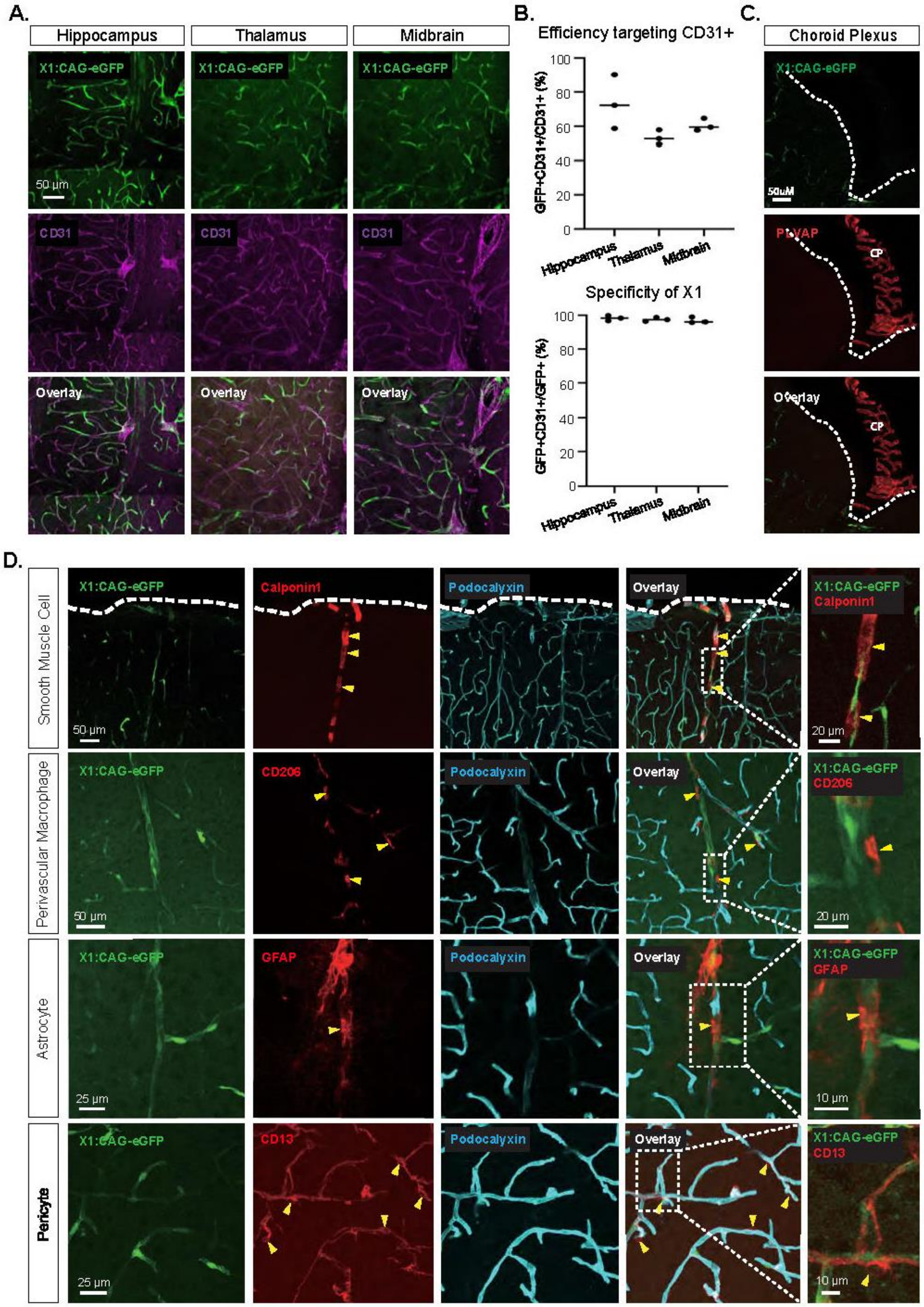

Supplementary Figure 1: Detailed characterization of AAV9-X1 in the mouse brain.

A. Representative images of AAV-X1 vector-mediated expression of eGFP (green) in the brain. The tissues were co-stained with GLUT1 marker (magenta) (scale bar: 50 µm). **B.** (Top) Percentage of AAV-mediated eGFP-expressing cells that overlap with GLUT1+ markers across brain regions, representing the efficiency of the vectors in targeting CD31+ cells. Each data point shows the mean ± s.e.m of 3 slices per mouse. (Bottom) Percentage of CD31+ markers in AAV-mediated eGFP-expressing cells across brain regions, representing the specificity of the vectors in targeting GLUT1+ cells. (n≥4 per group, ~8 weeks old C57BL/6J males, 3x10^{11} vg IV dose per mouse, 3 weeks of expression). **C-D.** EGFP expression is seen only in endothelial cells possessing BBB characteristics, and not in other vascular cells. **C.** PLVAP (red)-positive endothelial cells in choroid plexus (CP) do not express eGFP. The ventricular border is indicated by the dashed line. **D.** Representative images of brain sections co-stained with endothelial cell marker (podocalyxin, in cyan) and (in red, with yellow arrowheads) markers for smooth muscle cells (calponin 1), perivascular macrophages (CD206), astrocytes (GFAP), and pericytes (CD13). The dashed lines indicate the cortical surface.

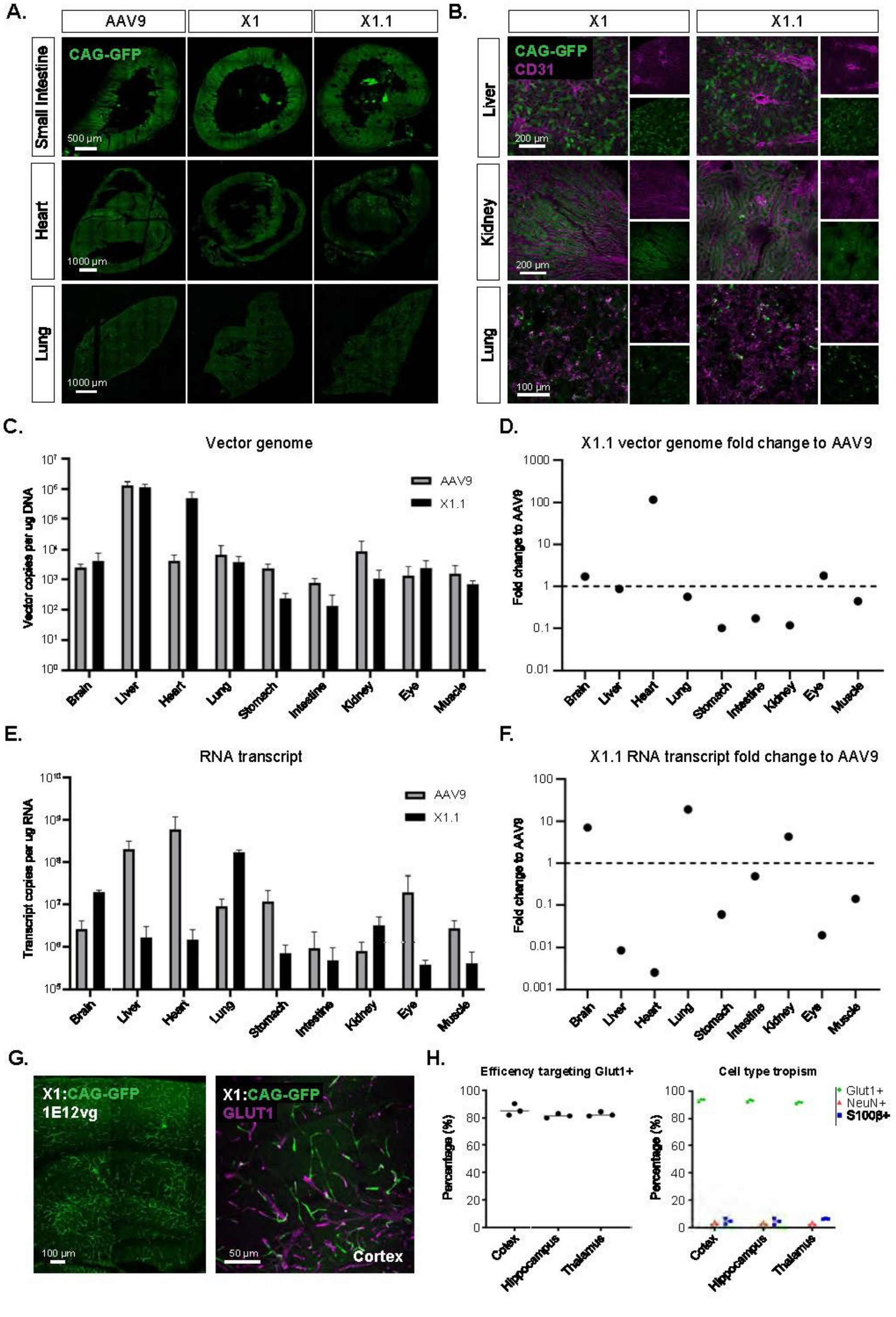

Supplementary Figure 2: Biodistribution of AAVs across mice organs.

A. Representative images of AAV9, AAV-X1, and AAV-X1.1 vector-mediated expression of eGFP in the small intestine (scale bar: 500 µm), heart (scale bar: 1000 µm) and lung (scale bar: 1000 µm) (n≥4 per group, ~8 week-old C57BL/6J males, 3E11 vg IV dose per mouse, 3 weeks of expression). **B.** Representative images of AAV-X1, and AAV-X1.1 vector-mediated expression of eGFP in the liver (scale bar: 500 µm), kidney (scale bar: 1000 µm) and lung (scale bar: 1000 µm) (n≥4 per group, ~8 week-old C57BL/6J males, 3E11 vg IV dose per mouse, 3 weeks of expression). The tissues were co-stained with CD31 (magenta). **C**. Vector genome of AAV9 or AAV-X1 per ug DNA across organs in mice following I.V. delivery (n=3 per group, ~8 week-old C57BL/6J males, 3E11 vg IV dose per mouse, 3 weeks of expression). **D**. Vector genome of AAV-X1 fold change of vector genome of AAV9 across organs. (n=3 per group, ~8 week-old C57BL/6J males, 3E11 vg IV dose per mouse, 3 weeks of expression). **E**. RNA transcript of AAV9 or AAV-X1 per ug RNA across organs in mice following I.V. delivery, GADPH was used to normalize across organs (n=3 per group, ~8 week-old C57BL/6J males, 3E11 vg IV dose per mouse, 3 weeks of expression). F. RNA transcript of AAV-X1 fold change of RNA transcript of AAV9 across organs. (n=3 per group, ~8 week-old C57BL/6J males, 3E11 vg IV dose per mouse, 3 weeks of expression). **G.** AAV-X1 vector-mediated expression of eGFP in the cortex (n=3, ~8 week-old C57BL/6J males, 1E12 vg IV dose per mouse, 3 weeks of expression). The tissues were co-stained with GLUT1 (magenta). Quantification can be seen in **H**. (Left) Percentage of AAV-mediated eGFP-expressing cells that overlap with the GLUT1+ marker across brain regions, representing the efficiency of the vectors' targeting of GLUT1+ cells. (Right) Percentage of marker+ cells in AAV-mediated eGFP-expressing cells across brain regions, representing the specificity of the vectors. Each data point is the average of 3 slices of each mouse. Source data are provided as a Source Data file.

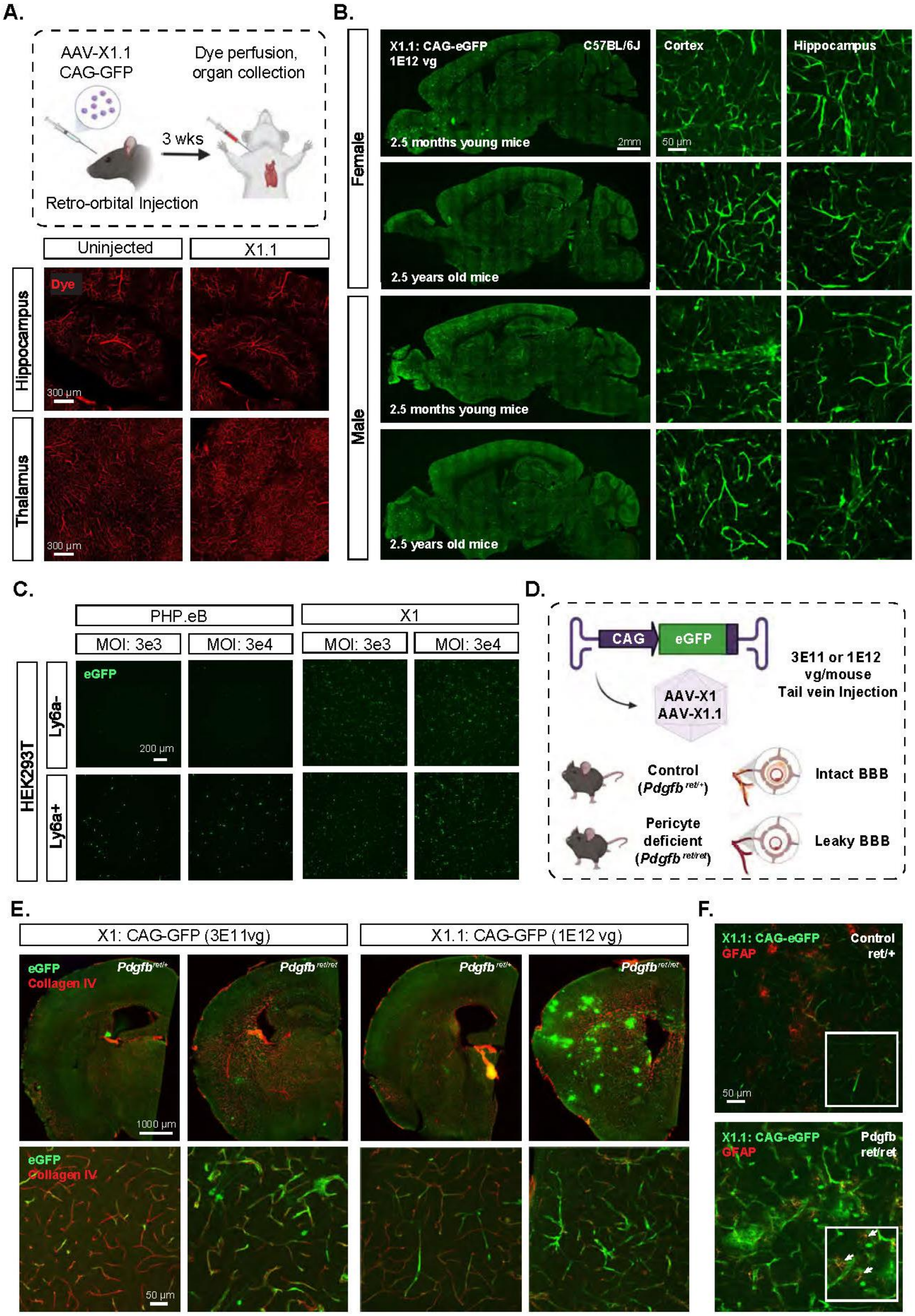
A.
AAV-X1.1
CAG-GFP
Dye perfusion,
organ collection
3 wks
Retro-orbital Injection
Uninjected
X1.1
Hippocampus
Thalamus
Dye
300 µm
300 µm
B.
Female
Male
X1.1: CAG-eGFP
1E12 vg
C57BL/6J
Cortex
Hippocampus
2.5 months young mice
2mm
50 µm
2.5 years old mice
2.5 months young mice
2.5 years old mice
C.
PHP.eB
X1
MOI: 3e3
MOI: 3e4
MOI: 3e3
MOI: 3e4
HEK293T
Ly6a-
Ly6a+
eGFP
200 µm
D.
CAG
eGFP
3E11 or 1E12
vg/mouse
Tail vein Injection
AAV-X1
AAV-X1.1
Control
(*Pdgfb* ret/+)
Intact BBB
Pericyte
deficient
(*Pdgfb* ret/ret)
Leaky BBB
E.
X1: CAG-GFP (3E11vg)
X1.1: CAG-GFP (1E12 vg)
eGFP
Collagen IV
Pdgfb ret/+
Pdgfb ret/ret
Pdgfb ret/+
Pdgfb ret/ret
1000 µm
eGFP
Collagen IV
50 µm
F.
X1.1: CAG-eGFP
GFAP
Control
ret/+
50 µm
X1.1: CAG-eGFP
GFAP
Pdgfb
ret/ret

Supplementary Figure 3：Engineered AAVs are independent of Ly6a and show different expression patterns in pericyte-deficient mice.

A. (Top) Illustration of dye perfusion to evaluate the intactness of the BBB in AAV-injected mice. (Bottom) Representative images of dye staining (red) in hippocampus and thalamus (scale bars: 300 μm) (n=3 per group, 1E12 vg IV dose per mouse, 3 weeks of expression). **B.** Representative image of AAV-X1 vector-mediated expression of eGFP in the brains of both sexes and both young 2.5-month-old and aged 2.5-year-old C57BL/6J males (scale bars: 2 mm in whole brain and 50 μm in cortex/hippocampus) (n=3 per group, 1E12 vg IV dose per mouse, 3 weeks of expression). **C.** Representative images of AAV transduction in HEK293T cells with or without previous transfection of plasmids encoding Ly6a. (Packaged with ssAAV:CAG-eGFP, n= 3 per condition, 2-day expression, high dose: MOI 25000, low dose: MOI 2500). Scale bar: 200 µm. **D.** Illustration of AAV vector delivery to control mice and pericyte-deficient mice (Pdgfb ret/ret) for studying their transduction profile in BBB in different conditions (3E11 vg/mouse for X1, 1E12 vg/mouse for X1.1, tail vein injection, 3 weeks' expression). **E.** Representative images of AAV-mediated expression of eGFP (green) in coronal sections of mouse brain (scale bar: 1000 µm), and zoomed-in images of tissue co-stained with collagen IV marker (red) (scale bar: 2 mm). **F.** Representative images of tissue co-stained with GFAP marker (red) (scale bar: 50 µm). Boxes show further zoomed-in views of astrocytes that have endfeet on the vasculature; white arrows highlight the colocalization of eGFP expression and GFAP marker in Pdgfb ret/ret mice.

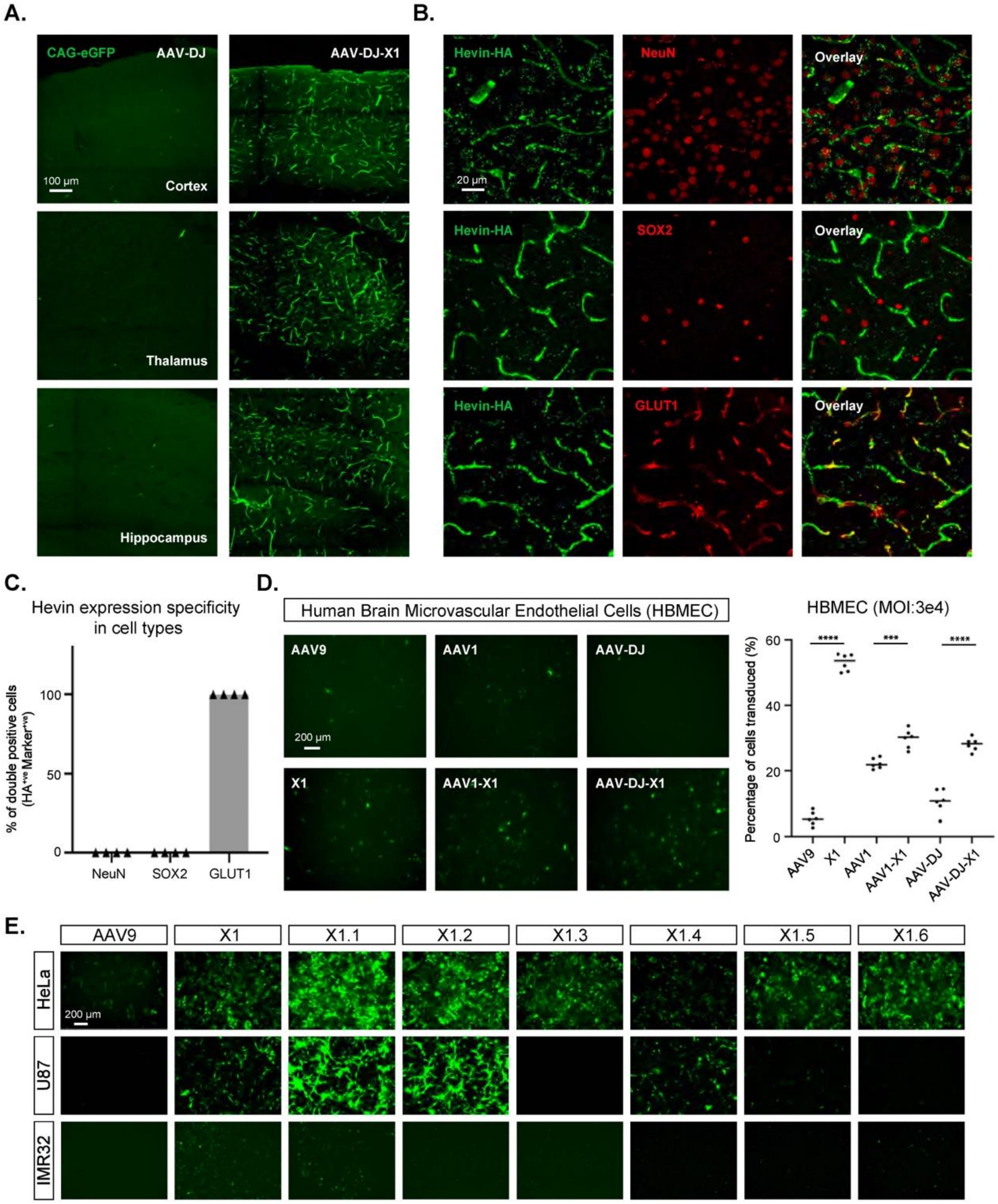

Supplementary Figure 4: Hevin specificity amd engineered AAVs efficiently transduce human cells.

A. Representative images of AAV-DJ and AAV-DJ-X1-mediated eGFP expression in the cortex, thalamus and hippocampus (scale bar: 100 µm) (C57BL/6J, n=3 per group, 3E11 vg IV dose per mouse, 3 weeks of expression). **B**. Representative images of AAV-X1.1 vector-mediated expression of Hevin in the brain. The tissues were co-stained with HA (green) and NeuN (red) or SOX2 (red) or GLUT1 (red) (scale bar: 30 µm). **C**. Quantification of AAV-X1.1-mediated Hevin expression across cell types. **D**. (Left) Representative images of AAV (AAV9, X1, AAV1, AAV1-X1, AAV-DJ, AAV-DJ-X1)-mediated eGFP expression (green) in Human Brain Microvascular Endothelial Cells (HBMECs). (AAVs packaged with ssAAV:CAG-eGFP, n= 6 per condition, 1 day expression). (Right) Percentage of cells transduced by the AAVs, one-way analysis of variance (ANOVA) non-parametric Kruskal-Wallis test (approximate $P<0.0001$), and follow-up multiple comparisons with uncorrected Dunn's test are reported ($P<0.0001$ for AAV9 versus X1, $P=0.0002$ for AAV1 versus AAV1-X1, $P<0.0001$ for AAV-DJ versus AAV-DJ-X1; n=6 per group, each data point is the mean of 3 technical replicates, mean ± s.e.m is plotted). **E.** Representative images of AAV (AAV9, X1, X1.1, X1.2, X1.3, X1.4, X1.5, X1.6)-mediated eGFP expression (green) in HeLa cells, U87 cells, and IMR32 cells (AAVs packaged with ssAAV:CAG-eGFP, n= 3 per condition, 1 day expression, MOI: 50000).

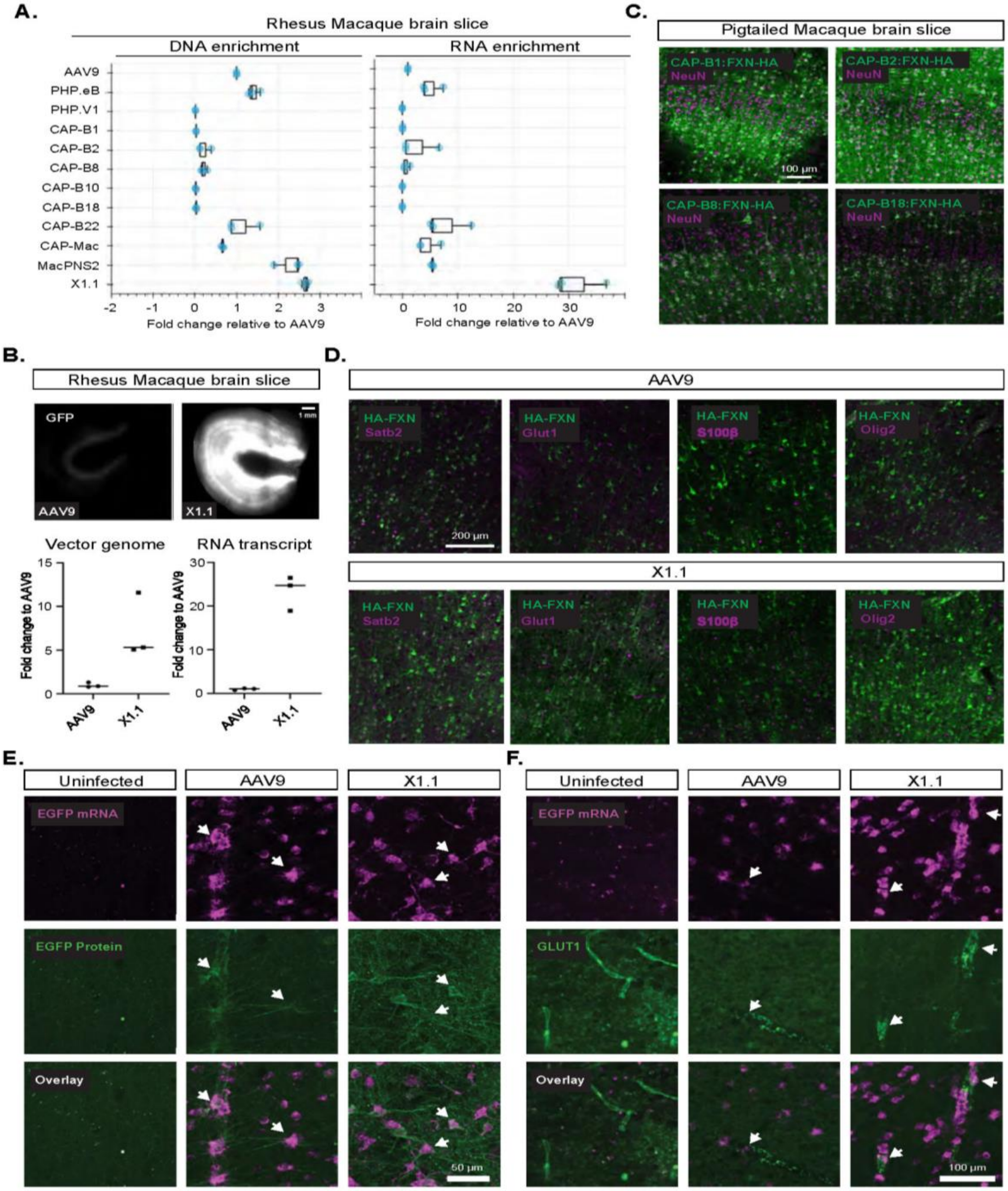

Supplementary Figure 5: Engineered AAVs efficiently transduce human cell lines and *ex vivo* macaque slices.

A. DNA and RNA level in rhesus macaque brain slices for AAVs, with DNA and RNA levels normalized to AAV9. **B.** (top) Representative images of AAV9 and X1.1-mediated

CAG-GFP expression in *ex vivo* rhesus macaque brain slices. (bottom) Vector genome and RNA transcript of the AAVs in the slices, fold change to AAV9 was shown. **C.** Representative images of AAV (CAP-B1, CAP-B2, CAP-B8, CAP-B18)-mediated CAG-FXN-HA expression in *ex vivo* southern pig-tailed macaque brain slices. The tissues were co-stained with antibodies against HA (green) and NeuN (magenta). **D.** Representative images of AAV9 and X1.1-mediated CAG-FXN-HA expression in *ex vivo* southern pig-tailed macaque brain slices. The tissues were co-stained with antibodies against HA (green) and Satb2, GLUT1, S100β or Olig2 (magenta). **E, F.** mFISH analysis of EGFP expression in transduced cultured slices. Organotypic cortical slices were cultured from macaque brain, and were uninfected or infected by X1.1 or AAV9 encapsidated EGFP reporter vector. After eight days in culture, EGFP mRNA was resolved against EGFP protein (E) or GLUT-1 protein (F) in cortical white matter regions. Minimal background EGFP mRNA or protein was detected in the absence of virus (uninfected), EGFP mRNA positive cells often express EGFP protein (arrows, E), and EGFP mRNA positive cells are often found lining GLUT-1+ blood vessels (putative endothelial cells, or pericytes, arrows, F). Images are from stitched montages.

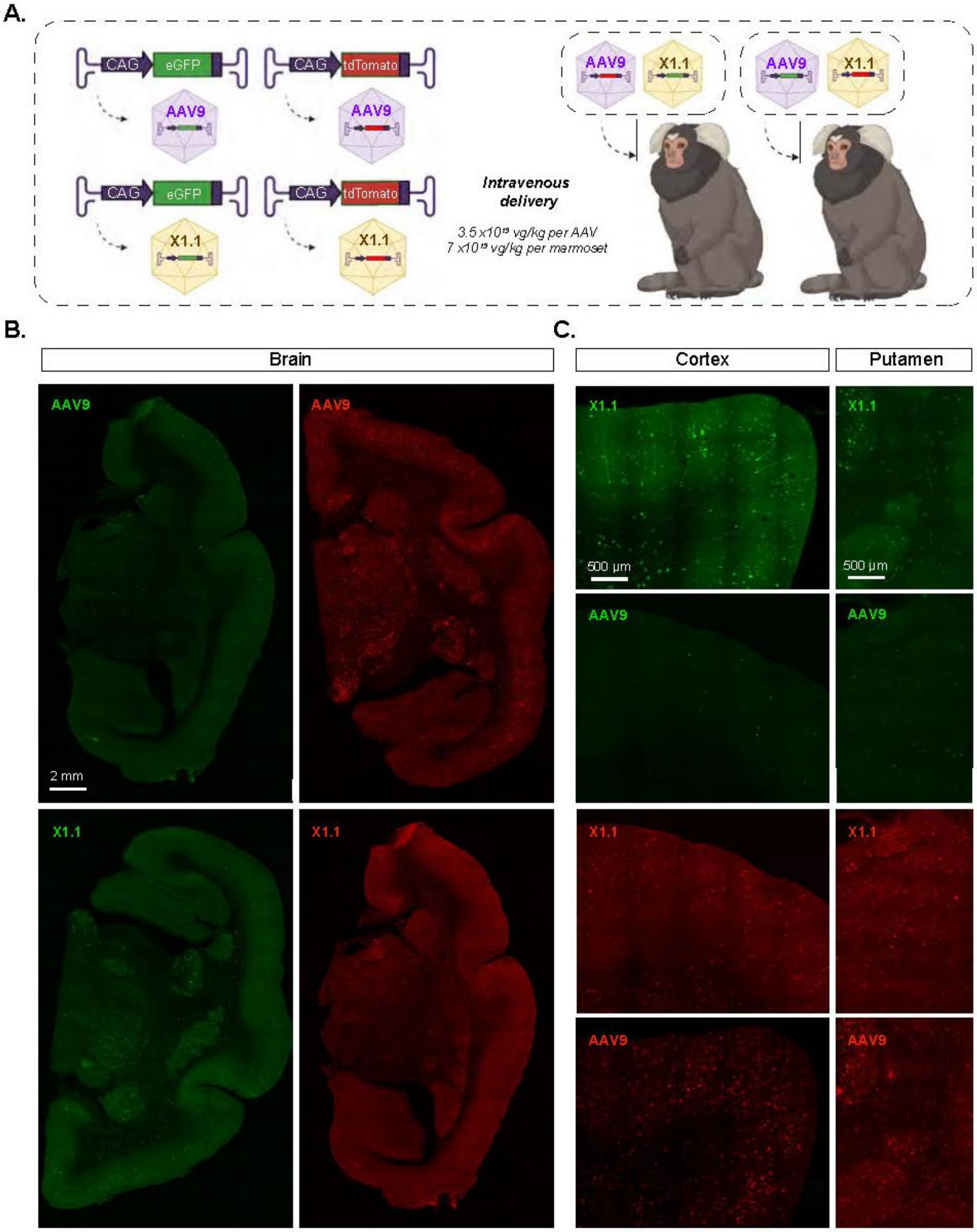

Supplementary Figure 6: Engineered AAV transduces the central nervous system in marmoset similarly to AAV9.

A. Illustration of AAV vector delivery to adult marmoset to study transduction across the CNS after 3 weeks of expression. The capsids (AAV9/X1.1) and their corresponding genomes (ssAAV:CAG-eGFP/tdTomato) are shown on the left. Two AAV vectors packaged with different colored fluorescent reporters were mixed and intravenously delivered at a total dose of 7x10^{13} vg/kg per adult marmoset (16 month-old *Callithrix jacchus*, i.e. 3.5x10^{13} vg/kg per AAV). Representative images of **B.**, coronal brain sections of the midbrain (scale bar: 2 mm), and **C.**, select brain areas: cortex and putamen (scale bar: 500 µm), showing AAV9 vector-mediated expression of eGFP (green) or tdTomato (red), X1.1-mediated expression of eGFP (green) and X1.1-mediated expression of tdTomato (red).

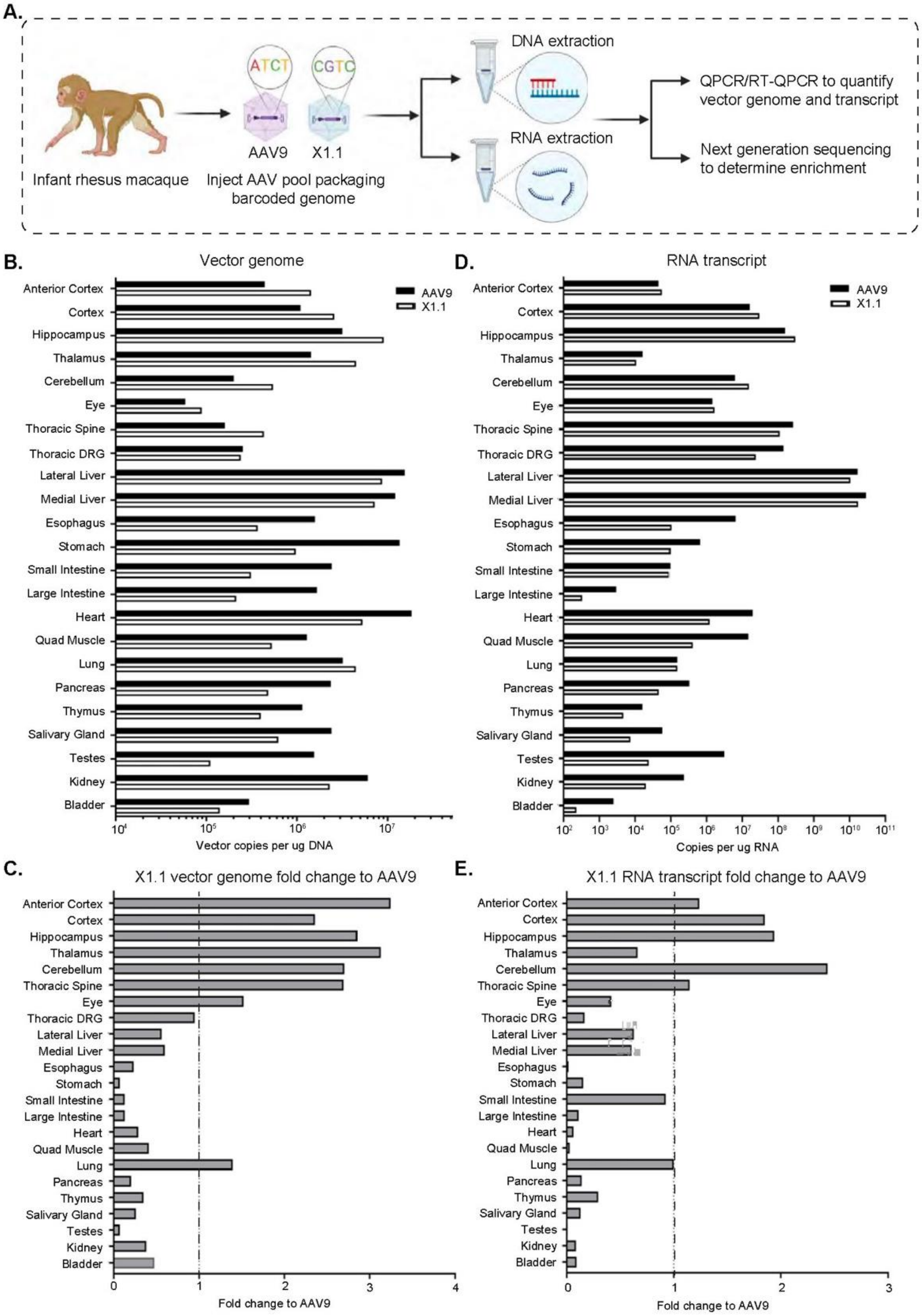

Supplementary Figure 7: Biodistribution of engineered AAV in rhesus macaque following systemic delivery.

A. Illustration of AAV vector delivery to rhesus macaque to study biodistribution after 4 weeks of expression. The capsids (AAV9/X1.1) packaged with CAG-GFP genome containing a unique barcode were mixed and intravenously injected at a dose of 2x10^{13} vg/kg per macaque (*Macaca mulatta*, injected within 10 days of birth, male, i.e. 2x10^{13} vg/kg per AAV). After 4 weeks of expression, tissues were collected and DNA/RNA extractions were performed. Then QPCR/RT-QPCR were performed to quantify vector genome and transcript. Next generation sequencing was performed to determine enrichment. **B.** Vector genome of AAV9 or AAV-X1 per ug DNA across organs in rhesus macaque following IV delivery. **C**. Vector genome of AAV-X1 fold change of vector genome of AAV9 across organs in rhesus macaque. **D**. RNA transcript of AAV9 or AAV-X1 per ug RNA across organs in rhesus macaque following I.V. delivery, GADPH was used to normalize across organs. **E**. RNA transcript of AAV-X1 fold change of RNA transcript of AAV9 across organs. (n=3 per group, ~8 week-old C57BL/6J males, 3E11 vg IV dose per mouse, 3 weeks of expression).

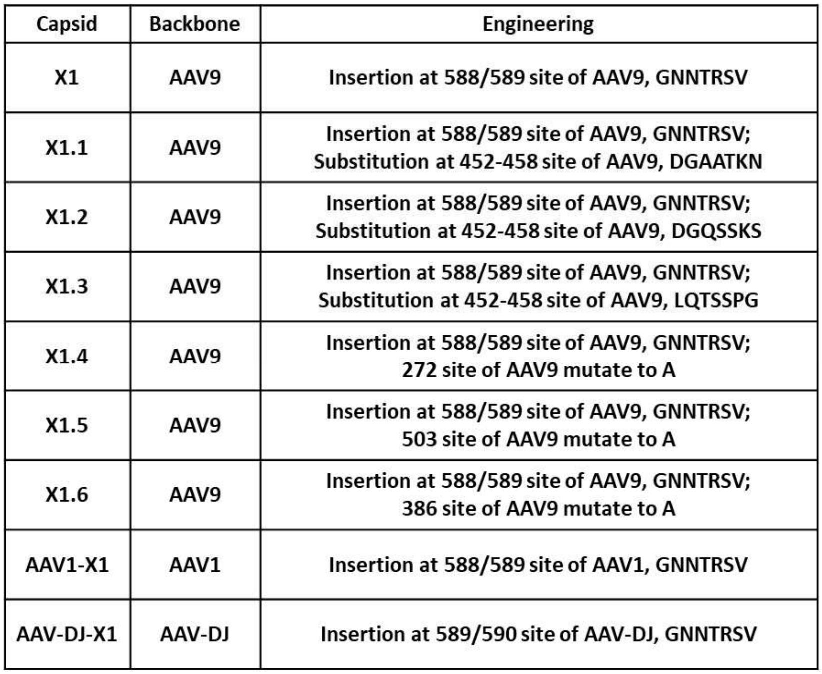

Capsid	Backbone	Engineering
X1	AAV9	Insertion at 588/589 site of AAV9, GNNTRSV
X1.1	AAV9	Insertion at 588/589 site of AAV9, GNNTRSV; Substitution at 452-458 site of AAV9, DGAATKN
X1.2	AAV9	Insertion at 588/589 site of AAV9, GNNTRSV; Substitution at 452-458 site of AAV9, DGQSSKS
X1.3	AAV9	Insertion at 588/589 site of AAV9, GNNTRSV; Substitution at 452-458 site of AAV9, LQTSSPG
X1.4	AAV9	Insertion at 588/589 site of AAV9, GNNTRSV; 272 site of AAV9 mutate to A
X1.5	AAV9	Insertion at 588/589 site of AAV9, GNNTRSV; 503 site of AAV9 mutate to A
X1.6	AAV9	Insertion at 588/589 site of AAV9, GNNTRSV; 386 site of AAV9 mutate to A
AAV1-X1	AAV1	Insertion at 588/589 site of AAV1, GNNTRSV
AAV-DJ-X1	AAV-DJ	Insertion at 589/590 site of AAV-DJ, GNNTRSV

Supplementary Table 1: Summary of engineering approaches for the novel AAVs.

Capsid	Model tested	Sex and age	Administration	Tropism
X1	Wildtype mice (C57BL/6J, BALB/CJ, FVB/NJ, CBA/J)	Both male and female, 6-8 weeks	Intravenously	Brain endothelial cell specific expression
	Transgenic mice (PDGFB-retention motif knock out mice)	Both male and female, 6-8 weeks	Intravenously	Brain endothelial cell specific expression in PDGFB ret/+. Endothelial, neuron, astrocyte expression in PDGFP ret/ret
	Human Brain Microvascular Endothelial cells	-	Direct application	Stronger expression comparing to controls including AAV9, AAV1, AAV2 etc.
X1.1	Wildtype mice (C57BL/6J)	Both male and female, 6-8 weeks or 2 years old	Intravenously	Brain endothelial cell specific expression
	Transgenic mice (Hevin-KO)	Male, 6-8 weeks	Intravenously	Brain endothelial cell specific expression
	Transgenic mice (PDGFB-retention motif knock out mice)	Both male and female, 6-8 weeks	Intravenously	Brain endothelial cell specific expression in PDGFB ret/+, endothelial, neuron, astrocyte expression in PDGFP ret/ret
	Rat	Both male and female, 6-8 weeks	Intravenously	Brain endothelial cell specific expression
	Marmoset	Both male and female, 14 months	Intravenously	Neuron, astrocyte and endothelial cell expression
	Rhesus Macaque	Both male and female, infant	Intravenously	Neuron and endothelial cell expression
	Macaque Brain Slice	Both male and female, adult 2~4 years,	Direct application	predominantly neuron expression with lesser astrocyte, oligodendrocyte, and endothelial cell expression
	Human Brain Microvascular Endothelial cells	-	Direct application	Stronger expression comparing to controls including AAV9, AAV1, AAV2 etc.
	Human Brain Slice		Direct application	Stronger expression comparing to controls including AAV9

Supplementary Table 2: Summary of novel AAVs' performance across models tested.

3.13 MATERIALS AND METHODS

A. Plasmids

1. Library preparation

The plasmids used for AAV library preparation were described previously (Ravindra Kumar et al. 2020; Deverman et al. 2016) (plasmid would be deposited at Addgene). Briefly, plasmid rAAV-ΔCap-in-cis-Lox2 (Fig. 1A) was used for building the heptamer insertion (*7-mer-i*) AAV library. Plasmid pCRII-9Cap-XE was used as a PCR template for the DNA library generation. Plasmid AAV2/9-REP-AAP-ΔCap was used to supplement the AAV library during virus production.

2. DNA construct for AAV characterization

The AAV capsid AAV-X1 was built by inserting 7-mer peptides between AAs 588-589 of AAV9 cap gene in the pUCmini-iCAP-PHP.B backbone (Ravindra Kumar et al. 2020). The AAV-PHP.V1 capsid was described previously (Ravindra Kumar et al, 2020, Addgene 127847). The AAV capsid AAV-X1.1 (Addgene 196836: will be available upon publication), AAV-X1.2, and AAV-X1.3 were built by substituting AAs 452-458 of AAV-X1. The AAV capsids AAV-X1.4, AAV-X1.5, and AAV-X1.6 were built by mutation of AA 272/386/503 in AAV-X1 to Alanine. The AAV capsid AAV1-X1 was built by inserting a 7-mer peptide between AAs 588-589 of the AAV1 cap gene in AAV1-Rep-Cap (Challis et al. 2019) (Addgene 112862).

For *in vivo* validation of AAV capsids, we packaged the vectors with a single-stranded (ss) rAAV genome: pAAV:CAG-eGFP, pAAV:CAG-tdTomato (a gift from Edward Boyden, Addgene plasmid # 59462). To make pAAV:CAG-eGFP-3xMir122-TS (Addgene ID: will be deposited on Addgene), 3 copies of the Mir122-TS were cut out from plasmid CAG-GCaMP6f-3x-miR204-5p-3x-miR122-TS (Challis et al. 2019). To make pAAV:CAG-Hevin-HA, Hevin-HA was synthesized as a gBlocks Gene Fragment (IDT) based off the sequence in the plasmid pAAV:GfaABC1D-Hevin, a gift from Cagla Eroglu’s Lab, and subcloned into the plasmid pAAV:CAG-eGFP by replacing the eGFP gene. To make pAAV:CAG-Ly6a, the Ly6a coding sequence from C57BL/6J was synthesized as a gBlocks Gene Fragment (IDT) and subcloned into the plasmid pAAV:CAG-eGFP by replacing the eGFP gene. pAAV-CAG-FXN-HA was chosen for the *ex vivo* slice study because it contains a ubiquitous CAG promoter and a HA-tagged endogenous human frataxin (FXN) protein and a unique 12bp barcode sequence. The barcode sequence was used to differentiate different capsid packaging the same construct during the next-generation sequencing (NGS) analysis.

3. AAV capsid library generation

The round-1 (R1) and round-2 (R2) libraries were generated as described previously (Ravindra Kumar et al, 2020). Briefly, the R1 library involved a randomized 21-nucleotide (7xNNK mutagenesis) insertion between AAs 588-589 of the AAV9 capsid. The R2 library was built using a *synthetic pool* method (Ravindra Kumar et al. 2020).

B. Animals and subjects

All animal procedures in mice that were carried out in this study were approved by the California Institute of Technology Institutional Animal Care and Use Committee (IACUC), Caltech Office of Laboratory Animal Resources (OLAR), Cantonal Veterinary Office Zurich (license number ZH194/2020, 32869/2020), Duke Division of Laboratory Animal Resources (DLAR). All experimental procedures in rats were conducted at UCL according to the UK Animals Scientific Procedures Act (1986) and under personal and project licenses granted by the Home Office following appropriate ethics review.

All experimental procedures performed on marmosets were approved by the University of California, San Diego, Institutional Animal Care and Use Committee (IACUC) and in accordance with National Institutes of Health and the American Veterinary Medical Association guidelines. Two female animals and one male animal were used in this study and received intravenous injections of AAVs.

All experimental procedures performed on rhesus macaques were approved by the International Animal Care and Use Committee at the University of California, Davis and the California National Primate Research Center (CNPRC). One infant female animal was used in this study and received intravenous injections of AAVs.

All human neurosurgical tissue studies were approved by the Western Institutional Review Board. Human neurosurgical specimens were obtained with informed consent of patients that underwent neocortex resection for the treatment of temporal lobe epilepsy or for tumor removal. Specimens for research were not required for diagnostic purposes and were distal to the pathological focus of the surgical resections (Berg et al., 2021).

For all the experiments performed in this study, the animals were randomly assigned, and the experimenters were not blinded while performing the experiments unless mentioned otherwise.

C. *In vivo* selection and capsid library recovery

For capsid selection *in vivo*, the virus library was intravenously administered to male and female mice of various Cre transgenic lines (n=2-3 per Cre line) at 3×10^{11} vg per mouse in R1 selection, and at 3×10^{11} vg per mouse in R2 selection. Two weeks post injection, mice were euthanized, and the organs of interest were harvested and snap-frozen on dry ice. The tissues were stored at −80°C for long-term. To recover capsids from the tissue, the rAAV genome extractions from tissues were processed using Trizol, and the rAAV genomes were recovered by Cre-dependent PCR or Cre-independent PCR as previously described (Ravindra Kumar et al. 2020). The AAV DNA library, virus library and the libraries recovered from tissue post *in vivo* selection were processed for NGS as also described previously (Ravindra Kumar et al, 2020).

D. Characterization of AAV vectors across models

1. AAV vector production

The AAV vectors were produced using an optimized vector production protocol (Challis et al., 2019). Plasmids were transfected into HEK 293T cells (ATCC) using polyethylenimine. We collected the medium 72 hours after the transfection and harvest both the cell and medium 120 hours after transfection. We precipitated the viral particles from the medium with 40% polyethylene in 500 mM NaCl and combined them with cell pellets for processing. The cell pellets were later suspended with 100 U/mL of salt-activated nuclease in 500 mM NaCl, 40 mM Tris, 2.5 mM MgCl2. AAVs were then harvested from the cell lysates with iodixanol step gradients and ultracentrifugation. Afterward, AAVs were concentrated with Amicon filters and formulated in sterile PBS solution. Transmission electron microscopy (TEM) was used to examine the purity of the prep. Virus titer was measured by qPCR. The average yield was ~ $1x10^{12}$ vg per plate. BR1:CAG-eGFP was purchased from Signagen (SL116035).

2. AAV vector administration in mice and tissue harvest

For the cell-type profiling of the novel AAVs in mice, the AAV vectors were injected intravenously via the retro-orbital route to 6-8 week old adult mice at a dose of $0.1\text{-}1x10^{12}$ vg per mouse. The retro-orbital injections were performed as described previously (Yardeni et al., 2011; Challis et al., 2019). The expression times were ~3 weeks from the time of injection. The dosage and expression time were kept consistent across different experimental groups unless noted otherwise. To harvest the tissues of interest, the mice were anesthetized with Euthasol (pentobarbital sodium and phenytoin sodium solution, Virbac AH) and transcardially perfused using 30 – 50 mL of 0.1 M phosphate buffered saline (PBS) (pH 7.4), followed by 30 – 50 mL of 4% paraformaldehyde (PFA) in 0.1 M PBS. The organs were collected and post-fixed 24-48 h in 4% PFA at 4°C. Following this, the tissues were washed with 0.1 M PBS twice and stored in fresh PBS-azide (0.1 M PBS containing 0.05% sodium azide) at 4°C.

In the Hevin experiment, 4-month-old Hevin KO mice (Kucukdereli et al., 2011) were retro-orbitally injected with either AAV-X1.1:CAG-Hevin-HA or AAV-X1.1:CAG-eGFP (1E12 vg per mouse). After 3 weeks, the mice were perfused and brains were extracted for synapse assay. In the experiment with pericyte-deficient mice, 4-5 month-old PDGFB-retention motif knock out mice (*Pdgfb*$^{ret/ret}$) in a C57BL6/J genetic background (Lindblom et al., 2003) were used. 3E11 vg per mice for X1 and 1E12 vg per mice for X1.1 were injected into mice via the tail vein. 3 weeks post-injection, the anaesthetized animals were perfused for 1–2 min with PBS, followed by 5 min perfusion with 4% PFA in PBS, pH 7.2. Brains were collected and post-fixed in 4% PFA in PBS, pH 7.2 at 4 °C for 6 h.

3. AAV vector administration in rat and tissue harvest

Female rats were used (150-200g) for the experiments. 1E13 vg of the virus was delivered intravenously through the tail vein under light anesthesia. The injected volume was 0.5 ml containing the required number of particles. After 21 days the animals were perfused using 4% PFA solution and PBS. Brains were collected.

4. AAV vector administration in marmoset and tissue harvest

Marmoset monkeys were anesthetized using an intramuscular Ketamine (20 mg/kg) and Acepromazine (0.5 mg/kg) injection. An intravenous catheter was placed in the saphenous vein of the hind leg and flushed with ~2 mL of LRS (Lactated Ringer's solution) for 2 min. Viruses were pooled together in a single syringe (~500-900 µL) and infused at a rate of 200 µL/min into the catheter. Following the infusion, the catheter was flushed with ~3 mL of LRS for 2 min and removed. The animal was then returned to a recovery cage.

Following an incubation period of 4-6 weeks post viral injection, the animals were euthanized by injecting pentobarbital intraperitoneally. Two researchers worked in parallel to harvest the tissue to limit degradation as quickly as possible. Each organ – brain, lungs, kidneys, etc - was removed and separated into two parts. One half of the tissue was flash-frozen in 2-methylbutane that was chilled with dry ice to preserve mRNA and DNA in the harvested tissues. The other half of the tissue was fixed in 4% PFA solution for estimation of protein expression. Flash-frozen tissue samples were transferred to a -80^{o}C freezer, while PFA-fixed tissue samples were stored in a 4^{o}C fridge.

5. AAV vector administration in macaque and tissue harvest

One female rhesus macaque was injected within 10 days of birth. Prior to injection, the animal was anesthetized with ketamine (0.1 mL) and the skin over the saphenous vein was shaved and sanitized. AAVs (2.5×10^{13} vg/kg) were slowly infused into the saphenous vein for ~1 min in < 0.75 mL of 0.1 M PBS. The animal was monitored while they recovered from anesthesia in their home enclosure, and daily for the remainder of the study. The monkey was individually housed within sight and sound of conspecifics.

Tissues were collected 4 weeks post AAV administration. The animal was deeply anesthetized and euthanized using sodium pentobarbital in accordance with guidelines for humane euthanasia of animals at the CNPRC. The whole body was perfused with ice cold RNase-free 0.1 M PBS. The brain was removed from the skull and blocked into 4 mm thick slabs in the coronal plane. Brain slabs and organs were subsequently post-fixed in 4% PFA for 48 h. One hemisphere of the animal was cryoprotected in 10%,15%, and 30% sucrose in 0.1 M PBS.

6. AAV vector administration in ex vivo human and non-human primate brain slices

All procedures involving non-human primates conformed to the guidelines provided by the US National Institutes of Health. *Ex vivo* brain slice culture experiments were performed on temporal cortex tissue from adult *Macaca nemestrina* or *Macaca mulatta* animals housed at the Washington National Primate Research Center. We obtained these brain samples through the Tissue Distribution Program operating under approved University of Washington IACUC protocol number 4277-01. All human neurosurgical tissue studies were approved by the Western Institutional Review Board. Human neurosurgical specimens were obtained with informed consent of patients that underwent neocortex resection for the treatment of temporal lobe epilepsy or for tumor removal. Specimens for research were not required for diagnostic purposes and were distal to the pathological focus of the surgical resections (Berg et al., 2021).

Human and macaque brain slices were prepared using the NMDG protective recovery method (Ting et al., 2014; Ting et al., 2018). Human neurosurgical tissue or macaque brain tissue specimens were placed in carbogenated NMDG artificial cerebral spinal (ACSF) solution containing (in mM): 92 NMDG, 2.5 KCl, 1.25 NaH2PO4, 30 NaHCO3, 20 HEPES, 25 glucose, 2 thiourea, 5 Na-ascorbate, 3 Na-pyruvate, 0.5 CaCl2.4H2O and 10 MgSO4.7H2O. Brain slices were prepared on a VF-200 Compresstome at 300 μm thickness using a zirconium ceramic blade (EF-INZ10, Cadence) and then underwent warmed recovery in carbogenated NMDG aCSF at 32-34*C for 12 minutes. Human and macaque brain slices were placed on membrane inserts in 6 well sterile culture plates, and wells were filled with slice culture medium consisting of 8.4 g/L MEM Eagle medium, 20% heat-inactivated horse serum, 30 mM HEPES, 13 mM D-glucose, 15 mM NaHCO3, 1 mM ascorbic acid, 2 mM MgSO4.7H2O, 1 mM CaCl2.4H2O, 0.5 mM GlutaMAX-I, and 1 mg/L insulin (Ting et al., 2018). The slice culture medium was carefully adjusted to pH 7.2-7.3, osmolality of 300-310 mOsmoles/Kg by addition of pure H2O and then sterile-filtered. Culture plates were placed in a humidified 5% CO2 incubator at 35°C and the slice culture medium was replaced every 2-3 days until end point analysis. 1-3 hours after plating, brain slices were infected by direct application of ~2.5×10^{10} vg of concentrated AAV viral particles distributed over the slice surface.

7. AAV vector characterization in cell cultures

Human brain microvascular endothelial cells (HBMEC) (ScienCell Research Laboratories, cat. no. 1000) were cultured as per the instructions provided by the vendor. The viral vectors packaging ssAAV: CAG-eGFP were added to the cell culture at the multiplicity of infection (MOI) of either 5E4 or 5E3 per well (6 wells per dose per vector). The culture was assessed for fluorescence expression at 1-day post infection. In the *in vitro* Ly6a experiment, HEK293T cells (ATCC, CRL-3216) were cultured in 6-well plate, Ly6a was transiently expressed in HEK293T cells by transfecting each well with 2.53 µg plasmid DNA. Receptor-expressing cells were transferred to 96-well plates and transduced with AAV variants at the MOI of 3E4 or 3E3 per well. The culture was assessed for fluorescence expression at 1-day post infection. HeLa cells (ATCC, CCL-2), U87 cells (ATCC, HTB-

14) and IMR32 cells (ATCC, CCL-127) were cultured as per the instructions provided by the vendor. The viral vectors packaging ssAAV: CAG-eGFP were added to the cell culture at the MOI of 5E4 per well (3 wells per dose per vector). The culture was assessed for fluorescence expression at 1-day post infection.

E. Immunohistochemistry and imaging

In the AAV characterization experiment in mice, tissue sections, typically 100-µm thick, were first incubated in the blocking buffer (10% normal donkey serum (NDS), 0.1% Triton X-100, and 0.01% sodium azide in 0.1 M PBS, pH 7.4) with primary antibodies at appropriate dilutions (Anti-CD31 from Histonova Cat # DIA-310, diluted 1:100; Anti-podocalyxin from R&D Systems Cat # AF1556, diluted 1:100; Anti-CD13 from AbD Serotec, Cat # MCA2183EL, diluted 1:100; Anti-CNN-1 (Calponin 1) from Abcam, Cat # Ab46794, diluted 1:100; Anti-Collagen-IV, from AbD, Serotec Cat # 2150-1470, diluted 1:300; Anti-GFAP from Invitrogen, Cat # 13-030, diluted 1:600; Anti-HA from Roche, Cat# 11867423001, diluted 1:200; Anti-GFP from Aves Labs, Cat# GFP-1020, diluted 1:500; Anti-GLUT1 from Millipore, Cat# 07-1401, diluted: 1:500; Anti-S100β from Abcam, Cat# ab52642, diluted: 1:500; Anti-NeuN from Abcam, Cat# ab177487, diluted: 1:500) for 24 h at room temperature (RT) on a rocker. After primary antibody incubation, the tissues were washed 1-3 times with wash buffer 1 (0.1% Triton X-100 in 0.1 M PBS buffer, pH 7.4) over a period of 5-6 h in total. The tissues were then incubated in the blocking buffer with the secondary antibodies at appropriate dilutions for 12-24h at RT and then washed 3 times in 0.1 M PBS over a total duration of 5-6 h. When performing DNA staining, the tissues were incubated with 4’, 6-diamidino-2-phenylindole (DAPI) (Sigma Aldrich, 10236276001, 1:1000) in 0.1 M PBS for 15 min followed by a single wash for 10 min in 0.1 M PBS. The DAPI and/or antibody-stained tissue sections were mounted with ProLong Diamond Antifade Mountant (ThermoFisher Scientific, P36970) before imaging them under the microscope. The images were acquired with a Zeiss LSM 880 confocal microscope using the following objectives: Plan-Apochromat 10× 0.45 M27 (working distance 2.0 mm), and Plan-Apochromat 25× 0.8 Imm Corr DIC M27 multi-immersion. The liver images were acquired with a Keyence BZ-X700 microscope using a 10x objective. The images were then processed in the following image processing softwares: Zen Black 2.3 SP1 (for Zeiss confocal images) and BZ-X Analyzer (for Keyence images).

In the rat experiment, whole brains were imaged using serial section two-photon microscopy (Mayerich, Abbott, and McCormick, 2008; Ragan et al., 2012). Our microscope was controlled by ScanImage Basic (Vidrio Technologies, USA) using BakingTray, a custom software wrapper for setting up the imaging parameters (Campbell, 2020). 50-60um slices were cut and 7-9 optical planes were imaged using a 16x objective. Images were assembled using StitchIt (Campbell, Blot, and lguerard, 2020).

In the Hevin experiment, for synaptic puncta analysis of mouse primary visual cortex (area V1), brains were cryosectioned at 25 µm using Leica CM3050S (Leica, Germany). Tissue sections were washed and permeabilized in TBS with 0.2% Triton-X 100 three times at room temperature followed by blocking in 5% Normal Goat Serum (NGS) for 1 hr at room temperature. To label pre and postsynaptic proteins, VGluT2 (Synaptic Systems; Cat# 135 404) and PSD95 (Thermo Fisher; Cat# 51-6900) antibodies were used, respectively. Primary antibodies were diluted in 5% NGS containing TBST and incubated overnight at 4 °C. Secondary antibodies (Alexa Fluor conjugated; Invitrogen) were added in TBST with 5% NGS for 2hr at room temperature. Slides were mounted in Vectashield with DAPI (Vector Laboratories, CA). Images were acquired with Olympus FV 3000 inverted confocal microscope using high magnification 60x objective plus 1.64x optical zoom z-stack images containing 15 optical sections spaced 0.33µm apart. During the post processing of captured images, each z-stack was converted into 5 maximum projection images (MPI) by combining three optical sections using ImageJ software. The number of co-localized excitatory thalamocortical (VGluT2/PSD95) synaptic puncta were obtained using the ImageJ plugin Puncta Analyzer (Ippolito and Eroglu, 2010).

In the pericyte-deficient mice experiment, coronal vibratome sections (60 µm) of brains were cut using the Leica VT1000S. Free floating brain sections were incubated in the blocking/permeabilization solution (1% bovine serum albumin, 0.5% Triton X-100 in

PBS) overnight at 4 °C, followed by incubation in primary antibody solution for two nights at 4 °C, and subsequently in secondary antibody solution, overnight at 4 °C. Sections were incubated with DAPI (4’,6-Diamidino-2-phenylindole dihydrochlorid) solution(D9542, Sigma-Aldrich, diluted 1:10000) for 7 minutes at RT and subsequently mounted in ProLong Gold Antifade mounting medium (cat. #P36930). Life Technologies). Images were taken with Leica SP8 inverse, 20 X objective PL APO CS (NA 0.7) (Leica Microsystems). Widefield images were generated using Slidescanner Zeiss Axio Scan.Z1 (Leica Microsystems). Image processing was done using Fuji and Zen2. All confocal images are represented as maximum intensity projections.

In the marmoset and macaque experiment, coronal sections (100 μm) of brains were cut using the Leica VT1000S. Sections (50-100 μm) of gut, DRG and spinal cord were cut using a cryostat (Leica Biosystems). Tissue were stained with relevant antibody following the similar protocol in the mouse characterization experiment. The images were acquired with a Zeiss LSM 880 confocal microscope using the following objectives: Plan-Apochromat 10× 0.45 M27 (working distance 2.0 mm), and Plan-Apochromat 25× 0.8 Imm Corr DIC M27 multi-immersion. The images were then processed in the Zen Black 2.3 SP1 (for Zeiss confocal images).

In the primate *ex vivo* slice culture experiments, following 7-10 days post virus infection, temporal cortex brain slices were fixed in 4% PFA for 24 hours at 4*C. After PFA fixation, the slices were transferred into 30% sucrose in water for >24 hours and then sub-sectioned on a sliding microtome to 15-30 μm for immunostaining using the following antibodies: mouse anti-HA (Biolegend catalog #901513, 1:1000) and rabbit anti-NeuN (Millipore catalog #ABN78, 1:2000). In a subset of IHC experiments we performed co-immunostaning with additional cell type marker antibodies including the following: rabbit anti-GLUT1 (Millipore catalog #07-1401, 1:1000), rabbit anti-Olig2 (Abcam catalog #AB9610, 1:1000), and mouse anti-S100β (Millipore catalog #S2532, 1:1000). We also switched from mouse anti-HA to rat anti-HA (Roche catalog #3F10, 1:1000) to circumvent antibody cross reactivity issues observed with Olig2 and other cell type markers. Secondary antibodies included Goat anti-mouse, Goat anti-rabbit, or Goat anti-rat Alexa Fluor conjugated antibodies (A488, A555, A647 from ThermoFisher) as needed. Slices were incubated in 1ug/mL DAPI solution and mounted on 1x3 inch slides with Prolong Gold mounting medium. Region of interest (ROI) in the neocortical grey matter spanning L3/4/5 were imaged on an Olympus FV3000 confocal microscope using 405nm, 561nm, and 640nm laser lines. Z-stack images were acquired at 1um step sized through the slice thickness and collapsed to made maximum intensity projection images. Every attempt was made to select comparable ROIs in the brain slices that best captured viral reporter expression patterns and to image at matched settings to directly compare across the capsid variants. In some cases, images needed to be pseudo-colored post-acquisition for best effect of illustrating signal overlap in two channel merged images (green and magenta with overlap in white).

In the RNAScope FISH and antibody labeling on ex vivo slice culture experiments, 350 µm thick macaque cortical slices were obtained, cultured and transduced as above. After eight days in culture, slices were fixed in 4% PFA (Electron Microscopy Sciences) at 4°C for 12 hours and cryoprotected in 30% sucrose. Thick slices were subsection 15 µm on a freezing sliding microtome (Leica SM2000R) and stored in 1 x phosphate buffered saline (PBS) + 0.1% sodium azide at 4°C. RNAscope Multiplex Fluorescent v2 (Advanced Cell Diagnostics) was performed, and if not otherwise noted, buffers or solutions were obtained from the ACD v2 kit. Sections were washed in 1 x PBS, mounted onto slides, and dried at 60°C. Samples were fixed in 4% paraformaldehyde (PFA) for 15 min at 4°C followed by a series of five minute washes in solutions with increasing ethanol concentrations (50%, 70%, 100%, 100%). Hydrogen peroxide was applied to the sections, incubated at RT for 10 minutes, and washed in 1x PBS twice for 1 min. Samples were incubated in Target Retrieval Reagent for 5-7min at 100°C. Slides were rinse in deionized water and incubated in 100% ethanol for 3 minutes and air-dried. Hydrophobic barrier around the tissue was created with an ImmEdge Pen (Vector Laboratories, H-4000). Samples were treated with Protease III for 30 minutes at 40°C and then washed twice in 1x PBS for 1 min at RT. We used a C1 probe designed by ACD against SYFP2 for detection of the EGFP reporter mRNA. Sections were incubated in this probe for 3 hours at 40°C. Sections were then washed twice in 1x Wash Buffer for 2 minutes each at RT, then incubated in 5x Sodium Chloride Sodium Citrate (SSC) (Invitrogen) overnight at RT. Sections were incubated in Amp1 reagent for 30 min at 40°C then washed twice in 1x Wash Buffer for 2 min at RT. Sections were then incubated in Amp2 reagent for 30 min at 40°C, then washed twice in 1x Wash Buffer for 2 min at RT. Sections were then incubated in Amp3 reagent for 15 min at 40°C, then washed twice in 1X Wash Buffer for 2 min at RT. Sections were then incubated in HRP-C1 at 40C for 15 min, washed twice in 1x Wash Buffer for 2 min at RT, then incubated in TSA Cy3 (Perkin Elmer, diluted 1:1500 in TSA Buffer) at for 30 min at 40C. Sections were then incubated in HRP Blocker at 40°C for 30 min and washed twice in 1x Wash Buffer for 2 min each at RT. Sections were washed in 1x PBS for 2 min at RT then fixed in 4% PFA for 15 min at RT. Sections were washed twice in 1x PBS for 5 min. Next, slides were incubated in a blocking buffer of 10% normal goat serum (Jackson ImmunoResearch) in PBS for 15 min at RT. Sections were incubated in primary antibody for 1 hour at RT: rabbit Anti-GLUT1 (Millipore), chicken Anti-GFP (Aves). Samples were then washed twice in 1x PBS for 5 min each, then incubated in secondary antibody for 1 hour at RT: goat anti-rabbit Alexa Fluor 488 (ThermoFisher), goat anti-chicken Alexa Fluor 488 (ThermoFisher). Samples were washed twice in 1x PBS for 5 min each, counterstained with DAPI for 30 seconds at RT, then mounted with Prolong Gold Antifade Mountant (ThermoFisher Scientific, P36930). Samples were imaged on an Olympus confocal FluoView3000 using a 30x silicone immersion objective or a Nikon Ti2 epifluorescence microscope with a 20x objective. Montage images were stitched on the Olympus software (FV31S-SW), stacks were Z-projected and analyzed using FIJI. Images from the Nikon are not montages, are from a single plane. All analysis was done in FIJI.

F. Protein production

Ly6a-Fc was produced in Expi293F suspension cells grown in Expi293 Expression Medium (Thermo Fisher Scientific) in a 37 °C, 5% CO2 incubator with 130 rpm shaking. Transfection was performed with Expifectamine according to manufacturer's instructions (Thermo Fisher Scientific). Following harvesting of cell conditioned media, 1 M Tris, pH 8.0 was added to a final concentration of 20 mM. Ni-NTA Agarose (QIAGEN) was added to ~5% conditioned media volume. 1 M sterile PBS, pH 7.2 (GIBCO) was added to ~3X conditioned media volume. The mixture was stirred overnight at 4 °C. Ni-NTA agarose beads were collected in a Buchner funnel and washed with ~300 mL protein wash buffer (30 mM HEPES, pH 7.2, 150 mM NaCl, 20 mM imidazole). Beads were transferred to an Econo-Pak Chromatography column (Bio-Rad) and protein was eluted in 15 mL of elution buffer (30 mM HEPES, pH 7.2, 150 mM NaCl, 200 mM imidazole). Proteins were concentrated using Amicon Ultracel 10K filters (Millipore) and absorbance at 280 nm was measured using a Nanodrop 2000 spectrophotometer (Thermo Fisher Scientific) to determine protein concentration.

G. Surface Plasmon Resonance (SPR)

Experiments were performed using a Sierra SPR-32 Pro (Bruker). Ly6a-Fc fusion protein in HBS-P+ buffer (GE Healthcare) was immobilized to a protein A sensor chip at a capture level of approximately 1200 -1500 response units (RUs). Two-fold dilutions of rAAV beginning at 4 x 10^{12} v.g. mL^{-1} were injected at a flow rate of 10 µl min^{-1} with a contact time of 240 s and a dissociation time of 600 s. The protein A sensor chip was regenerated with 10 mM glycine pH 1.5 after each cycle. Kinetic data were double reference subtracted.

H. Bulk sequencing for capsid enrichment in ex vivo tissue

Ex vivo NHP or human brain slice cultures were either infected with the pool of viruses with equivalent molar ratio or infected with PHP.eB packaging non CAG-FXN-HA construct. After 7 or 10 days *in vitro*, the tissues were snap frozen and shipped to Caltech on dry ice. Tissues were immediately stored at -80°C upon receipt. RNA was extracted from the whole tissue or half of the tissue following a slightly modified

Phenol/Chloroform protocol (Goertsen et al., 2021). RNA was further cleaned by treating with DNase using RNA Clean & Concentrator-5 kit (Zymo), and reverse-transcription was done on up to 1 µg purified RNA using Superscript IV VILO Master Mix (ThermoFisher). If DNA was needed from the tissue, DNA was extracted from the other half of the tissue using QIAamp DNA Mini Kit (Qiagen) followed the manufacturer's instructions.

The barcoded FXN region was recovered from the resulting cDNA library or DNA using primers of 5'-TGGACCTAAGCGTTATGACTGGAC-3' and 5'-GGAGCAACATAGTTAAGAATACCAGTCAATC-3' and PCR was performed using Q5 2x Master Mix (New England BioLabs) at 25 cycles of 98°C for 10s, 63°C for 15s, and 72°C for 20s. Each sample was run in up to 5 reactions using up to 50 ng of cDNA or DNA, each, as a template. After PCR, samples were purified using DNA Clean & Concentrator-25 kit (Zymo). The barcoded FXN region was further recovered and the adaptor sequence was added by performing PCR using primers of 5'-ACGCTCTTCCGATCTTGTTCCAGATTACGCTTGAG-3' and 5'-TGTGCTCTTCCGATCTTGTAATCCAGAGGTTGATTATCG-3' at 10 cycles of 98°C for 10s, 55°C for 15s, and 72°C for 20s. Samples were then purified using DNA Clean & Concentrator-25 kit. Index sets in the NEBNext Dual Index Primers (New England BioLabs) were carefully chosen and added to the barcoded FXN region by performing PCR at 10 cycles of 98°C for 10s, 60°C for 15s, and 72°C for 20s. To further separate the sequence for later next-generation sequencing (NGS), the PCR samples were run on a 2% low-melting-point agarose gel for separation and recovery of the 210bp band.

NGS was performed on an Illumina MiSeq Next Generation Sequencer (Illumina) using a 150-cycle MiSeq Reagent Kit v3 (Illumina) following the manufacturer's procedure. All samples were pooled in equal ratio to a 4 nM library. 10% 20 pM PhiX control was spiked in to add diversity to the library. Demultiplexing was done by BaseSpace Sequence Hub and the barcode counting analysis was performed using in-house Python code. For each brain slice culture, the enrichment of capsid variants was calculated by the ratio of the counts of their corresponding barcode to the counts of the corresponding barcode to the internal control capsid (e.g. AAV9 or PHP.eB). To correct any potential error due to titer determination, PCR amplification, or sequencing, DNA from the same pool of virus that was used for the brain slice culture infection was extracted, amplified, and included in the MiSeq NGS and analysis. The enrichment of the capsid variants was then normalized by the input viral DNA in the pool.

I. QPCR and RT-PCR for vector genome and RNA transcript in ex vivo tissue

Quantitative PCR and quantitative RT-PCR to measure AAV variant transduction and expression in NHP slice culture. We cut physiological slices (300 microns thick) from the superior temporal gyrus from one adult (age 14 year and 1 month, weight 10.83 kg) M. mulatta animal housed at University of Washington National Primate facility. The animal had been planned for routine euthanasia and we collected the brain as part of the facility's tissue distribution program. We sectioned a block of superior temporal gyrus and the slices were recovered as described by Ting et al. 2021, and then we cultured the slices on the air-liquid membrane interface as described in Mich et al. 2021. At 30 minutes following slice plating, we transduced the slices on their face with ~1-2 uL. CAG-EGFP vectors, packaged in AAV9 or X1.1 (titers approximately 5e13 gc/mL). We performed transductions on three biological replicates for each vector. We refreshed the culture medium every 48 hours until tissue harvest at 8 days *in vitro*. At harvest, we imaged the slices to confirm transduction, and then bisected the slices, and quick-froze each slice half in a dry ice-ethanol bath, then stored them at -20 degrees C until nucleic acid processing.

One slice half (~20 mg wet tissue weight) was processed to isolate DNA, and the other slice half was processed to isolate RNA for cDNA preparation. We isolated DNA using the Qiagen DNeasy Blood and Tissue Kit (Qiagen, catalog # 69504) with no modifications to the protocol, yielding approximately 3-5 ug total DNA per slice half. We isolated RNA using first TRIzol (Thermo Fisher Scientific, catalog #15596026) to isolate crude dilute RNA, which we then purified and concentrated using the PureLink RNA Mini Kit (Thermo Fisher Scientific, catalog # 12183018A). On the column of the PureLink RNA

Mini Kit, we also performed DNA digestion by modifying the first wash as follows: we first washed with 350 uL of Wash Buffer 1, then added 80 uL of RNase-Free DNaseI in RDD buffer (Qiagen catalog # 79254) and incubated the column at room temperature for 15 minutes, then washed again with 350 uL of Wash Buffer 1, and proceeded with washing and elution as per the protocol. Typically, this technique yielded ~1.5 ug DNA-free total RNA per slice half. We then performed first-strand cDNA synthesis from 400 ng total RNA in 20 uL reactions using Promega GoScript Reverse Transcription Kit (Promega, catalog # A5000).

For quantitative PCR we used 100 ng DNA in a 20 uL amplification reaction using the following Taqman probes (all from Thermo Fisher Scientific): EGFP-FAM probe (Assay ID Mr04097229_mr, catalog #4331182), and custom genomic reference probe CN2386-2-VIC (Assay ID ARH6DUK catalog #4448512, designed to target both M. mulatta and M. nemestrina). For quantitative RT-PCR we used 1 uL of cDNA (20 ng of original total RNA) in a 10 uL amplification reaction using the following probes: EGFP-FAM probe (same probe as used for DNA detection), and custom housekeeping reference probe GAPDH-VIC (Assay ID APAAHJR, catalog #4448508, designed to target both M. mulatta and M. nemestrina). We amplified and detected these reactions on a Roche Lightcycler II instrument alongside standard curves consisting of serial dilutions of plasmid DNA or purified PCR amplicons in the case of GAPDH. Then we extracted Cp values using the second derivative method, calculated the relative abundances of vector DNA/RNA with respect to internal reference probes, and normalized these ratios to those observed with AAV9 vector. In some cases, the EGFP-FAM probe was so abundant that it interfered with detection of the VIC reference probes; in these cases, the reactions were run in separate wells.

J. Data analysis

1. Quantification of AAV transduction *in vivo*:

The quantification of AAV transduction across tissues was carried out by manually counting fluorescent expression resulting from the AAV genome. ImageJ was used for this purpose.

2. NGS data alignment, processing and analysis:

The NGS data analysis was carried out using a custom data-processing pipeline with scripts written in Python (https://github.com/GradinaruLab/mCREATE) (Ravindra Kumar et al., 2020) and using plotting software such as Plotly, Seaborn, and GraphPad PRISM 7.05. The AAV9 capsid structure model was produced with PyMOL.

3. Enrichment score calculation:

The enrichment score for a variant was determined using the following formula: Enrichment score of variant "x" in tissue1= log10 [(Enrichment of variant 'X' in the tissue1) / (Enrichment of variant 'X' in the virus pool)]. Enrichment of variant 'X' in the tissue1 = (Variant "x" RC in tissue library) / (Sum of variants N RC in tissue1). Enrichment of variant 'X' in the virus pool = (Variant "x" RC in virus pool) / (Sum of variants N RC in virus pool), Where N is the total number of variants in a library.

4. Fold change calculation:

The fold-change of a variant "x" to AAV9 = (The enrichment score of "x") / (The enrichment score of AAV9).

3.14 OTHER INFORMATION

Contributions

X.C. and V.G. designed the experiments. X.C., D.A.W., J. T.T., M. Z., D.S.B., H.S., S.R.K., T.F.S., E.S., D.G., V.N. performed experiments. D.A.W. assisted with the characterization of the vectors across models. D.S.B. and C.E. designed and conducted the *in vivo* Hevin expression experiments. J.T.T., M.Z., D.G., V.O., N.T., N.W., J.M., Y.B., D.M., B.G., B.P.L, and E.S.L. assisted with the characterization of variants in *ex vivo* macaque and human brain slices. T.M. and E.S. assisted with the SPR experiment and the Ly6a experiment in HEK293T cells. S.H. and A.K. assisted with the characterization of the vectors in pericyte-deficient mice and vascular cell type specific transduction. S.R.K assisted with the HBMEC experiment and early iteration of the library. C.M.A assisted with tissue processing in macaque. X.D generated the AAV1 and AAV9 models. V.P. and A.A. assisted with the characterization in rat with the support of the staff at SWC. V.N. and C.T.M. assisted with the characterization of the virus in marmoset with the support of vet staff at UCSD. L.J.C and A.F assisted with the characterization of the virus in rhesus macaque with the support of vet staff at UC Davis. X.C. prepared the figures with input from all authors. X.C. and V.G. wrote the manuscript with input from all authors. V.G. supervised all aspects of the work.

Acknowledgments

We thank members of the Gradinaru group for their assistance in this study: Yaping Lei for help with virus production, Miguel Chuapoco for discussion on the macaque experiment, Min Jee Jang and Cameron Jackson for attempt on FISH experiment, Elisha Mackey for mouse colony management, Zhe Qu for lab management, Patricia Anguiano for administrative assistance, and the entire Gradinaru group for discussions. We thank I. Antoshechkin and the Millard and Muriel Jacobs Genetics and Genomics Laboratory at Caltech for providing sequencing service. We thank the Beckman Institute Single-Cell Profiling and Engineering Center (SPEC) at Caltech and Sisi Chen for providing sequencing machines. We thank Annie W. Lam and Jost Vielmetter of the Beckman

Institute Protein Expression Center at Caltech for Ly6a protein production and for providing surface plasmon resonance machines. We thank Sian Murphy at SWC's Neurobiological Research Facility (NRF) for the injection of the rats. We thank Cassandra Tang-Wing and Chris Chamberlain at UCSD for the injection of the marmosets. We thank Michael Metke and Vikram Pal Singh at UCSD for the tissue collection from marmosets. We thank the staff at the California National Primate Research Center for the experiment in rhesus macaque. We thank Catherine Oikonomou for help with manuscript editing. This work was primarily supported by grants from the National Institutes of Health (NIH) to V.G.: NIH Director's New Innovator DP2NS087949 and PECASE, NIH BRAIN Armamentarium 1UF1MH128336-01, NIH Pioneer 5DP1NS111369-04 and SPARC 1OT2OD024899. Additional funding includes the Vallee Foundation (V.G.), the Moore Foundation (V.G.), the CZI Neurodegeneration Challenge Network (V.G. and C.E.), and the NSF NeuroNex Technology Hub grant 1707316 (V.G.), the Heritage Medical Research Institute (V.G.) and the Beckman Institute for CLARITY, Optogenetics and Vector Engineering Research (CLOVER) for technology development and dissemination (V.G.), NIH BRAIN UG3MH120095 (J.T.T, V.G.), CNPRC base grant (NIH P51 OD011107, A.F.), the Swiss National Science Foundation (310030_188952, A.K), the Synapsis (grant 2019-PI02, A.K.), the Swiss Multiple Sclerosis Society (A.K.). C.E. is an investigator of the Howard Hughes Medical Institute.

Competing interests

The California Institute of Technology has filed patent applications for the work described in this manuscript, with X.C. and V.G. listed as inventors. V.G. is a co-founder and board member of Capsida Biotherapeutics, a fully integrated AAV engineering and gene therapy company.

Chapter 4

FUTURE DIRECTIONS

4.1 BROADER APPLICATION OF THE ENGINEERED AAVS

The engineered systemic AAVs has been shown to be used for neuronal activity monitoring, neuronal function modulation as well as providing therapeutic protein for the nervous system in this work. We are just at the start of the broad application of these systemic AAVs. Their broad transduction of nervous system could enable researchers to study disease which has both CNS and PNS indication such as Friedreich ataxia. There are more and more evidence of the importance of brain and peripheral interaction, these tools would be a good venue to dissect out those interactions. The interesting tropism of these vectors we observed in non-human primate would also enable researchers to study the nervous system in a system that is more similar to human, thus informing the best practice for clinical intervention for nervous system disease.

4.2 INVESTIGATION OF THE ACTING MECHANISM OF THE NOVEL AAVS

The engineered systemic AAVs has been The beauty of directed evolution is it provides the opportunity to identify top candidates without knowing the acting mechanism. We indeed identify series of AAVs from directed evolution that enable us to target the nervous system efficiently and specifically. However, we observed some tropism difference when testing across species. Some tropism difference come to us as surprise partially due to our lack of understanding for their acting mechanism. With all these powerful AAVs in hand, we could start exploring how they gain this new property comparing to their parents. One factor that contribute to their newly-gained tropism could be newly-gained interaction with certain receptor expressed in the target tissue. We are starting to identify the key receptors for the novel AAVs through screening of relevant proteome. Understanding their receptors could increase our confidence when applying them to more species and more varied physiological condition. We could first evaluate the expression profile of these novel receptors before we applied the novel AAVs to those different conditions.

4.3 FURTHER ENGINEERING AGAINST THE IDENTIFIED ACTING MECHANISM

The identifications of the novel receptor for AAVs also open new engineering space. Some of these receptors were not thought to be involve in transcytosis at BBB before, these newly identified mechanism provided new path to engineer bio agents for CNS drug delivery. Human version of these receptor would also enable us to rationally engineer for future clinical application. The incorporation of novel computational methods would also enable us to fine tune the interaction between the candidates and the receptors, thus fine tuning the bio agents’ tropism. This novel receptor-based engineering platform could be used for engineering AAVs, antibodies and small molecule for nervous system drug delivery.

BIBLIOGRAPHY

Adachi, Kei, Tatsuji Enoki, Yasuhiro Kawano, Michael Veraz, and Hiroyuki Nakai. 2014. "Drawing a High-Resolution Functional Map of Adeno-Associated Virus Capsid by Massively Parallel Sequencing." *Nature Communications* 5 (1): 3075. https://doi.org/10.1038/ncomms4075.

Ali, Hossamaldein Gaber, Khalid Ibrahim, Mahmoud Fawzi Elsaid, Reem Babiker Mohamed, Mahmoud I. A. Abeidah, Azhar Othman Al Rawwas, Khaled Elshafey, et al. 2021. "Gene Therapy for Spinal Muscular Atrophy: The Qatari Experience." *Gene Therapy*, July, 1–5. https://doi.org/10.1038/s41434-021-00273-7.

Armulik, Annika, Guillem Genové, Maarja Mäe, Maya H. Nisancioglu, Elisabet Wallgard, Colin Niaudet, Liqun He, et al. 2010. "Pericytes Regulate the Blood-Brain Barrier." *Nature* 468 (7323): 557–61. https://doi.org/10.1038/nature09522.

Arnold, Frances H. 1998. "When Blind Is Better: Protein Design by Evolution." *Nature Biotechnology* 16 (7): 617–18. https://doi.org/10.1038/nbt0798-617.

Arnold, Frances H. 2001. "Combinatorial and Computational Challenges for Biocatalyst Design." *Nature* 409 (6817): 253–57. https://doi.org/10.1038/35051731.

Aschauer, Dominik F., Sebastian Kreuz, and Simon Rumpel. 2013. "Analysis of Transduction Efficiency, Tropism and Axonal Transport of AAV Serotypes 1, 2, 5, 6, 8 and 9 in the Mouse Brain." *PloS One* 8 (9): e76310. https://doi.org/10.1371/journal.pone.0076310.

Asencor, Andoni I., Gennady Dvoryanchikov, Pantelis Tsoulfas, and Nirupa Chaudhari. 2021. "AAV-PHP.S-Mediated Delivery of Reporters to Cranial Ganglion Sensory Neurons." *bioRxiv*, 2021-09. https://doi.org/10.1101/2021.09.14.460327.

Batista, Ana Rita, Oliver D. King, Christopher P. Reardon, Crystal Davis, null Shankaracharya, Vivek Philip, Heather Gray-Edwards, et al. 2020. "Ly6a Differential Expression in Blood-Brain Barrier Is Responsible for Strain Specific Central Nervous System Transduction Profile of AAV-PHP.B." *Human Gene Therapy* 31 (1–2): 90–102. https://doi.org/10.1089/hum.2019.186.

Bedbrook, Claire N., Benjamin E. Deverman, and Viviana Gradinaru. 2018. “Viral Strategies for Targeting the Central and Peripheral Nervous Systems.” *Annual Review of Neuroscience* 41 (1): 323–48. https://doi.org/10.1146/annurev-neuro-080317-062048.

Bedbrook, Claire N., Kevin K. Yang, J. Elliott Robinson, Elisha D. Mackey, Viviana Gradinaru, and Frances H. Arnold. 2019. “Machine Learning-Guided Channelrhodopsin Engineering Enables Minimally-Invasive Optogenetics.” *Nature Methods* 16 (11): 1176–84. https://doi.org/10.1038/s41592-019-0583-8.

Bell, Christie L., Brittney L. Gurda, Kim Van Vliet, Mavis Agbandje-McKenna, and James M. Wilson. 2012. “Identification of the Galactose Binding Domain of the Adeno-Associated Virus Serotype 9 Capsid.” *Journal of Virology* 86 (13): 7326–33. https://doi.org/10.1128/JVI.00448-12.

Berg, Jim, Staci A. Sorensen, Jonathan T. Ting, Jeremy A. Miller, Thomas Chartrand, Anatoly Buchin, Trygve E. Bakken, et al. 2021. “Human Neocortical Expansion Involves Glutamatergic Neuron Diversification.” *Nature* 598 (7879): 151–58. https://doi.org/10.1038/s41586-021-03813-8.

Bevan, Adam K., Sandra Duque, Kevin D. Foust, Pablo R. Morales, Lyndsey Braun, Leah Schmelzer, Curtis M. Chan, et al. 2011. “Systemic Gene Delivery in Large Species for Targeting Spinal Cord, Brain, and Peripheral Tissues for Pediatric Disorders.” *Molecular Therapy: The Journal of the American Society of Gene Therapy* 19 (11): 1971–80. https://doi.org/10.1038/mt.2011.157.

Bey, Karim, Johan Deniaud, Laurence Dubreil, Béatrice Joussemet, Joseph Cristini, Carine Ciron, Juliette Hordeaux, et al. 2020. “Intra-CSF AAV9 and AAVrh10 Administration in Nonhuman Primates: Promising Routes and Vectors for Which Neurological Diseases?” *Molecular Therapy. Methods & Clinical Development* 17 (June): 771–84. https://doi.org/10.1016/j.omtm.2020.04.001.

Bočkor, L., G. Bortolussi, A. Iaconcig, G. Chiaruttini, C. Tiribelli, M. Giacca, F. Benvenuti, L. Zentilin, and A. F. Muro. 2017. “Repeated AAV-Mediated Gene Transfer by Serotype Switching Enables Long-Lasting Therapeutic Levels of HUgt1a1 Enzyme in a Mouse Model of Crigler–Najjar Syndrome Type I.” *Gene Therapy* 24 (10): 649–

60. https://doi.org/10.1038/gt.2017.75.

Bortolussi, Giulia, Lorena Zentillin, Jana Vaníkova, Luka Bockor, Cristina Bellarosa, Antonio Mancarella, Eleonora Vianello, et al. 2014. “Life-Long Correction of Hyperbilirubinemia with a Neonatal Liver-Specific AAV-Mediated Gene Transfer in a Lethal Mouse Model of Crigler–Najjar Syndrome.” *Human Gene Therapy* 25 (9): 844–55. https://doi.org/10.1089/hum.2013.233.

Bourdenx, Mathieu, Nathalie Dutheil, Erwan Bezard, and Benjamin Dehay. 2014. “Systemic Gene Delivery to the Central Nervous System Using Adeno-Associated Virus.” *Frontiers in Molecular Neuroscience* 7: 50. https://doi.org/10.3389/fnmol.2014.00050.

Campbell, Rob, Antonin Blot, and lguerard. 2020. SainsburyWellcomeCentre/StitchIt: Last Release of Stitching Model 1. *Zenodo*. https://doi.org/10.5281/zenodo.3941901.

Campbell, Rob. 2020. SainsburyWellcomeCentre/BakingTray: Jan 2020. *Zenodo*. https://doi.org/10.5281/zenodo.3631610.

Cavanaugh, Daniel J., Alexander T. Chesler, Alexander C. Jackson, Yaron M. Sigal, Hiroki Yamanaka, Rebecca Grant, Dajan O’Donnell, et al. 2011. “Trpv1 Reporter Mice Reveal Highly Restricted Brain Distribution and Functional Expression in Arteriolar Smooth Muscle Cells.” The Journal of Neuroscience: The Official Journal of the Society for Neuroscience 31 (13): 5067–77. https://doi.org/10.1523/JNEUROSCI.6451-10.2011.

Chakrabarti, Sampurna, Luke A. Pattison, Balint Doleschall, Rebecca H. Rickman, Helen Blake, Gerard Callejo, Paul A. Heppenstall, and Ewan St. John Smith. 2020. “Intraarticular Adeno-Associated Virus Serotype AAV-PHP.S–Mediated Chemogenetic Targeting of Knee-Innervating Dorsal Root Ganglion Neurons Alleviates Inflammatory Pain in Mice.” *Arthritis & Rheumatology* 72 (10): 1749–58. https://doi.org/10.1002/art.41314.

Challis, Rosemary C., Sripriya Ravindra Kumar, Ken Y. Chan, Collin Challis, Keith Beadle, Min J. Jang, Hyun Min Kim, et al. 2019. “Systemic AAV Vectors for Widespread and Targeted Gene Delivery in Rodents.” *Nature Protocols* 14 (2): 379. https://doi.org/10.1038/s41596-018-0097-3.

Challis, Rosemary C., Sripriya Ravindra Kumar, Xinhong Chen, David Goertsen, Gerard M. Coughlin, Acacia M. Hori, Miguel R. Chuapoco, Thomas S. Otis, et al. 2022. "Adeno-Associated Virus Toolkit to Target Diverse Brain Cells." *Annual Review of Neuroscience* 45:447–69. https://doi.org/10.1146/annurev-neuro-111020-100834

Chan, Ken Y., Min J. Jang, Bryan B. Yoo, Alon Greenbaum, Namita Ravi, Wei-Li Wu, Luis Sánchez-Guardado, et al. 2017. "Engineered AAVs for Efficient Noninvasive Gene Delivery to the Central and Peripheral Nervous Systems." *Nature Neuroscience* 20 (8): 1172–79. https://doi.org/10.1038/nn.4593.

Chen, Ritchie, Andres Canales, and Polina Anikeeva. 2017. "Neural Recording and Modulation Technologies." *Nature Reviews. Materials* 2 (2): 16093. https://doi.org/10.1038/natrevmats.2016.93.

Chen, Wenli, Shun Yao, Jie Wan, Yu Tian, Lan Huang, Shanshan Wang, Farhana Akter, Yinqiu Wu, Yizheng Yao, and Xiaochun Zhang. 2021. "BBB-Crossing Adeno-Associated Virus Vector: An Excellent Gene Delivery Tool for CNS Disease Treatment." *Journal of Controlled Release: Official Journal of the Controlled Release Society* 333 (May): 129–38. https://doi.org/10.1016/j.jconrel.2021.03.029.

Chen, Xinhong, Sripriya Ravindra Kumar, Cameron D. Adams, Daping Yang, Tongtong Wang, Cynthia M. Arokiaraj, Damien A. Wolfe et al. 2022. "Engineered AAVs for Non-Invasive Functional Transgene Expression in Rodent and Non-Human Primate Central and Peripheral Nervous Systems." *Neuron*, 110(14), 2242-2257. https://doi.org/10.1016/j.neuron.2022.05.003

Chu, Wing Sum, and Joanne Ng. 2021. "Immunomodulation in Administration of RAAV: Preclinical and Clinical Adjuvant Pharmacotherapies." Frontiers in Immunology 12: 658038. https://doi.org/10.3389/fimmu.2021.658038.

Colella, Pasqualina, Giuseppe Ronzitti, and Federico Mingozzi. 2018. "Emerging Issues in AAV-Mediated *In vivo* Gene Therapy." *Molecular Therapy - Methods & Clinical Development* 8 (March): 87–104. https://doi.org/10.1016/j.omtm.2017.11.007.

Corder, Gregory, Biafra Ahanonu, Benjamin F. Grewe, Dong Wang, Mark J. Schnitzer, and Grégory Scherrer. 2019. “An Amygdalar Neural Ensemble That Encodes the Unpleasantness of Pain.” *Science (New York, N.Y.)* 363 (6424): 276–81. https://doi.org/10.1126/science.aap8586.

De Rubeis, Silvia, Xin He, Arthur P. Goldberg, Christopher S. Poultney, Kaitlin Samocha, A. Erucment Cicek, Yan Kou, et al. 2014. “Synaptic, Transcriptional and Chromatin Genes Disrupted in Autism.” *Nature* 515 (7526): 209–15. https://doi.org/10.1038/nature13772.

Deverman, Benjamin E., Bernard M. Ravina, Krystof S. Bankiewicz, Steven M. Paul, and Dinah W. Y. Sah. 2018. “Gene Therapy for Neurological Disorders: Progress and Prospects.” *Nature Reviews Drug Discovery* 17 (9): 641–59. https://doi.org/10.1038/nrd.2018.110.

Deverman, Benjamin E., Piers L. Pravdo, Bryan P. Simpson, Sripriya Ravindra Kumar, Ken Y. Chan, Abhik Banerjee, Wei-Li Wu, et al. 2016. “Cre-Dependent Selection Yields AAV Variants for Widespread Gene Transfer to the Adult Brain.” *Nature Biotechnology* 34 (2): 204–9. https://doi.org/10.1038/nbt.3440.

DiMattia, Michael A., Hyun-Joo Nam, Kim Van Vliet, Matthew Mitchell, Antonette Bennett, Brittney L. Gurda, Robert McKenna, et al. 2012. “Structural Insight into the Unique Properties of Adeno-Associated Virus Serotype 9.” *Journal of Virology* 86 (12): 6947–58. https://doi.org/10.1128/JVI.07232-11.

Dong, Chunyang, Yu Zheng, Kiran Long-Iyer, Emily C. Wright, Yulong Li, and Lin Tian. 2022. “Fluorescence Imaging of Neural Activity, Neurochemical Dynamics, and Drug-Specific Receptor Conformation with Genetically Encoded Sensors.” *Annual Review of Neuroscience* 45 (1): 273–94. https://doi.org/10.1146/annurev-neuro-110520-031137.

Draxler, Peter, Aurora Moen, Karolina Galek, Ani Boghos, Dariga Ramazanova, and Jürgen Sandkühler. 2021. “Spontaneous, Voluntary, and Affective Behaviours in Rat Models of Pathological Pain.” *Frontiers in Pain Research* 2: 23. https://doi.org/10.3389/fpain.2021.672711.

Duan, Yangyang, Tao Ye, Zhe Qu, Yuewen Chen, Abigail Miranda, Xiaopu Zhou, Ka-Chun

Lok, et al. 2021. “Brain-Wide Cas9-Mediated Cleavage of a Gene Causing Familial Alzheimer’s Disease Alleviates Amyloid-Related Pathologies in Mice.” *Nature Biomedical Engineering*, July, 1–13. https://doi.org/10.1038/s41551-021-00759-0.

Fenno, Lief, Ofer Yizhar, and Karl Deisseroth. 2011. “The Development and Application of Optogenetics.” *Annual Review of Neuroscience* 34 (1): 389–412. https://doi.org/10.1146/annurev-neuro-061010-113817.

Foust, Kevin D., Emily Nurre, Chrystal L. Montgomery, Anna Hernandez, Curtis M. Chan, and Brian K. Kaspar. 2009. “Intravascular AAV9 Preferentially Targets Neonatal Neurons and Adult Astrocytes.” *Nature Biotechnology* 27 (1): 59–65. https://doi.org/10.1038/nbt.1515.

Geisler, A., A. Jungmann, J. Kurreck, W. Poller, H. A. Katus, R. Vetter, H. Fechner, and O. J. Müller. 2011. “MicroRNA122-Regulated Transgene Expression Increases Specificity of Cardiac Gene Transfer upon Intravenous Delivery of AAV9 Vectors.” *Gene Therapy* 18 (2): 199–209. https://doi.org/10.1038/gt.2010.141.

Geisler, Anja, and Henry Fechner. 2016. “MicroRNA-Regulated Viral Vectors for Gene Therapy.” *World Journal of Experimental Medicine* 6 (2): 37–54. https://doi.org/10.5493/wjem.v6.i2.37.

George, Lindsey A., Margaret V. Ragni, John E. J. Rasko, Leslie J. Raffini, Benjamin J. Samelson-Jones, Margareth Ozelo, Maria Hazbon, et al. 2020. “Long-Term Follow-Up of the First in Human Intravascular Delivery of AAV for Gene Transfer: AAV2-HFIX16 for Severe Hemophilia B.” *Molecular Therapy* 28 (9): 2073–82. https://doi.org/10.1016/j.ymthe.2020.06.001.

Giovannucci, Andrea, Johannes Friedrich, Pat Gunn, Jérémie Kalfon, Brandon L. Brown, Sue Ann Koay, Jiannis Taxidis, et al. 2019. “CaImAn an Open Source Tool for Scalable Calcium Imaging Data Analysis.” *ELife* 8 (January): e38173. https://doi.org/10.7554/eLife.38173.

Giusti, Sebastian A., Claudia A. Vercelli, Annette M. Vogl, Adam W. Kolarz, Natalia S. Pino, Jan M. Deussing, and Damian Refojo. 2014. “Behavioral Phenotyping of Nestin-Cre Mice: Implications for Genetic Mouse Models of Psychiatric Disorders.”

Journal of Psychiatric Research 55 (August): 87–95. https://doi.org/10.1016/j.jpsychires.2014.04.002.

Goertsen, David, Nicholas C. Flytzanis, Nick Goeden, Miguel R. Chuapoco, Alexander Cummins, Yijing Chen, Yingying Fan, et al. 2021. "AAV Capsid Variants with Brain-Wide Transgene Expression and Decreased Liver Targeting after Intravenous Delivery in Mouse and Marmoset." *Nature Neuroscience*, December. https://doi.org/10.1038/s41593-021-00969-4.

Golebiowski, Diane, Imramsjah M. J. van der Bom, Churl-Su Kwon, Andrew D. Miller, Keiko Petrosky, Allison M. Bradbury, Stacy Maitland, et al. 2017. "Direct Intracranial Injection of AAVrh8 Encoding Monkey β-N-Acetylhexosaminidase Causes Neurotoxicity in the Primate Brain." *Human Gene Therapy* 28 (6): 510–22. https://doi.org/10.1089/hum.2016.109.

Gombash, S. E., C. J. Cowley, J. A. Fitzgerald, C. A. Lepak, M. G. Neides, K. Hook, L. J. Todd, et al. 2017. "Systemic Gene Delivery Transduces the Enteric Nervous System of Guinea Pigs and Cynomolgus Macaques." *Gene Therapy* 24 (10): 640–48. https://doi.org/10.1038/gt.2017.72.

Gong, Xin, Diego Mendoza-Halliday, Jonathan T. Ting, Tobias Kaiser, Xuyun Sun, André M. Bastos, Ralf D. Wimmer, et al. 2020. "An Ultra-Sensitive Step-Function Opsin for Minimally Invasive Optogenetic Stimulation in Mice and Macaques." *Neuron* 107 (1): 38-51.e8. https://doi.org/10.1016/j.neuron.2020.03.032.

Gore, Reshma, Maureen S. Riedl, Kelley F. Kitto, Carolyn A. Fairbanks, and Lucy Vulchanova. 2019. "AAV-Mediated Gene Delivery to the Enteric Nervous System by Intracolonic Injection." *Methods in Molecular Biology (Clifton, N.J.)* 1950: 407–15. https://doi.org/10.1007/978-1-4939-9139-6_24.

Gray, Steven J, Kenton T Woodard, and R Jude Samulski. 2010. "Viral Vectors and Delivery Strategies for CNS Gene Therapy." *Therapeutic Delivery* 1 (4): 517–34.

Gray, Steven J. 2016. "Timing of Gene Therapy Interventions: The Earlier, the Better." *Molecular Therapy* 24 (6): 1017–18. https://doi.org/10.1038/mt.2016.20.

Greig, Jenny A., Camilo Breton, Kelly M. Martins, Yanqing Zhu, Zhenning He, John White, Peter Bell, Lili Wang, and James M. Wilson. 2022. "Loss of Transgene Expression

Limits Liver Gene Therapy in Primates." *bioRxiv*. https://doi.org/10.1101/2022.03.24.485675.

Grødem, Sverre, Ingeborg Nymoen, Guro Helén Vatne, Valgerdur Björnsdottir, Kristian Kinden Lensjø, and Marianne Fyhn. 2021. "An Updated Suite of Viral Vectors for *in vivo* Calcium Imaging Using Local and Retro-Orbital Injections." *BioRxiv*, January, 2021.05.14.443815. https://doi.org/10.1101/2021.05.14.443815.

GuhaSarkar, Dwijit, James Neiswender, Qin Su, Guangping Gao, and Miguel Sena-Esteves. 2017. "Intracranial AAV-IFN-β Gene Therapy Eliminates Invasive Xenograft Glioblastoma and Improves Survival in Orthotopic Syngeneic Murine Model." *Molecular Oncology* 11 (2): 180–93. https://doi.org/10.1002/1878-0261.12020.

Haery, Leila, Benjamin E. Deverman, Katherine S. Matho, Ali Cetin, Kenton Woodard, Connie Cepko, Karen I. Guerin, et al. 2019. "Adeno-Associated Virus Technologies and Methods for Targeted Neuronal Manipulation." *Frontiers in Neuroanatomy* 13: 93. https://doi.org/10.3389/fnana.2019.00093.

Hamilton, Bradley A., and J. Fraser Wright. 2021. "Challenges Posed by Immune Responses to AAV Vectors: Addressing Root Causes." *Frontiers in Immunology* 12. https://www.frontiersin.org/article/10.3389/fimmu.2021.675897.

Hanlon, Killian S., Jonah C. Meltzer, Tetyana Buzhdygan, Ming J. Cheng, Miguel Sena-Esteves, Rachel E. Bennett, Timothy P. Sullivan, et al. 2019. "Selection of an Efficient AAV Vector for Robust CNS Transgene Expression." *Molecular Therapy. Methods & Clinical Development* 15 (December): 320–32. https://doi.org/10.1016/j.omtm.2019.10.007.

Hinderer, Christian, Nathan Katz, Elizabeth L. Buza, Cecilia Dyer, Tamara Goode, Peter Bell, Laura K. Richman, and James M. Wilson. 2018. "Severe Toxicity in Nonhuman Primates and Piglets Following High-Dose Intravenous Administration of an Adeno-Associated Virus Vector Expressing Human SMN." *Human Gene Therapy* 29 (3): 285–98. https://doi.org/10.1089/hum.2018.015.

Hirai, Takashi, Mitsuhiro Enomoto, Akira Machida, Mariko Yamamoto, Hiroya Kuwahara, Mio Tajiri, Yukihiko Hirai, et al. 2012. "Intrathecal ShRNA-AAV9 Inhibits Target Protein Expression in the Spinal Cord and Dorsal Root Ganglia of Adult Mice."

Human Gene Therapy Methods 23 (2): 119–27. https://doi.org/10.1089/hgtb.2012.035.

Homs, J., L. Ariza, G. Pagès, E. Udina, X. Navarro, M. Chillón, and A. Bosch. 2011. "Schwann Cell Targeting via Intrasciatic Injection of AAV8 as Gene Therapy Strategy for Peripheral Nerve Regeneration." *Gene Therapy* 18 (6): 622–30. https://doi.org/10.1038/gt.2011.7.

Hordeaux, Juliette, Qiang Wang, Nathan Katz, Elizabeth L. Buza, Peter Bell, and James M. Wilson. 2018. "The Neurotropic Properties of AAV-PHP.B Are Limited to C57BL/6J Mice." *Molecular Therapy* 26 (3): 664–68. https://doi.org/10.1016/j.ymthe.2018.01.018.

Hordeaux, Juliette, Yuan Yuan, Peter M. Clark, Qiang Wang, R. Alexander Martino, Joshua J. Sims, Peter Bell, Angela Raymond, William L. Stanford, and James M. Wilson. 2019. "The GPI-Linked Protein LY6A Drives AAV-PHP.B Transport across the Blood-Brain Barrier." *Molecular Therapy: The Journal of the American Society of Gene Therapy* 27 (5): 912–21. https://doi.org/10.1016/j.ymthe.2019.02.013.

Huang, Lan, Jie Wan, Yinqiu Wu, Yu Tian, Yizheng Yao, Shun Yao, Xiaoyun Ji, Shengjun Wang, Zhaoliang Su, and Huaxi Xu. 2021. "Challenges in Adeno-Associated Virus-Based Treatment of Central Nervous System Diseases through Systemic Injection." *Life Sciences* 270 (April): 119142. https://doi.org/10.1016/j.lfs.2021.119142.

Huang, Qin, Ken Y. Chan, Isabelle G. Tobey, Yujia Alina Chan, Tim Poterba, Christine L. Boutros, Alejandro B. Balazs, et al. 2019. "Delivering Genes across the Blood-Brain Barrier: LY6A, a Novel Cellular Receptor for AAV-PHP.B Capsids." *PloS One* 14 (11): e0225206. https://doi.org/10.1371/journal.pone.0225206.

Hudry, Eloise, and Luk H. Vandenberghe. 2019. "Therapeutic AAV Gene Transfer to the Nervous System: A Clinical Reality." *Neuron* 101 (5): 839–62. https://doi.org/10.1016/j.neuron.2019.02.017.

Ingusci, Selene, Gianluca Verlengia, Marie Soukupova, Silvia Zucchini, and Michele Simonato. 2019. "Gene Therapy Tools for Brain Diseases." *Frontiers in Pharmacology* 10: 724. https://doi.org/10.3389/fphar.2019.00724.

Ippolito, Dominic M., and Cagla Eroglu. 2010. "Quantifying Synapses: An

Immunocytochemistry-Based Assay to Quantify Synapse Number.” *Journal of Visualized Experiments: JoVE*, no. 45 (November): 2270. https://doi.org/10.3791/2270.

Isakova, Alina, Tobias Fehlmann, Andreas Keller, and Stephen R. Quake. 2020. “A Mouse Tissue Atlas of Small Noncoding RNA.” *Proceedings of the National Academy of Sciences* 117 (41): 25634–45. https://doi.org/10.1073/pnas.2002277117.

Jennings, Charles G., Rogier Landman, Yang Zhou, Jitendra Sharma, Julia Hyman, J. Anthony Movshon, Zilong Qiu, et al. 2016. “Opportunities and Challenges in Modeling Human Brain Disorders in Transgenic Primates.” *Nature Neuroscience* 19 (9): 1123–30. https://doi.org/10.1038/nn.4362.

Jiman, Ahmad A., David C. Ratze, Elissa J. Welle, Paras R. Patel, Julianna M. Richie, Elizabeth C. Bottorff, John P. Seymour, Cynthia A. Chestek, and Tim M. Bruns. 2020. “Multi-Channel Intraneural Vagus Nerve Recordings with a Novel High-Density Carbon Fiber Microelectrode Array.” *Scientific Reports* 10 (1): 15501. https://doi.org/10.1038/s41598-020-72512-7.

Kähler, Anna K., Srdjan Djurovic, Bettina Kulle, Erik G. Jönsson, Ingrid Agartz, Håkan Hall, Stein Opjordsmoen, et al. 2008. “Association Analysis of Schizophrenia on 18 Genes Involved in Neuronal Migration: MDGA1 as a New Susceptibility Gene.” *American Journal of Medical Genetics. Part B, Neuropsychiatric Genetics: The Official Publication of the International Society of Psychiatric Genetics* 147B (7): 1089–1100. https://doi.org/10.1002/ajmg.b.30726.

Kimura, Seigo, and Hideyoshi Harashima. 2020. “Current Status and Challenges Associated with CNS-Targeted Gene Delivery across the BBB.” *Pharmaceutics* 12 (12): 1216. https://doi.org/10.3390/pharmaceutics12121216.

Kisanuki, Yaz Y., Robert E. Hammer, Jun-ichi Miyazaki, S.Clay Williams, James A. Richardson, and Masashi Yanagisawa. 2001. “Tie2-Cre Transgenic Mice: A New Model for Endothelial Cell-Lineage Analysis *in vivo*.” *Developmental Biology* 230 (2): 230–42. https://doi.org/10.1006/dbio.2000.0106.

Körbelin, Jakob, Godwin Dogbevia, Stefan Michelfelder, Dirk A Ridder, Agnes Hunger, Jan Wenzel, Henning Seismann, et al. 2016. “A Brain Microvasculature Endothelial

Cell-specific Viral Vector with the Potential to Treat Neurovascular and Neurological Diseases.” *EMBO Molecular Medicine* 8 (6): 609–25. https://doi.org/10.15252/emmm.201506078.

Krashes, Michael J., Shuichi Koda, ChianPing Ye, Sarah C. Rogan, Andrew C. Adams, Daniel S. Cusher, Eleftheria Maratos-Flier, Bryan L. Roth, and Bradford B. Lowell. 2011. “Rapid, Reversible Activation of AgRP Neurons Drives Feeding Behavior in Mice.” *The Journal of Clinical Investigation* 121 (4): 1424–28. https://doi.org/10.1172/JCI46229.

Krolak, Trevor, Ken Y. Chan, Luke Kaplan, Qin Huang, Jason Wu, Qingxia Zheng, Velina Kozareva et al. “A high-efficiency AAV for endothelial cell transduction throughout the central nervous system.” *Nature Cardiovascular Research* 1, no. 4 (2022): 389-400.

Kucukdereli, Hakan, Nicola J. Allen, Anthony T. Lee, Ava Feng, M. Ilcim Ozlu, Laura M. Conatser, Chandrani Chakraborty, et al. 2011. “Control of Excitatory CNS Synaptogenesis by Astrocyte-Secreted Proteins Hevin and SPARC.” *Proceedings of the National Academy of Sciences of the United States of America* 108 (32): E440-449. https://doi.org/10.1073/pnas.1104977108.

Lau, Cia-Hin, Jonathan Weng-Thim Ho, Pik Kwan Lo, and Chung Tin. 2019. “Targeted Transgene Activation in the Brain Tissue by Systemic Delivery of Engineered AAV1 Expressing CRISPRa.” *Molecular Therapy. Nucleic Acids* 16 (June): 637–49. https://doi.org/10.1016/j.omtn.2019.04.015.

Levy, Jonathan M., Wei-Hsi Yeh, Nachiket Pendse, Jessie R. Davis, Erin Hennessey, Rossano Butcher, Luke W. Koblan, Jason Comander, Qin Liu, and David R. Liu. 2020. “Cytosine and Adenine Base Editing of the Brain, Liver, Retina, Heart and Skeletal Muscle of Mice via Adeno-Associated Viruses.” *Nature Biomedical Engineering* 4 (1): 97–110. https://doi.org/10.1038/s41551-019-0501-5.

Li, Xuefeng, Xiaoli Wei, Jinduan Lin, and Li Ou. 2022. “A Versatile Toolkit for Overcoming AAV Immunity.” *Frontiers in Immunology* 13. https://www.frontiersin.org/articles/10.3389/fimmu.2022.991832.

Liguore, William A., Jacqueline S. Domire, Dana Button, Yun Wang, Brett D. Dufour, Sathya Srinivasan, and Jodi L. McBride. 2019. “AAV-PHP.B Administration Results in a Differential Pattern of CNS Biodistribution in Non-Human Primates Compared with Mice.” *Molecular Therapy* 27 (11): 2018–37. https://doi.org/10.1016/j.ymthe.2019.07.017.

Lindblom, Per, Holger Gerhardt, Stefan Liebner, Alexandra Abramsson, Maria Enge, Mats Hellstrom, Gudrun Backstrom, et al. 2003. “Endothelial PDGF-B Retention Is Required for Proper Investment of Pericytes in the Microvessel Wall.” *Genes & Development* 17 (15): 1835–40. https://doi.org/10.1101/gad.266803.

Lloyd-Burton, Samantha, and A. Jane Roskams. 2012. “SPARC-like 1 (SC1) Is a Diversely Expressed and Developmentally Regulated Matricellular Protein That Does Not Compensate for the Absence of SPARC in the CNS.” *The Journal of Comparative Neurology* 520 (12): 2575–90. https://doi.org/10.1002/cne.23029.

Lykken, Erik Allen, Charles Shyng, Reginald James Edwards, Alejandra Rozenberg, and Steven James Gray. 2018. “Recent Progress and Considerations for AAV Gene Therapies Targeting the Central Nervous System.” *Journal of Neurodevelopmental Disorders* 10 (1): 16. https://doi.org/10.1186/s11689-018-9234-0.

Mäe, Maarja A., Liqun He, Sofia Nordling, Elisa Vazquez-Liebanas, Khayrun Nahar, Bongnam Jung, Xidan Li, et al. 2021. “Single-Cell Analysis of Blood-Brain Barrier Response to Pericyte Loss.” *Circulation Research* 128 (4): e46–62. https://doi.org/10.1161/CIRCRESAHA.120.317473.

Majowicz, Anna, David Salas, Nerea Zabaleta, Estefania Rodríguez-Garcia, Gloria González-Aseguinolaza, Harald Petry, and Valerie Ferreira. 2017. “Successful Repeated Hepatic Gene Delivery in Mice and Non-Human Primates Achieved by Sequential Administration of AAV5ch and AAV1.” *Molecular Therapy* 25 (8): 1831–42. https://doi.org/10.1016/j.ymthe.2017.05.003.

Martino, R. Alexander, Edwin C. Fluck, Jacqueline Murphy, Qiang Wang, Henry Hoff, Ruth A. Pumroy, Claudia Y. Lee, et al. 2021. “Context-Specific Function of the Engineered Peptide Domain of PHP.B.” *Journal of Virology* 95 (20): e0116421. https://doi.org/10.1128/JVI.01164-21.

Marvaldi, Letizia, Nicolas Panayotis, Stefanie Alber, Shachar Y. Dagan, Nataliya

Okladnikov, Indrek Koppel, Agostina Di Pizio, et al. 2020. “Importin A3 Regulates Chronic Pain Pathways in Peripheral Sensory Neurons.” *Science* 369 (6505): 842–46. https://doi.org/10.1126/science.aaz5875.

Marx, Vivien. 2016. “Neurobiology: Learning from Marmosets.” *Nature Methods* 13 (11): 911–16. https://doi.org/10.1038/nmeth.4036.

Masselink, Wouter, Daniel Reumann, Prayag Murawala, Pawel Pasierbek, Yuka Taniguchi, François Bonnay, Katharina Meixner, Jürgen A. Knoblich, and Elly M. Tanaka. 2019. “Broad Applicability of a Streamlined Ethyl Cinnamate-Based Clearing Procedure.” *Development (Cambridge, England)* 146 (3): dev166884. https://doi.org/10.1242/dev.166884.

Matsuzaki, Yasunori, Ayumu Konno, Ryuta Mochizuki, Yoichiro Shinohara, Keisuke Nitta, Yukihiro Okada, and Hirokazu Hirai. 2018. “Intravenous Administration of the Adeno-Associated Virus-PHP.B Capsid Fails to Upregulate Transduction Efficiency in the Marmoset Brain.” *Neuroscience Letters* 665: 182–88. https://doi.org/10.1016/j.neulet.2017.11.049.

Matsuzaki, Yasunori, Ayumu Konno, Ryuta Mochizuki, Yoichiro Shinohara, Keisuke Nitta, Yukihiro Okada, and Hirokazu Hirai. 2018. “Intravenous Administration of the Adeno-Associated Virus-PHP.B Capsid Fails to Upregulate Transduction Efficiency in the Marmoset Brain.” *Neuroscience Letters* 665: 182–88. https://doi.org/10.1016/j.neulet.2017.11.049.

Matsuzaki, Yasunori, Masami Tanaka, Sachiko Hakoda, Tatsuki Masuda, Ryota Miyata, Ayumu Konno, and Hirokazu Hirai. 2019. “Neurotropic Properties of AAV-PHP.B Are Shared among Diverse Inbred Strains of Mice.” *Molecular Therapy* 27 (4): 700–704. https://doi.org/10.1016/j.ymthe.2019.02.016.

Mayerich, D., L. Abbott, and B. McCormick. 2008. “Knife-Edge Scanning Microscopy for Imaging and Reconstruction of Three-Dimensional Anatomical Structures of the Mouse Brain.” *Journal of Microscopy* 231 (Pt 1): 134–43. https://doi.org/10.1111/j.1365-2818.2008.02024.x.

McInnes, Leland, John Healy, and James Melville. 2020. “UMAP: Uniform Manifold Approximation and Projection for Dimension Reduction.” *ArXiv:1802.03426 [Cs,* *Stat]*, September. http://arxiv.org/abs/1802.03426.

Michelson, Nicholas J., Matthieu P. Vanni, and Timothy H. Murphy. 2019. "Comparison between Transgenic and AAV-PHP.EB-Mediated Expression of GCaMP6s Using *in vivo* Wide-Field Functional Imaging of Brain Activity." *Neurophotonics* 6 (2): 025014. https://doi.org/10.1117/1.NPh.6.2.025014.

Miller, Cory T., Winrich A. Freiwald, David A. Leopold, Jude F. Mitchell, Afonso C. Silva, and Xiaoqin Wang. 2016. "Marmosets: A Neuroscientific Model of Human Social Behavior." *Neuron* 90 (2): 219–33. https://doi.org/10.1016/j.neuron.2016.03.018.

Mingozzi, Federico, and Katherine A. High. 2017. "Overcoming the Host Immune Response to Adeno-Associated Virus Gene Delivery Vectors: The Race Between Clearance, Tolerance, Neutralization, and Escape." *Annual Review of Virology* 4 (1): 511–34. https://doi.org/10.1146/annurev-virology-101416-041936.

Mishra, Santosh K., Sarah M. Tisel, Peihan Orestes, Sonia K. Bhangoo, and Mark A. Hoon. 2011. "TRPV1-Lineage Neurons Are Required for Thermal Sensation." *The EMBO Journal* 30 (3): 582–93. https://doi.org/10.1038/emboj.2010.325.

Mongrédien, Raphaële, Amaia M. Erdozain, Sylvie Dumas, Laura Cutando, Amaia Nuñez Del Moral, Emma Puighermanal, Sara Rezai Amin, et al. 2019. "Cartography of Hevin-Expressing Cells in the Adult Brain Reveals Prominent Expression in Astrocytes and Parvalbumin Neurons." *Brain Structure & Function* 224 (3): 1219–44. https://doi.org/10.1007/s00429-019-01831-x.

Monteys, Alex Mas, Amiel A. Hundley, Paul T. Ranum, Luis Tecedor, Amy Muehlmatt, Euyn Lim, Dmitriy Lukashev, Rajeev Sivasankaran, and Beverly L. Davidson. 2021. "Regulated Control of Gene Therapies by Drug-Induced Splicing." *Nature* 596 (7871): 291–95. https://doi.org/10.1038/s41586-021-03770-2.

Nonnenmacher, Mathieu, Wei Wang, Matthew A. Child, Xiao-Qin Ren, Carol Huang, Amy Zhen Ren, Jenna Tocci, et al. 2021. "Rapid Evolution of Blood-Brain-Barrier-Penetrating AAV Capsids by RNA-Driven Biopanning." *Molecular Therapy. Methods & Clinical Development* 20 (March): 366–78. https://doi.org/10.1016/j.omtm.2020.12.006.

O'Carroll, Simon J., William H. Cook, and Deborah Young. 2021. "AAV Targeting of Glial

Cell Types in the Central and Peripheral Nervous System and Relevance to Human Gene Therapy." *Frontiers in Molecular Neuroscience* 13: 256. https://doi.org/10.3389/fnmol.2020.618020.

Oh, Seung Wook, Julie A. Harris, Lydia Ng, Brent Winslow, Nicholas Cain, Stefan Mihalas, Quanxin Wang, et al. 2014. "A Mesoscale Connectome of the Mouse Brain." *Nature* 508 (7495): 207–14. https://doi.org/10.1038/nature13186.

Ojala, David S., Sabrina Sun, Jorge L. Santiago-Ortiz, Mikhail G. Shapiro, Philip A. Romero, and David V. Schaffer. 2018. "*In vivo* Selection of a Computationally Designed SCHEMA AAV Library Yields a Novel Variant for Infection of Adult Neural Stem Cells in the SVZ." *Molecular Therapy: The Journal of the American Society of Gene Therapy* 26 (1): 304–19. https://doi.org/10.1016/j.ymthe.2017.09.006.

Pena, Stefanie A., Rahul Iyengar, Rebecca S. Eshraghi, Nicole Bencie, Jeenu Mittal, Abdulrahman Aljohani, Rahul Mittal, and Adrien A. Eshraghi. 2020. "Gene Therapy for Neurological Disorders: Challenges and Recent Advancements." *Journal of Drug Targeting* 28 (2): 111–28. https://doi.org/10.1080/1061186X.2019.1630415.

Pietersz, Kimberly L., Francois Du Plessis, Stephan M. Pouw, Jolanda M. Liefhebber, Sander J. van Deventer, Gerard J. M. Martens, Pavlina S. Konstantinova, and Bas Blits. 2021. "PhP.B Enhanced Adeno-Associated Virus Mediated-Expression Following Systemic Delivery or Direct Brain Administration." *Frontiers in Bioengineering and Biotechnology* 9: 679483. https://doi.org/10.3389/fbioe.2021.679483.

Piguet, Françoise, Timothée de Saint Denis, Emilie Audouard, Kevin Beccaria, Arthur André, Guillaume Wurtz, Raphael Schatz, et al. 2021. "The Challenge of Gene Therapy for Neurological Diseases: Strategies and Tools to Achieve Efficient Delivery to the Central Nervous System." *Human Gene Therapy* 32 (7–8): 349–74. https://doi.org/10.1089/hum.2020.105.

Pogorzala, Leah A., Santosh K. Mishra, and Mark A. Hoon. 2013. "The Cellular Code for Mammalian Thermosensation." The Journal of Neuroscience: The Official Journal of the Society for Neuroscience 33 (13): 5533–41. https://doi.org/10.1523/JNEUROSCI.5788-12.2013.

Ponder, Katherine P., and Mark E. Haskins. 2007. "Gene Therapy for Mucopolysaccharidosis." *Expert Opinion on Biological Therapy* 7 (9): 1333–45. https://doi.org/10.1517/14712598.7.9.1333.

Privolizzi, Riccardo, Wing Sum Chu, Maha Tijani, and Joanne Ng. 2021. "Viral Gene Therapy for Paediatric Neurological Diseases: Progress to Clinical Reality." *Developmental Medicine & Child Neurology* 63 (9): 1019–29. https://doi.org/10.1111/dmcn.14885.

Profaci, Caterina P., Roeben N. Munji, Robert S. Pulido, and Richard Daneman. 2020. "The Blood-Brain Barrier in Health and Disease: Important Unanswered Questions." *The Journal of Experimental Medicine* 217 (4): e20190062. https://doi.org/10.1084/jem.20190062.

Pulicherla, Nagesh, Shen Shen, Swati Yadav, Kari Debbink, Lakshmanan Govindasamy, Mavis Agbandje-McKenna, and Aravind Asokan. 2011. "Engineering Liver-Detargeted AAV9 Vectors for Cardiac and Musculoskeletal Gene Transfer." *Molecular Therapy* 19 (6): 1070–78. https://doi.org/10.1038/mt.2011.22.

Purcell, A. E., O. H. Jeon, A. W. Zimmerman, M. E. Blue, and J. Pevsner. 2001. "Postmortem Brain Abnormalities of the Glutamate Neurotransmitter System in Autism." *Neurology* 57 (9): 1618–28. https://doi.org/10.1212/wnl.57.9.1618.

Ragan, Timothy, Lolahon R. Kadiri, Kannan Umadevi Venkataraju, Karsten Bahlmann, Jason Sutin, Julian Taranda, Ignacio Arganda-Carreras, Yongsoo Kim, H. Sebastian Seung, and Pavel Osten. 2012. "Serial two-photon tomography for automated ex vivo mouse brain imaging." *Nature Methods* 9, 255-258. https://doi.org/10.1038/nmeth.1854.

Ravagli, Enrico, Svetlana Mastitskaya, Nicole Thompson, Francesco Iacoviello, Paul R. Shearing, Justin Perkins, Alexander V. Gourine, Kirill Aristovich, and David Holder. 2020. "Imaging Fascicular Organization of Rat Sciatic Nerves with Fast Neural Electrical Impedance Tomography." *Nature Communications* 11 (1): 6241. https://doi.org/10.1038/s41467-020-20127-x.

Ravi, Bhavya, Michelle Harran Chan-Cortés, and Charlotte J. Sumner. 2021. "Gene-Targeting Therapeutics for Neurological Disease: Lessons Learned from Spinal

Muscular Atrophy." *Annual Review of Medicine* 72 (1): 1–14. https://doi.org/10.1146/annurev-med-070119-115459.

Ravindra Kumar, Sripriya, Timothy F. Miles, Xinhong Chen, David Brown, Tatyana Dobreva, Qin Huang, Xiaozhe Ding, et al. 2020. "Multiplexed Cre-Dependent Selection Yields Systemic AAVs for Targeting Distinct Brain Cell Types." *Nature Methods* 17 (5): 541–50. https://doi.org/10.1038/s41592-020-0799-7.

Reynaud-Dulaurier, Robin, and Michael Decressac. 2020. "PHP.B/EB Vectors Bring New Successes to Gene Therapy for Brain Diseases." *Frontiers in Bioengineering and Biotechnology* 8: 1137. https://doi.org/10.3389/fbioe.2020.582979.

Risher, W. Christopher, Sagar Patel, Il Hwan Kim, Akiyoshi Uezu, Srishti Bhagat, Daniel K. Wilton, Louis-Jan Pilaz, et al. 2014. "Astrocytes Refine Cortical Connectivity at Dendritic Spines." *ELife* 3 (December). https://doi.org/10.7554/eLife.04047.

Rivière, C., O. Danos, and A. M. Douar. 2006. "Long-Term Expression and Repeated Administration of AAV Type 1, 2 and 5 Vectors in Skeletal Muscle of Immunocompetent Adult Mice." *Gene Therapy* 13 (17): 1300–1308. https://doi.org/10.1038/sj.gt.3302766.

Romero, Philip A., and Frances H. Arnold. 2009. "Exploring Protein Fitness Landscapes by Directed Evolution." *Nature Reviews Molecular Cell Biology* 10 (12): 866–76. https://doi.org/10.1038/nrm2805.

Ronzitti, Giuseppe, David-Alexandre Gross, and Federico Mingozzi. 2020. "Human Immune Responses to Adeno-Associated Virus (AAV) Vectors." *Frontiers in Immunology* 11 (April): 670. https://doi.org/10.3389/fimmu.2020.00670.

Rossi, Jari, Nina Balthasar, David Olson, Michael Scott, Eric Berglund, Charlotte E. Lee, Michelle J. Choi, Danielle Lauzon, Bradford B. Lowell, and Joel K. Elmquist. 2011. "Melanocortin-4 Receptors Expressed by Cholinergic Neurons Regulate Energy Balance and Glucose Homeostasis." *Cell Metabolism* 13 (2): 195–204. https://doi.org/10.1016/j.cmet.2011.01.010.

Sawamoto, Kazuki, Hui-Hsuan Chen, Carlos J. Alméciga-Díaz, Robert W. Mason, and Shunji Tomatsu. 2018. “Gene Therapy for Mucopolysaccharidoses.” *Molecular Genetics and Metabolism* 123 (2): 59–68. https://doi.org/10.1016/j.ymgme.2017.12.434.

Sevin, Caroline, and Kumaran Deiva. 2021. “Clinical Trials for Gene Therapy in Lysosomal Diseases With CNS Involvement.” *Frontiers in Molecular Biosciences* 8: 624988. https://doi.org/10.3389/fmolb.2021.624988.

Shen, Shen, Kelli D. Bryant, Junjiang Sun, Sarah M. Brown, Andrew Troupes, Nagesh Pulicherla, and Aravind Asokan. 2012. “Glycan Binding Avidity Determines the Systemic Fate of Adeno-Associated Virus Type 9.” *Journal of Virology* 86 (19): 10408–17. https://doi.org/10.1128/JVI.01155-12.

Singh, Sandeep K., Jeff A. Stogsdill, Nisha S. Pulimood, Hayley Dingsdale, Yong Ho Kim, Louis-Jan Pilaz, Il Hwan Kim, et al. 2016. “Astrocytes Assemble Thalamocortical Synapses by Bridging Nrx1α and NL1 via Hevin.” *Cell* 164 (0): 183–96. https://doi.org/10.1016/j.cell.2015.11.034.

Stanimirovic, Danica B., Jagdeep K. Sandhu, and Will J. Costain. 2018. “Emerging Technologies for Delivery of Biotherapeutics and Gene Therapy Across the Blood-Brain Barrier.” *BioDrugs: Clinical Immunotherapeutics, Biopharmaceuticals and Gene Therapy* 32 (6): 547–59. https://doi.org/10.1007/s40259-018-0309-y.

Sternson, Scott M., and Bryan L. Roth. 2014. “Chemogenetic Tools to Interrogate Brain Functions.” *Annual Review of Neuroscience* 37 (1): 387–407. https://doi.org/10.1146/annurev-neuro-071013-014048.

Sundaram, Sivaraj M., Adriana Arrulo Pereira, Hannes Köpke, Helge Müller-Fielitz, Meri De Angelis, Timo D. Müller, Heike Heuer et al. 2021 "Gene therapy targeting the blood-brain barrier improves neurological symptoms in a model of genetic MCT8 deficiency." *bioRxiv*. https://doi.org/10.1101/2021.12.05.471343.

Takano, Tetsuya, John T. Wallace, Katherine T. Baldwin, Alicia M. Purkey, Akiyoshi Uezu, Jamie L. Courtland, Erik J. Soderblom, et al. 2020. “Chemico-Genetic Discovery of Astrocytic Control of Inhibition *in vivo*.” *Nature* 588 (7837): 296–302. https://doi.org/10.1038/s41586-020-2926-0.

Tan, Fangzhi, Cenfeng Chu, Jieyu Qi, Wenyan Li, Dan You, Ke Li, Xin Chen, et al. 2019. "AAV-Ie Enables Safe and Efficient Gene Transfer to Inner Ear Cells." *Nature Communications* 10 (1): 3733. https://doi.org/10.1038/s41467-019-11687-8.

Terstappen, Georg C., Axel H. Meyer, Robert D. Bell, and Wandong Zhang. 2021. "Strategies for Delivering Therapeutics across the Blood-Brain Barrier." *Nature Reviews. Drug Discovery* 20 (5): 362–83. https://doi.org/10.1038/s41573-021-00139-y.

Thakur, Kiran T., Emiliano Albanese, Panteleimon Giannakopoulos, Nathalie Jette, Mattias Linde, Martin J. Prince, Timothy J. Steiner, and Tarun Dua. 2016. "Neurological Disorders." In Mental, Neurological, and Substance Use Disorders: Disease Control Priorities, Third Edition (Volume 4), edited by Vikram Patel, Dan Chisholm, Tarun Dua, Ramanan Laxminarayan, and María Elena Medina-Mora. Washington (DC): The International Bank for Reconstruction and Development / The World Bank. http://www.ncbi.nlm.nih.gov/books/NBK361950/.

Ting, Jonathan T., Brian Kalmbach, Peter Chong, Rebecca de Frates, C. Dirk Keene, Ryder P. Gwinn, Charles Cobbs, et al. 2018. "A Robust Ex Vivo Experimental Platform for Molecular-Genetic Dissection of Adult Human Neocortical Cell Types and Circuits." *Scientific Reports* 8 (May): 8407. https://doi.org/10.1038/s41598-018-26803-9.

Tosolini, Andrew P., and George M. Smith. 2018. "Editorial: Gene Therapy for the Central and Peripheral Nervous System." *Frontiers in Molecular Neuroscience* 11: 54. https://doi.org/10.3389/fnmol.2018.00054.

Vogt, Christoph C., Tobias Bruegmann, Daniela Malan, Annika Ottersbach, Wilhelm Roell, Bernd K. Fleischmann, and Philipp Sasse. 2015. "Systemic Gene Transfer Enables Optogenetic Pacing of Mouse Hearts." *Cardiovascular Research* 106 (2): 338–43. https://doi.org/10.1093/cvr/cvv004.

Walters, Marie C., Martha J. Sonner, Jessica H. Myers, and David R. Ladle. 2019. "Calcium Imaging of Parvalbumin Neurons in the Dorsal Root Ganglia." *ENeuro* 6 (4): ENEURO.0349-18.2019. https://doi.org/10.1523/ENEURO.0349-18.2019.

Wang, Dan, Phillip W. L. Tai, and Guangping Gao. 2019. “Adeno-Associated Virus Vector as a Platform for Gene Therapy Delivery.” *Nature Reviews Drug Discovery* 18 (5): 358–78. https://doi.org/10.1038/s41573-019-0012-9.

Watakabe, Akiya, Masanari Ohtsuka, Masaharu Kinoshita, Masafumi Takaji, Kaoru Isa, Hiroaki Mizukami, Keiya Ozawa, Tadashi Isa, and Tetsuo Yamamori. 2015. “Comparative Analyses of Adeno-Associated Viral Vector Serotypes 1, 2, 5, 8 and 9 in Marmoset, Mouse and Macaque Cerebral Cortex.” *Neuroscience Research* 93 (April): 144–57. https://doi.org/10.1016/j.neures.2014.09.002.

Williams, Erika K., Rui B. Chang, David E. Strochlic, Benjamin D. Umans, Bradford B. Lowell, and Stephen D. Liberles. 2016. “Sensory Neurons That Detect Stretch and Nutrients in the Digestive System.” *Cell* 166 (1): 209–21. https://doi.org/10.1016/j.cell.2016.05.011.

Xiao, Minjia, Zhi Jie Xiao, Binbin Yang, Ziwei Lan, and Fang Fang. 2020. “Blood-Brain Barrier: More Contributor to Disruption of Central Nervous System Homeostasis Than Victim in Neurological Disorders.” *Frontiers in Neuroscience* 14: 764. https://doi.org/10.3389/fnins.2020.00764.

Yang, Andrew C., Ryan T. Vest, Fabian Kern, Davis P. Lee, Christina A. Maat, Patricia M. Losada, Michelle B. Chen, et al. 2022. “A Human Brain Vascular Atlas Reveals Diverse Mediators of Alzheimer’s Risk” *Nature* 603(7903).885-892. https://doi.org/10.1038/s41586-021-04369-3.

Yang, Bin, Shaoyong Li, Hongyan Wang, Yansu Guo, Dominic J Gessler, Chunyan Cao, Qin Su, et al. 2014. “Global CNS Transduction of Adult Mice by Intravenously Delivered RAAVrh.8 and RAAVrh.10 and Nonhuman Primates by RAAVrh.10.” *Molecular Therapy* 22 (7): 1299–1309. https://doi.org/10.1038/mt.2014.68.

Yang, Yiyuan, Mingzheng Wu, Abraham Vázquez-Guardado, Amy J. Wegener, Jose G. Grajales-Reyes, Yujun Deng, Taoyi Wang, et al. 2021. “Wireless Multilateral Devices for Optogenetic Studies of Individual and Social Behaviors.” *Nature Neuroscience* 24 (7): 1035–45. https://doi.org/10.1038/s41593-021-00849-x.

Yardeni, Tal, Michael Eckhaus, H. Douglas Morris, Marjan Huizing, and Shelley Hoogstraten-Miller. 2011. “Retro-Orbital Injections in Mice.” *Lab Animal* 40 (5):

155–60. https://doi.org/10.1038/laban0511-155.

Yu, Hongwei, Gregory Fischer, Lejla Ferhatovic, Fan Fan, Alan R. Light, Dorothee Weihrauch, Damir Sapunar, Hiroyuki Nakai, Frank Park, and Quinn H. Hogan. 2013. "Intraganglionic AAV6 Results in Efficient and Long-Term Gene Transfer to Peripheral Sensory Nervous System in Adult Rats." *PloS One* 8 (4): e61266. https://doi.org/10.1371/journal.pone.0061266.

Yu, Xing, Caihong Ji, and Anwen Shao. 2020. "Neurovascular Unit Dysfunction and Neurodegenerative Disorders." *Frontiers in Neuroscience* 14 (April): 334. https://doi.org/10.3389/fnins.2020.00334.

Zanos, Theodoros P., Harold A. Silverman, Todd Levy, Tea Tsaava, Emily Battinelli, Peter W. Lorraine, Jeffrey M. Ashe, Sangeeta S. Chavan, Kevin J. Tracey, and Chad E. Bouton. 2018. "Identification of Cytokine-Specific Sensory Neural Signals by Decoding Murine Vagus Nerve Activity." *Proceedings of the National Academy of Sciences* 115 (21): E4843–52. https://doi.org/10.1073/pnas.1719083115.

Zapolnik, Paweł, and Antoni Pyrkosz. 2021. "Gene Therapy for Mucopolysaccharidosis Type II—A Review of the Current Possibilities." *International Journal of Molecular Sciences* 22 (11): 5490. https://doi.org/10.3390/ijms22115490.

Zhang, Ran, Lin Cao, Mengtian Cui, Zixian Sun, Mingxu Hu, Rouxuan Zhang, William Stuart, et al. 2019. "Adeno-Associated Virus 2 Bound to Its Cellular Receptor AAVR." *Nature Microbiology* 4 (4): 675–82. https://doi.org/10.1038/s41564-018-0356-7.

Zhang, Yan; Rózsa, Márton; Bushey, Daniel; Zheng, Jihong; Reep, Daniel; Broussard, Gerard Joey; Tsang, Arthur; Tsegaye, Getahun; Patel, Ronak, et al. 2020. "jGCaMP8 Fast Genetically Encoded Calcium Indicators." *Janelia Research Campus*. Online resource. 10.25378/janelia.13148243.v1.

Zhao, Huimin, Lori Giver, Zhixin Shao, Joseph A. Affholter, and Frances H. Arnold. 1998. "Molecular Evolution by Staggered Extension Process (StEP) in Vitro Recombination." *Nature Biotechnology* 16 (3): 258–61. https://doi.org/10.1038/nbt0398-258.

Zhurov, Vladimir, John D. H. Stead, Zul Merali, Miklos Palkovits, Gabor Faludi, Caroline

Schild-Poulter, Hymie Anisman, and Michael O. Poulter. 2012. “Molecular Pathway Reconstruction and Analysis of Disturbed Gene Expression in Depressed Individuals Who Died by Suicide.” *PloS One* 7 (10): e47581. https://doi.org/10.1371/journal.pone.0047581.